Titre: Title:	Dynamics of Excitonic Complexes Bound to Isoelectronic Centers: Toward the Realization of Optically Addressable Qubits
Auteur: Author:	Philippe St-Jean
Date:	2016
Type:	Mémoire ou thèse / Dissertation or Thesis
Référence: Citation:	St-Jean, P. (2016). Dynamics of Excitonic Complexes Bound to Isoelectronic Centers: Toward the Realization of Optically Addressable Qubits [Thèse de doctorat, École Polytechnique de Montréal]. PolyPublie. https://publications.polymtl.ca/2329/

UNIVERSITÉ DE MONTRÉAL

DYNAMICS OF EXCITONIC COMPLEXES BOUND TO ISOELECTRONIC CENTERS: TOWARD THE REALIZATION OF OPTICALLY ADDRESSABLE QUBITS

PHILIPPE ST-JEAN
DÉPARTEMENT DE GÉNIE PHYSIQUE
ÉCOLE POLYTECHNIQUE DE MONTRÉAL

THÈSE PRÉSENTÉE EN VUE DE L'OBTENTION
DU DIPLÔME DE PHILOSOPHIÆ DOCTOR
(GÉNIE PHYSIQUE)
SEPTEMBRE 2016

UNIVERSITÉ DE MONTRÉAL

ÉCOLE POLYTECHNIQUE DE MONTRÉAL

Cette thèse intitulée:

DYNAMICS OF EXCITONIC COMPLEXES BOUND TO ISOELECTRONIC CENTERS: TOWARD THE REALIZATION OF OPTICALLY ADDRESSABLE QUBITS

présentée par: ST-JEAN Philippe
en vue de l'obtention du diplôme de: Philosophiæ Doctor
a été dûment acceptée par le jury d'examen constitué de:

M. MÉNARD David, Ph. D., président
M. FRANCOEUR Sébastien, Ph. D., membre et directeur de recherche
M. MOUTANABBIR Oussama, Ph. D., membre
Mme ECONOMOU Sophia, Ph. D., membre externe

DEDICATION

To Béatrice,
with love.

ACKNOWLEDGEMENT

Over the past seven years, I have had the opportunity to work, at Polytechnique Montréal, with remarkable people that have enormously helped me, both scientifically and humanly. I would like to thank particularly my supervisor Sébastien Francoeur who offered me an inestimable support over all these years. I extremely appreciated the openness with which he considered all the scientific ideas I could come up with, as well as his great generosity for alway taking the time to discuss with me, with rigor and passion, about my data and results, or about any other scientific concept I might have been interested in.

I would also like to deeply thank my friend and colleague (in this order) Gabriel Éthier-Majcher with whom I have worked since my first days at Polytechnique Montréal. Gabriel is a constant source of inspiration for me, and I will fondly remember all of our interminable discussions about *every* possible topic. Having the chance to develop such a profound complicity with a fellow worker is a sheer luck for which I am, and will ever be, extremely grateful.

I would as well like to thank all my colleagues and friends who I have met inside and outside the laboratory during the past years. In particular, Stéphane Marcet and Claudéric Ouellet-Plamondon who guided me when I started my master; Alaric Bergeron, Patrick Lavoie, Anne-Laurence Phaneuf-L'Heureux - who is pursuing the work on ZnSe that I have initiated (Best of luck Anne-Lau!!) -, Jean-Francis Germain and John Ibrahim, with whom I spent long hours of fun in the darkness of the lab; Victor Lambin Iezzi, Sébastien Loranger, Fouzi Benboujja, and my other hockey teammates.

Completing a PhD is not an easy task, and maintaining a positive spirit is not always easy; however, I always had the chance to rely on my family: maman, papa, Justine and Denise - and on my friends - Éric, Charles, Charles, Carl-André, Didier, Marc, Cédric, Lucka and Vincent - who, relentlessly, supported and cheered me up during these years. To all, a thousand thanks from the bottom of my heart!

Last but not least, I would like to thank tenderly my wife Béatrice Boudreault. Although it is impossible in such few words to express all the good her presence brings me every day, I would like to dedicate this thesis to her as an expression of the brightness our encounter, in the middle of my PhD, has brought to my life.

RÉSUMÉ

La réalisation de qubits pouvant être couplés efficacement à des photons optiques est nécessaire pour réaliser la transmission d'information quantique à longue distance, par exemple à l'intérieur d'un réseau quantique. Le principal obstacle empêchant la réalisation de ces qubits addressables optiquement vient de la grande difficulté de trouver une plateforme offrant à la fois une grande homogénéité et un fort couplage optique. Les centres isoélectroniques (CIs), qui sont des impuretés isovalentes à l'intérieur d'un matériau semi-conducteur, représentent une alternative fort intéressante aux systèmes de qubits adressables optiquement proposés dans la littérature, soit les boîtes quantiques auto-assemblées et les centres NV dans le diamant souffrant, respectivement, d'un fort élargissement inhomogène et d'un couplage optique moins grand que les CIs. En effet, la nature atomique des CIs leur assure une homogénéité comparable aux centres NV et leur capacité à lier des complexes excitoniques présentant de forts moments dipolaires permet d'obtenir un couplage avec les champs photoniques aussi fort que dans les boîtes quantiques.

Le but du travail présenté dans cette thèse est d'évaluer le potentiel de différents complexes excitoniques liés à ces CIs pour fabriquer des qubits adressables optiquement. Cette thèse par articles est séparée en deux grandes sections. Dans la première section, correspondant aux articles 1 et 2, j'ai étudié les caractéristiques physiques de qubits excitoniques liés à des CIs d'azote dans le GaP (Article 1) et le GaAs (Article 2). Plus précisément, ces articles présentent une analyse approfondie combinant des mesures de photoluminescence résolue dans le temps et des modèles de balance de populations afin d'identifier et de quantifier les différents mécanismes impliqués dans la dynamique de recombinaison des excitons. Dans la seconde section, j'ai démontré l'initialisation d'un qubit de spin de trou lié à un centre isoélectronique de Te dans une matrice de ZnSe. Contrairement aux qubits excitoniques, la cohérence des qubits de spin n'est pas limitée par leur émission spontanée permettant ainsi d'atteindre des temps de cohérence beaucoup plus intéressants.

Le premier article de cette thèse présente une étude de la dynamique de recombinaison des excitons liés à des CIs d'azote dans le GaP. Le principal avantage relié à l'étude de ce système vient du fait qu'une grande variété de centres sont accessibles : ils peuvent être formés de 1,2 ou 3 impuretés d'azote et présenter différentes symétries à l'intérieur du matériau hôte. Bien qu'il soit difficile de réaliser des qubits adressables optiquement dans ce système dû à son faible taux d'émission spontannée, cette étude a permis de mieux comprendre comment configuration atomique d'un CI influence les différents mécanismes impliqués dans

la dynamique de recombinaison des excitons (capture, transferts inter-niveaux, et émission radiative et non-radiative).

Le second article présente une étude de la dynamique de recombinaison des excitons liés à des CIs d'azote dans le GaAs. Contrairement aux CIs dans le GaP, ceux dans le GaAs présentent des temps de vie très intéressants, comparables à ceux observés dans les boîtes quantiques, et sont donc beaucoup plus intéressants pour la transmission d'information quantique. L'analyse qui a été réalisée avec ce système est beaucoup plus élaborée que celle réalisée dans le GaP, ce qui a permis d'identifier directement les mécanismes impliqués dans la relaxation inter-niveaux des excitons : leur couplage avec des photons LA et l'interaction hyperfine. Bien que le premier effet ne soit pas observé dans les boîtes quantiques dû à la levée de dégénérescence entre les états de trous lourds et de trous légers, le second effet s'est avéré très comparable à l'interaction hyperfine dans les boîtes quantiques.

Finalement, le dernier article démontre, pour la première fois, l'initialisation d'un spin de trou lié à une impureté, ici un CI de Te dans le ZnSe. En plus du fait que le temps de cohérence des qubits de spins ne soit pas limité par l'émission spontanée, l'utilisation d'un spin de trou dans un matériau II-VI représente également des avantages considérables par rapport aux spins électroniques dans des matériaux III-V. D'abord, l'interaction hyperfine entre le moment magnétique des trous et celui des spins nucléaires est inférieure à celle des électrons, menant à des temps de cohérence un ordre de grandeur plus longs. De plus, la majorité des isotopes de Zn, Se et Te ont des spins nucléaires nuls ce qui diminue encore plus l'interaction hyperfine. Le protocole d'initialisation utilisé, basé sur l'effet tunnel d'excitons liés à des donneurs neutres, permet d'atteindre une fidélité de 98.5 % en un très court temps de 150 ps.

ABSTRACT

The realization of qubits that can be efficiently coupled to optical fields is necessary for long distance transmission of quantum information, e.g. inside quantum networks. The principal hurdle preventing the realization of such optically addressable qubits arises from the challenging task of finding a platform that offers as well high optical homogeneity and strong light-matter coupling. In regard to this challenge, isoelectronic centers (ICs), which are isovalent impurities in a semiconductor host, represent a very promising alternative to the well-studied epitaxial quantum dots and NV centers in diamond which suffer, respectively, from a large inhomogeneous broadening and a less effective coupling to optical fields than ICs. Indeed, the atomic nature of ICs insures an optical homogeneity comparable to NV centers, and their ability to bind excitonic complexes with strong electric dipole moments allows them to offer an optical coupling similar to quantum dots.

The aim of the work presented in this thesis is to evaluate the potential of different excitonic complexes bound to these ICs for building optically addressable qubits. This thesis by articles, is separated in two parts. In the first part, corresponding to Article 1 and 2, I study the physics of exciton qubits bound to N ICs in GaP (Article 1) and in GaAas (Article 2). More precisely, these articles present an analysis combining time-resolve PL measurements and balance of population models, allowing to identify and quantify the different mechanisms involved in the exciton recombination dynamics. In the second part, I demonstrate the initialization of a hole-spin qubit bound to a Te IC in ZnSe. Contrary to exciton qubits the coherence time of spin qubit is not limited by their spontaneous emission, allowing to preserve coherence on a much more significant timescale.

The first article of this thesis presents a study of the recombination dynamics of excitons bound to N ICs in GaP. The principal advantage of studying this system comes from the large variety of atomic configurations that can be accessed: ICs can be formed from one, two or three impurities, and exhibit different local symmetries inside the host lattice. Although it appears very challenging to realize optically addressable qubits in this system due to its low coupling to optical fields, it has allowed for a better understanding of how the atomic configuration of the underlying IC influences the different mechanisms involved in exciton recombination dynamics (capture, inter-level transfers, and radiative and non-radiative recombination).

The second article presents a study of the recombination dynamics of excitons bound to N ICs in GaAs. Contrary to ICs in GaP, ICs in GaAs exhibit a much stronger optical coupling,

comparable to those observed in quantum dots, and are thus much more interesting in the context of quantum information transmission. The analysis realized in this system is more elaborated, allowing us to identify directly the important mechanisms involved in exciton inter-level relaxation: LA phonon mediated transfers, and hyperfine interaction. Although the former effect is not observed in quantum dots due to the important splitting between light- and heavy-holes, the latter is demonstrated to be comparable in strength to hyperfine interaction in quantum dots.

Finally, the last article demonstrates, for the first time, the initialization of a hole-spin bound to a single impurity: a Te IC in ZnSe. In addition to the fact that the coherence time of spin qubits is not limited by spontaneous emission, the use of a hole-spin in ZnSe brings further advantages relatively to electron spins in III-V nanostructures. Firstly, hyperfine interaction between the magnetic moments of a hole-spin and of a nuclear spin is less than that for electrons, leading to enhanced coherence times (by at least an order of magnitude). Secondly, most Zn, Se and Te isotopes present vanishing nuclear spins which further mitigates the hyperfine interaction. The initialization scheme used, based on the efficient tunneling of excitons bound to neutral donors, has allowed to reach 98.5% fidelities and initialization times of 150 ps.

TABLE OF CONTENTS

DEDICATION iii

ACKNOWLEDGEMENT iv

RÉSUMÉ v

ABSTRACT vii

TABLE OF CONTENTS ix

LIST OF TABLES xiii

LIST OF FIGURES xv

LIST OF SYMBOLS AND ABBREVIATIONS xxi

LIST OF APPENDICES xxiii

CHAPTER 1 INTRODUCTION 1
1.1 Technological importance of quantum optical interfaces 3
1.1.1 Quantum networks 3
1.1.2 Quantum repeaters 4
1.2 Design of optical interfaces 5
1.2.1 On the nature of qubits: encoding and decoherence 5
1.2.2 Photonic qubits 7
1.2.3 Optically addressable qubits 8
1.3 Potential candidates for optically addressable qubits 10
1.3.1 Trapped ions 11
1.3.2 Quantum dots 11
1.3.3 Nitrogen-vacancy centers in diamond 13
1.3.4 Isoelectronic centers 15
1.4 Outline of the thesis 16

CHAPTER 2 LITERATURE REVIEW - ISOELECTRONIC CENTERS IN SEMICONDUCTORS 17
2.1 On the nature of isoelectronic centers 17

2.2 Description of the various types of ICs 20
2.2.1 Nitrogen ICs in gallium phosphide 20
2.2.2 Nitrogen dyads in gallium arsenide 26
2.2.3 Te dyads in zinc selenide 31
2.3 Fine structure of excitons bound to ICs 34
2.3.1 Exciton wave-functions 35
2.3.2 Invariant expansion of exciton Hamiltonian 36
2.3.3 Optical selection rules 41
2.4 Fine structure of positive trions bound to ICs 45
2.4.1 Trions wave-functions 45
2.4.2 Determination of the charge of the trion 48

CHAPTER 3 SCIENTIFIC APPROACH AND MOTIVATIONS 50
3.1 Article 1 and 2: Dynamics of excitons bound to ICs 50
3.1.1 Motivations underlying the choice of ICs systems 51
3.1.2 N dyads in GaAs - Article 2 51
3.1.3 Methods 52
3.2 Article 3: Initialization of a hole-spin qubit bound to a Te dyad in ZnSe . . . 54
3.2.1 Enhanced coherence times of hole spins in ZnSe 54
3.2.2 Experimental setup 57

CHAPTER 4 ARTICLE 1 - RECOMBINATION DYNAMICS OF EXCITONS BOUND TO NITROGEN ISOELECTRONIC CENTERS IN δ-DOPED GAP 59
4.1 abstract 59
4.2 Introduction 59
4.3 Samples and experimental setup 61
4.4 IC configurations and excitonic fine structures 61
4.5 Excitonic recombination regimes 65
4.6 Time dynamics model 67
4.7 Discussion on the processes governing the dynamics 73
4.8 Conclusion 74

CHAPTER 5 ARTICLE 2 - DYNAMICS OF EXCITONS BOUND TO NITROGEN ISOELECTRONIC CENTERS IN GAAS 76
5.1 Abstract 76
5.2 Introduction 76
5.3 Samples and methods 78

5.4 Experimental results 78
5.4.1 Fine structure of the emission 78
5.4.2 Luminescence decay time anisotropies 79
5.4.3 Revealing symmetries in photoluminescence intensities 82
5.4.4 Quenching of the photoluminescence total intensity 82
5.5 Exciton dynamics model 82
5.5.1 Part I - Excitonic wavefunctions 85
5.5.2 Part II - Exciton transfer mechanisms 85
5.5.3 Part III - Population balance model 91
5.6 Results and analysis 91
5.6.1 Excitonic fine structure 92
5.6.2 Exciton dynamics 93
5.7 Conclusion 101

CHAPTER 6 ARTICLE 3 - HIGH-FIDELITY AND ULTRAFAST INITIALIZATION OF A HOLE-SPIN BOUND TO A TE ISOELECTRONIC CENTER IN ZNSE . 102
6.1 Abstract 102
6.2 Introduction 102
6.3 Sample and experimental method 103
6.4 Initialization of a hole spin 106
6.4.1 Decay time of trions luminescence 109
6.5 Conclusion 110

CHAPTER 7 GENERAL DISCUSSION 111
7.1 Dynamics of excitons bound to N ICs in GaP - Article 1 111
7.1.1 Reexamination of exciton capture and non-radiative recombination . 111
7.1.2 Evaluation of exciton radiative decay and inter-level transfers 114
7.2 Dynamics of excitons bound to N ICs in GaAs - Article 2 114
7.2.1 Exciton fine structure 114
7.2.2 Radiative recombination vs. inter-level transfers 115
7.3 Article 3- Hole-spin initialization schemes 116
7.3.1 Optical pumping of a hole-spin 117
7.3.2 Coherent population trapping 119
7.3.3 Ionization of excitons 120
7.3.4 Summary of the different initialization schemes 121

CHAPTER 8 CONCLUSION AND RECOMMENDATIONS 122

8.1 Requirements for building optically addressable qubits 122
8.1.1 Exciton qubits bound to N ICs in GaP 123
8.1.2 Exciton qubits bound to N dyads in GaAs 124
8.1.3 Spin qubits bound to Te dyads in ZnSe 124
8.1.4 Summary of the different qubits performances 125
8.2 Outlook 125

REFERENCES 128

APPENDICES 154

LIST OF TABLES

Table 2.1 Current consensus on the different dyad configuration in GaP, as presented in Ref. [97, 98]. The first column identifies the different multiplets using Thomas and Hopfield notation [96], the second column identifies the number of atoms forming the center, and the second and third columns respectively present the local symmetry and orientation inside the host lattice of every IC. Symmetries and orientations that have not been unambiguously identified are presented between parentheses. 26

Table 2.2 Current consensus on the different dyad configuration in GaAs that form localized states at atmospheric pressure [43, 91, 104]. The second and third columns respectively present the local symmetry and orientation of every dyad inside the host lattice. 31

Table 2.3 Symmetry-adapted exciton bases ψ_{1-8} for T_d and C_{2v} point group. In C_{2v}, ψ_{1-4} correspond to heavy-hole excitons, and ψ_{5-8} to light-hole excitons. 40

Table 2.4 oscillator strength of the different exciton states forming the C_{2v} symmetry-adapted basis 44

Table 3.1 Natural abundance of the principal isotopes of Zn 57

Table 3.2 Natural abundance of the principal isotopes of Se 57

Table 3.3 Natural abundance of the principal isotopes of Te 57

Table 4.1 Experimental values describing the exciton dynamics. The capture rate ranged between 400 and 600 ps and did not vary with temperature or IC configuration. For the single-atom configuration, the *weak* states (B-line) was not observed. 72

Table 5.1 Symmetry-adapted exciton wavefunctions, C_{2v} representations and dipole moments (expressed in units of ($\langle s|x|x\rangle$, $\langle s|y|y\rangle$, $\langle s|z|z\rangle$)). ψ_{1-4} and ψ_{5-8} are built from heavy- and light-hole states, respectively. 87

Table 5.2 Calculated wavefunctions, energies and relative dipole moments of excitons bound to a dyad of C_{2v} symmetry. The PL energies are relative to the state with the lowest emission energy, $|Z_1\rangle$. States ψ_{1-8} are presented in Table 5.1. 94

Table 5.3 Parameters describing the exciton dynamics. 94

Table 5.4 Exciton transfer rates (in ns^{-1}). All temperature dependent rates are given at 5 (upper entry) and 12 K (lower entry). Transfers resulting from the coupling of light- and heavy-holes through LA phonons are shown in italic. All other inter-level rates results from the hyperfine interaction. 97

Table 7.1 Non-radiative recombination mechanisms associated to single N and NN_i ICs (hole or exciton escape) determined in this work as well as in previous works presented in Ref. [84, 148]. The activation energies extracted for these mechanisms (E_a) are presented as well as the emission energy (E_i). 113

Table 7.2 Summary of the different hole-spin initialization scheme used in Qds as well as that used in the last article. All values are extracted for epitaxial QDs, except coherent population trapping determined from NV centers in diamond. The references from which were taken the values are presented in the first column. 121

Table 8.1 Summary of the different systems considered for hosting optically addressable qubits in this thesis and in most studied platforms in the literature (self-assembled quantum dots and NV centers). * indicates values taken at room temperature, N/A indicates a value that is still lacking. 126

Table A.1 The T_d double group character table presents 7 irreducible representations, among which two corresponds to the symmetry representation of s-type conduction electrons (Γ_6) and light- and heavy-holes (Γ_8). Space and angular momentum vectors transform according to the Γ_4 and Γ_5 representations, respectively. 155

Table B.1 The C_{2v} double group character table presents 5 classes of symmetry representations, where the spatial coordinates x, y, and z are all non-equivalent, as they transform according to different representation. Half-integer spin states all belong to the Γ_5 representation. 157

LIST OF FIGURES

Figure 1.1 The Bloch sphere representation for a two-level system, representing a spin 1/2 quantum state. 6

Figure 1.2 Energy levels corresponding to the two important architectures of optically addressable qubits. 9

Figure 1.3 (a) Cross-section of a self-assembled InGaAs quantum dot inside a GaAs matrix. Here the growth is realized along the z-axis. (b) The smaller band gap of InGaAs than GaAs, thereby trapping charges inside the QD. 12

Figure 1.4 (a) NV centers consist of a nitrogen substitutional N impurities next to a vacancy inside a diamond lattice. (b) The energy levels associated to a negatively charged NV center present three $S = 1$ ground states and excited states. 14

Figure 2.1 Schematic representation of the wave-function of a strongly-localized electron and a Coulomb bound hole. In this case, the IC presented corresponds to an electron trap, indicating that the IC is more electronegative than the host. For a hole acceptor, the wave-functions would be similar, but interchanged. 19

Figure 2.2 Photoluminescence spectrum of nitrogen-doped GaP for different doping concentration. Transition associated to N ICs (A, B and NN_i lines) are labeled, as well as their LO, TO, and local-mode (loc) phonon replica. [96] 21

Figure 2.3 NN_1 dyads in GaP corresponding to N impurities located on nearest-neighbor sites of the anionic sub-lattice. Two different orientations are presented. 22

Figure 2.4 Only three transitions (labeled $NN_{1,3,4}$) are observed in PL spectra of N doped GaAs. Figure from Ref. [43]. 28

Figure 2.5 Comparison between the spectral position of the different N ICs observed in GaP and GaAs. Most exciton bound to N ICs in GaAs form resonant states in the conduction band. The only three configurations emitting below the band gap are dyads in the first NN_1, third NN_3, and fourth NN_4 nearest-neighbor configurations. 29

Figure 2.6 Confocal microscopy allows to optically isolate single nitrogen dyads in GaAs. Panel (a) presents micro-PL spectra of two different single emitters: $NN_{1,4}$. Both spectra are extracted from the point of highest in the underneath spatial PL maps (panel (b)) where single dyads are isolated. [104] 30

Figure 2.7 (a) Macro-photoluminescence measurements of Te doped ZnSe presents three broad lines of emission labeled I (around 2610 meV), II (between 2770 and 2775 meV), and III (between 2775 and 2800 meV). A strong peak associated to the emission from excitons bound to neutral donors is observed around 2880 meV. Figure from Ref. [108] (b) Micro-photoluminescence reveal several sharp lines associated to Te dyads in region II. Figure from the last article of this thesis. 32

Figure 2.8 (a) Linear (b) temporal mapping of the PL intensity from a Te dyads exhibiting transitions associated to excitons (X_0), trion (X^+ and bi-exciton (XX). (c) The evolution of the exciton, trion and bi-exciton intensities with the excitation powers follows a power law $I \propto P^{k_i}$, where $k_{\mathrm{X}} = 0.6$, $k_{\mathrm{X^+}} = 0.7$, and $k_{\mathrm{XX}} = 1.2$. Figures from Ref. [108]. . 33

Figure 2.9 Schematic diagrams of excitons energy levels under different symmetries: O(3) is the symmetry of vacuum, T_d corresponds to a substitutional impurity inside a zinc-blende lattice, and C_{2v} is the local symmetry of NN_1 in GaAs and GaP. Red (black) levels correspond to optically active (dark) excitons. 42

Figure 2.10 The photoluminescence of isolated N (a) and Bi (b) ICs in GaP presents one strong optical transition labeled the A-line (red), associated to the dipole-allowed radiative decay of a Γ_4 exciton, and two weak transitions labeled B-lines (black) associated to the dipole-forbidden radiative decay of Γ_3 and Γ_5 excitons (only obsever at very low temperature, $T \sim 1.6\ K$) [124]. For N impurities, the two B-lines are not spectrally resolved. [96] 43

Figure 2.11 Axes of a dyad in nearest-neighbor configuration presenting a C_{2v} symmetry. 44

Figure 2.12 NN_1 dyads in GaAs present a C_{2v} symmetry exhibit up to 6 linearly polarized transitions, oriented along $0° - 90°$ for *in-plane* dyads (a), and along $45° - 135°$ for *out-of-plane* dyads (b). However, in-plane dyads only present 4 transitions corresponding to $X_{1,2}$ and $Y_{1,2}$, because the experimental configuration does not allow to monitor the emission from $Z_{1,2}$, and out-of-plane dyads only present 5 optical transitions due to the vanishing electric dipole moment of Z_1. [90, 125] 46

Figure 2.13 Conservation of angular momentum implies that only transitions between spin-up (-down) trions and spin-up (-down) hole states. These optical transitions are respectively polarized circularly left (σ^-) and right (σ^+). Transitions between spin-up (-down) trions and spin-down (-up) hole states are forbidden in the absence of hole state mixing. . . 48

Figure 3.1 Time-resolved PL setup used in article 1 and 2. The inset presents a close-up on the sample. 53

Figure 3.2 Spin noise is the result of the fluctuating nuclear magnetic moments under the wave-function of the electron (or hole). 56

Figure 3.3 Amplitudes of s- and p-type wave-functions associated to hole and electrons, respectively. Contrary to electron, hole wave-functions typically vanish at the position of the nucleus, mitigating hyperfine interaction. 58

Figure 4.1 Photoluminescence spectrum measured at 30 K. The sharp lines correspond to the emission from ICs : single-atom configuration (A-Line) and dyads (NN_i). Phonon replica of the A-Line and NN_4 are also observed. 62

Figure 4.2 PL intensity as a function of energy and polarization for dyad NN_1 at (a,b) T = 4 K and (c,d) T = 30 K. The attribution of all excitonic transitions is presented in figures (a) and (c) where the black and red curves spectra show the PL polarized at 0° and 90°, respectively. (e) PL intensity as a function of temperature for bright ($B_{x,y}$) and weak ($W_{x,y}$) transitions. Dark transitions ($D_{1,2}$) are not observed. 64

Figure 4.3 (a) Temporal dependence of the PL intensity of NN_6 at T = 10, 28 and 60 K. The red curves represent a single exponential intensity rise followed by and a single- or bi- exponential decay and the yellow curves represent calculated PL decay curves, obtained by the balance of populations model presented in section V, that best fitted the data. (b) The black curve shows the emission rate, $\Gamma_l = \tau_l^{-1}$, of NN_6 as a function of temperature and the blue curve shows the inverse of the rise time of the PL from excitons bound to isolated nitrogen atoms (A-line). The vertical lines separate the three PL decay regimes discussed in the text. 66

Figure 4.4 Three-level model used for the analysis of the exciton dynamics. All transfer processes considered (γ) are described in the text and E refers to energy difference between the three excited levels. 68

Figure 4.5 Temperature dependence of the emission rate, $\Gamma_l = \tau_l^{-1}$, extraced on the experimental (symbols) and calculated (lines) PL decay curves for all ICs configurations. 71

Figure 5.1 (a) In-plane and out-of-plane configurations for dyads of C_{2v} symmetry. (b) Calculated spectral position of all excitonic states of a nitrogen dyad oriented along $\langle 110 \rangle$. (c) Photoluminescence intensity polarized parallel to an out-of-plane nitrogen dyad of C_{2v} symmetry. (d) Photoluminescence intensity polarized perpendicular (0°, red curve) and parallel (90°, black curve) to the in-plane nitrogen dyad studied in this work. (e) Photoluminescence intensity map as a function of energy and linear polarization of the emission. 80

Figure 5.2 Time-resolved PL from the single nitrogen dyad presented in Fig. 5.1. Panel (a) shows all four excitonic transitions at $T = 8\ K$ and (b) shows transition Y_1 at all temperatures studied. For both panels, the red curves show the sum of one rising and decaying mono-exponentials that best fitted the data; decay times are indicated. Blue curves show the PL intensities calculated from the model presented in Section 5.5. (c) Temperature evolution of extracted decay times. Y_1 and Y_2 (X_1 and X_2) are represented by the red and blue squares (circles). Dashed (X_i) and solid (Y_i) lines are added to guide the eye. 81

Figure 5.3 (a) Temperature dependence of the relative PL intensity of the four allowed excitonic transitions. Y_1 and Y_2 (X_1 and X_2) are represented by the red and blue squares (circles). Dashed (X_i) and solid (Y_i) lines are added to guide the eye. (b) Arrhenius plot of the total PL intensity measured from all four transitions shown in Fig. 5.1. The solid curve shows the calculated intensity of a thermally activated process. 83

Figure 5.4 Schematic representation of the model used to calculate excitonic energies and wavefunctions, time-resolved luminescence curves, and luminescence intensities. Quantities in gray boxes are adjustable parameters and quantities labeled in red are those directly compared to the experimental data. Boxes with thicker contour indicate temperature dependent transfer mechanisms. Inset: Population balance model for excitonic state i involving the ground state 0 and the seven other excitonic states for which $i \neq j$. 84

Figure 5.5 Schematic diagrams of energy levels for a free exciton in a GaAs crystal and for an exciton bound to a nitrogen dyad of C_{2v} symmetry. The ordering of the levels is obtained from Eq. 5.1 and the PL data. . . . 86

Figure 5.6 Panel (a) compares the temperature dependence of experimental and calculated TRPL decay times. Panels (b) and (c) shows the relative photoluminescence intensities of $X_{1,2}$ and $Y_{1,2}$, respectively (error bars are too small to be visible). Panel (d) shows the total photoluminescence intensity. Data points and curves represent experimental and calculated values, respectively. 95

Figure 6.1 (a) Time-integrated micro-photoluminescence spectrum of the sample studied in this work. This spectrum reveals the presence of a three distinct Te dyads preferentially binding neutral excitons (X_0), bi-exciton (XX_0), and positive trions (X^+). (b) and (c) Schematic diagrams of the selection rules associated to trion emission at $B = 0$ and 5 T in a Faraday configuration. σ and π represent circularly and linearly polarized transitions. (d) and (e) Trion photoluminescence intensity as a function of the excitation energy and circular polarization at these magnetic field values. 105

Figure 6.2 Time-resolved photoluminescence of trions bound to dyad 1 presented in panel (a) of Fig. 6.2 for excitations tuned to the D-X^0 band (a), to the HH band edge (b), and far above the LH band edge but below the spin-orbit band edge (c)-(d). The blue (red) curves show the emission intensity under co-polarized (cross-polarized) circular excitation and detection. (e) The horizontal line indicates the degree of polarization of the emission for an excitation energy 250 meV above the ZnSe band gap. (f) Decay times of trion emission for co- (blue squares) and cross-polarized (red circles) configurations as a function of the excitation energy for dyad 1. The dashed line indicates the upper bound for the radiative decay time of trion states (< 50 ps) 108

Figure 7.1 (a) The optical pumping schemes require a Λ system where the spin states are split and are connected to an excited state, here a trion state. (b) In Faraday configuration, the Λ system is provided by the HH-LH mixing that opens the cross transitions (dashed lines) radiative channels. (c) In Voigt configuration, the Λ system is provided by the in-plane magnetic field that mixes the spin-up and -down state. . . . 118

Figure 7.2 Ionization of an exciton leads to the initialization a hole in a well-defined spin state. This scheme is however limited by the exchange interaction between the electron and hole forming the exciton, as the driving field leads to an exciton in a superposition state rather than a well-defined state. ([198]) 120

Figure A.1 An isolated-atom IC (pink atom) presents a T_d symmetry inside a zinc-blende host. The symmetry point group describing the defect and its host includes 24 operations. 154

Figure B.1 Dyad (green atoms) presenting a C_{2v} symmetry inside a zinc-blende host. The symmetry point group describing the defect and its host includes 8 operations. 156

LIST OF SYMBOLS AND ABBREVIATIONS

Symbols related to qubits

θ	Longitudinal coordinate describing the strength of the superposition
ϕ	Transverse coordinate describing the phase of the superposition
ω	Frequency of precession
ΔE	Energy splitting
T_1	Decoherence time associated to relaxation
T_2^*	Decoherence time associated to dephasing

Abbreviations for the different qubit pysical supports

ICs	Isoelectronic centers
QDs	Quantum dots
NV	Nitrogen-vacancy centers in diamond
NV^0	Neutral NV center
NV^0	Negatively charged NV center
a_b	Bohr radius
a	Lattice constant
HTL	Hopfield, Thomas and Lynch sequential mechanism for binding charges
X	Neutral exciton
$X^{\pm}$	Positively and negatively charged excitons (trions)
XX	Bi-exciton

Symbols used to describe wave-functions

$\|0\rangle$	Vacuum state
$\|\Psi\rangle$	Exciton wave-function
$\|\Phi\rangle$	Envelope function of the exciton wave-function
$\|\psi_{e,h}\rangle$	Atomic part of the electron and hole wave-function
$\|\phi_{e,h}\rangle$	Angular part of the electron and hole atomic wave-function
$\|\chi_{e,h}\rangle$	Spin part of the electron and hole atomic wave-function
(α, β)	Spin-up and -down electron state
(ϕ_{1-4})	Hole wave-function in the coupled basis $\|J, m_J\rangle$
H_e	Electron Hamiltonian
H_h	Hole Hamiltonian

H_{ex}	Exchange interaction Hamiltonian
H_X	Exciton Hamiltonian
$g_{x,y,z}^{(e,h)}$	Electron and hole g-factors
$\delta_{x,y,z}^{(e,h)}$	Electron and hole diamagnetic shifts
$v_{x,y,x}$	Crystal-field parameters
$a_{x,y,z}$	Exchange parameters

Abbreviations used to describe the experimental setup

PL	Photoluminescence
TRPL	Time-resolved potoluminescence
CCD	Camera using a charge coupling device
APD	Avalanche photo-diode
CW	Continuous excitation or detection
HWP	Half-wave plate
QWP	Quarter-wave plate
POL	Polarizer

LIST OF APPENDICES

Appendice A T_d - symmetry operations and character table 154

Appendice B C_{2v} - symmetry operations and character table 156

CHAPTER 1 INTRODUCTION

The theory of quantum mechanics developed in the mid-1920s has led to some of the most significant technological breakthroughs of the last century, including superconductivity, nuclear magnetic resonance, transistors and lasers. The most defining principles of this theory, and the most peculiar, are the principles of superposition - a physical object can be found simultaneously in two distinct states -, and of entanglement - distant objects can be instantaneously connected. Although these principles have been some of the most accurately tested phenomena of modern physics, understanding how they can be harnessed to develop novel technologies remains highly challenging, yet extremely promising. Among the different fields of technology that have gained particularly insightful inputs from quantum mechanics, the processing and transmission of information is, right now, one of the most important and fast-growing [1].

The advantage of applying the principles of quantum mechanics to the realm of information theory arises from the fact that quantum information can be encoded in basic units (called qubits, for quantum bits) that are not restricted to be one or the other of the boolean variables 0 and 1, but can be formed from any arbitrary superposition of these:

$$|\Psi\rangle = a\,|0\rangle + b\,|1\rangle\,. \tag{1.1}$$

Here, the normalization of quantum wave-functions requires that $|a|^2+|b|^2 = 1$. Furthermore, contrary to classical information where every bit is addressed and controlled independently, qubits form entangled states, leading to a computational power that grows exponentially with the number of qubits: n qubits can be in a superposition of up to 2^n quantum states, whereas n classical bits can be found in only one of these 2^n states at a particular time. The most important proposal for harnessing this enhanced information complexity were developed independently in the 1980s, and correspond to the processing of quantum information and to the realization of quantum cryptography protocols.

Quantum information processing was first proposed by Richard Feynman [2] and David Deutsch [3] who assessed the possibility to process many operations simultaneously through the evolution of superposed quantum states in order to solve certain problems that are computationally too complex to be solved on a realistic timescale by classical computers. For example, Feynman argued that the intrinsic parallelism of such *quantum computers* could be exploited to simulate much more efficiently the quantum interactions inside a physical system,

e.g. molecules or crystals.

The field of quantum cryptography was developed around the same years by Gilles Brassard and Charles Bennett [4] who elaborated a protocol of cryptographic key distribution where the elements of the keys are encrypted in superposed quantum states (e.g. photonic polarization states). In contrast with classical protocols of key distribution that requires enormous yet finite calculations resources to break encryption codes, *quantum key distribution* protocols allow two parties to share public keys that can not be intercepted by an eavesdropper without revealing his presence. Equivalent quantum key distribution protocols, based on the sharing of entangled quantum states, were developed by Artur Ekert in 1991 [5], and by Brassard, Bennett and Mermin [6].

Quantum information processing and quantum cryptography both remained marginal research areas until the mid-1990s when Peter Shor demonstrated that a quantum algorithm (i.e. an algorithm that is run on a quantum computing machine) could factorize integers in a polynomial timescale [7], rather than on an exponential timescale as for classical algorithms. On the one hand, integer factorization lies at the core of classical cryptographic key distribution (e.g. in the RSA protocol), and Shor's algorithm therefore demonstrates the need for quantum cryptography, as the perspective of a practical quantum computer represents a serious threat to classically encrypted communications. On the other hand, Shor's algorithm demonstrates that quantum computers can be used, not only for simulating physical systems, but as well for solving mathematical problems. This demonstration triggered the elaboration of quantum algorithms that could lead to a significant speedup for the resolution of important mathematical problems. For example, Lov Grover established in 1996 a quantum algorithm allowing for a quadratic speedup in searches through unsorted databases [8], a task of crucial importance in many industrial areas.

Following the work of Shor, seminal demonstrations were realized both in the fields of quantum cryptography and quantum computation over the last decades: protocols of quantum key distribution have been experimentally demonstrated [9, 10], and are now commercially available [11, 12]; quantum algorithms [13–15] and simulations [16, 17] were realized on small scale prototypes of quantum computers; and storage of quantum information have been reported over considerable timescales, up to 6 hours at cryogenic temperatures [18] and up to 39 minutes at room temperature [19].

These demonstrations were however realized by using different physical supports of qubits that are very challenging to connect together inside global quantum information systems: processing and storage of quantum information are mostly realized with matter-based qubits (e.g. electronic or nuclear spins, charges, and superconducting circuits), whereas transmission

and cryptography are realized with optical photons. This situation is reminiscent of classical information which is processed and stored in solid-state supports (e.g. with capacitors, transistors, or micro-magnets) but transported over long distances by electromagnetic waves (using optical or RF frequencies), which has thus required the development of transmitters and receivers for transferring information from matter to photon, and vice-versa. The scope of this thesis is to assess the difficulty to connect solid-state and photon platforms in quantum information systems, by developing a novel qubit implementation that could serve as a light-matter interface.

1.1 Technological importance of quantum optical interfaces

The importance of realizing these optical interfaces is twofold: (1) connecting remote quantum computers or memories inside quantum networks; and (2) building quantum analogues of classical relays (quantum repeaters) necessary to prevent the loss of quantum information in long distance transmission. Both aspects are hereafter explicitly addressed in order to demonstrate their technological importance.

1.1.1 Quantum networks

The ability to connect classical computers inside a network (e.g. internet) critically improves computational and storage capabilities. This perspective is similar in the case of quantum information, as quantum networks would ultimately be necessary to overcome the scalability limitations of single quantum computers. [20–23]

Contrary to classical networks where the nodes can be controlled independently as they are simply connected by classical channels, a quantum network is built by *entangling* physically separated quantum systems. This entanglement represents a crucial difference as it leads to an exponential growth of the computational power: entangling k nodes each containing n qubits leads to the ability to process simultaneously superpositions of up to 2^{kn} quantum states [20]. In comparison, connecting quantum systems with classical channels would lead to an increase of the computational power simply proportional to $k2^n$. Furthermore, the realization of long distance entanglement in quantum networks could allow to implement quantum key distribution protocols based on the sharing of entangled quantum states [24], such as those developed by Ekert [5], and by Bennett, Brassard and Mermin [6].

Entangling spatially separated nodes of a quantum network requires to engineer transmission channels along which a mediating particle can transport the shared entangled state from one node to the other. Optical photons are the most interesting candidates to realize this task, as

they can robustly transport a quantum state either through free space or optical fibers and can interact efficiently with the quantum states located at both end of the channel if those states exhibit non-vanishing coupling to optical fields [22, 23]. Building these optically addressable quantum states (referred to in the literature as optically addressable qubits), which are the quantum equivalent of transmitters and receivers in classical networks, therefore lies at the core of the realization of real quantum networks. The work presented in this thesis evaluates the potential of a novel qubit implementation for realizing such optically addressable qubits.

1.1.2 Quantum repeaters

As mentioned above, entangling spatially separated qubits is a very crucial requirement for the realization of quantum networks, and the most robust way to entangle distant quantum systems is through the sharing of optical fields that propagate either through free space or optical fibers.

Recently, the entanglement of solid-state qubits separated by 1.3 km has been achieved using photons transported by optical fibers [25], but efficiently entangling qubits separated by more than 100 km would require the implementation of quantum relays (e.g. every 10 km or so) in order to preserve the entanglement. Two of the most important sources of entanglement loss are photon absorption, e.g. in silica or in the atmosphere, and decoherence of photon states due to their weak yet non-negligible interaction with the environment, e.g. through non-linear effects or birefringence in optical fibers. Since the importance of both of these detrimental effects increases with the distance over which the entanglement is realized, it is necessary to divide the transmission channels in smaller portions where the entanglement can be more easily preserved. This is done by connecting these smaller channels with quantum relays (referred to in the literature as quantum repeaters) that allow to more easily preserve the entanglement over the whole network: closer relays lead to higher probabilities of preserving the entanglement, and, in turn, to higher operation frequencies [26, 27].

These quantum repeaters can be viewed as intermediate nodes in a transmission channel acting as quantum memories with optical interfaces for ingoing and outgoing photons. The role of these quantum memories is to store quantum information over a period of time long enough to reconstruct the entanglement using specific protocols (e.g. entanglement swapping [28], entanglement purification [29], quantum error correction [30]). These quantum memories as well call for the implementation of optically addressable qubits as they require to couple optical fields with a solid-state platform.

1.2 Design of optical interfaces

Optically addressable qubits, which are necessary to the realization of quantum networks and quantum repeaters, consist of quantum memories that can interact with optical fields. In the following, I present the important aspects required in the design of these qubits: firstly, I introduce the physics of qubits, how they can be encoded and how they can interact with their environment; then I present the two important qubit implementations that will be presented in this thesis, photon qubits and optically addressable qubits. I indentify the important requirements for both of these implementations necessary for building efficient optical interfaces.

1.2.1 On the nature of qubits: encoding and decoherence

A qubit is formed from the coherent superposition of two boolean variables (as presented in Eq. 1.1), and can thus be physically encoded in a two-level quantum states. The most common example of such a two-level system in textbooks is the spin state of a spin 1/2 particles, such as electrons. It is possible to write such a state $|\Psi\rangle$ in terms of angles θ and ϕ accounting respectively for the mixing and phase between the spin-up and -down states:

$$|\Psi\rangle = \cos(\theta/2)\,|\uparrow\rangle + \sin(\theta/2)e^{i\phi}\,|\downarrow\rangle\,. \tag{1.2}$$

This state can be easily visualized using the well-known Bloch sphere presented in Fig. 1.1. The north and south pole account for the spin-up and spin-down states, and θ and ϕ describe the azimuthal and longitudinal coordinates. The coordinate ϕ refers to the phase of the qubit which, according to Schrödinger equation, precesses around the z-axis at a frequency proportional to the qubit energy splitting ($\omega = \Delta E/\hbar$) for a state not oriented along the z-axis. One of the most intuitive example is the Larmor precession of a spin in a magnetic field.

Following the laws of quantum mechanics, any measurement of the state of a qubit can be done along a single axis of the Bloch sphere. The result of this measurement leads to two possible outcomes: the state is parallel or anti-parallel to the axis of measurement; and the act of measuring the state of a qubit makes it collapse in the state corresponding to the result of the measurement. For example, measuring the state depicted in Eq. 1.2 along the z-axis can lead to the result $|\uparrow\rangle$ or $|\downarrow\rangle$ with probability $\cos^2(\theta/2)$ or $\sin^2(\theta/2)$, respectively; following this measurement, the qubit will have collapsed along the z-axis in the direction corresponding to the outcome of the measurement.

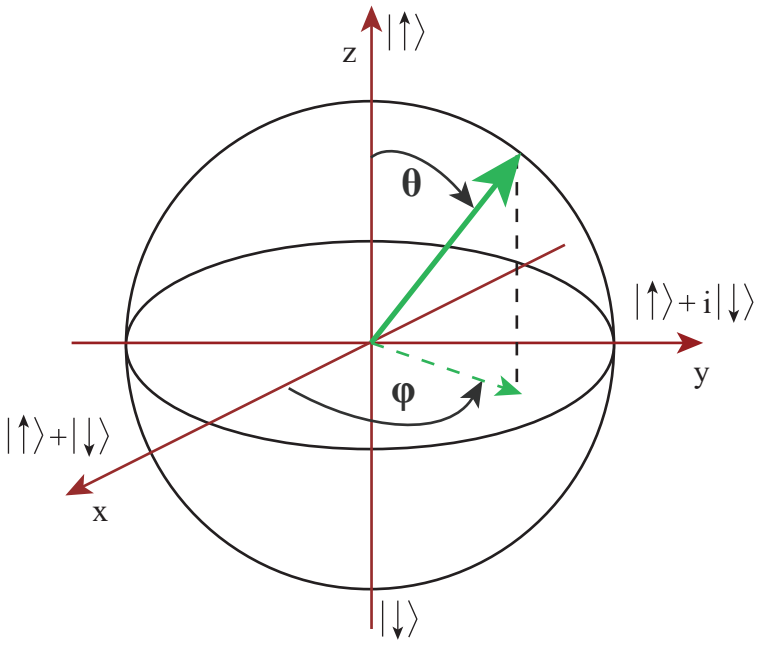

Figure 1.1 The Bloch sphere representation for a two-level system, representing a spin 1/2 quantum state.

Decoherence

However, a two-level system is an idealistic view of a qubit, as interactions with other quantum states in its environment are unavoidable, and lead to irreversible leak of information toward the environment. This leak of information can be viewed as the decoherence of the qubit state (unpredictable evolution of θ and ϕ in Eq. 1.2), and is one of the key aspect preventing the realization of practical quantum computer, as the rate of decoherence is often too important for the realization of error-correction protocols necessary to robustly run real algorithms [30, 31]. There are two important contribution to qubit decoherence: relaxation and dephasing, affecting respectively θ and ϕ in Eq. 1.2 [32].

1- Relaxation

Relaxation can be viewed as a longitudinal collapse of the qubit along an axis of the Bloch sphere, resulting from a perturbation on the environment acting as an unwanted measurement. This is the case for example when a spin qubit such as that describe in Eq. 1.2 interacts with a magnetic field in its environment (e.g. that associated to a magnetic impurity) causing it state to collapse along the direction of the field. The characteristic time of this process is referred to as the relaxation time T_1, and is the analogue of the longitudinal relaxation time in nuclear magnetic resonance experiments. Relaxiation mechanisms are investigated

in details in Article 1 and 2 of this thesis.

2- Dephasing

Perturbations of the environment can also affect the qubit precession (e.g. through a variation of the energy splitting), leading to an unpredictable evolution of the qubit phase from one experiment to the other. These statistical variations of the qubit precession lead to a loss of quantum information as the phase of the qubit does not follow a predictable evolution. The dephasing characteristic time is typically referred to as T_2^*, and is similar to the transverse relaxation time in NMR experiments.

In the context of optical interfaces for quantum information, these decoherence mechanisms affect as well the photon quantum states used to transmit information and the optically addressable qubits. In the following, I will describe in further details what are the causes of decoherence for both platforms, and at what extent it is detrimental to the implementation of optical interfaces

1.2.2 Photonic qubits

The developments of single-photon sources have allowed to use photons as a physical support for qubits [33]. Quantum information can be encoded in various degrees of freedoms of photons, such as the orbital angular momentum [34] or time delay [35], but in this thesis, I will only consider polarization-encoded photons qubits, based on the angular momentum of spin states, as polarization states are naturally suited for coupling to the optically addressable qubits that will be considered.

Photons are unitary spin particles ($S = 1$) that allow only two projections of their spin moment $S_z = \pm 1$ along their direction of propagation, corresponding to circular right ($|+1\rangle$) or left ($|-1\rangle$) polarization respectively. The polarization states of a photon therefore represent a two-level system that can be used as a qubit that propagates at the speed of light. This polarization state corresponds to:

$$|\Psi\rangle = \cos(\theta/2)\,|+1\rangle + \sin(\theta/2)e^{i\phi}\,|-1\rangle\,. \tag{1.3}$$

A photonic analogue to the Bloch sphere, the Poincaré sphere, allows for visualizing the different polarization states: circular right ($|+1\rangle$) and left states ($|-1\rangle$) correspond to the north and south poles. Linear polarization states lie in the equatorial plane: horizontal and vertical polarization states being aligned along the x-axis, and diagonal and anti-diagonal polarization states being oriented along the y-axis. The role of an optically addressable

qubits is thus to transfer a quantum state from the Bloch sphere to the Poincare Sphere, and vice-versa.

As mentioned above, in addition to photon absorption, the decoherence of photon quantum states is detrimental to long distance entanglement. In the context of polarization-encoded photon qubits, the most important decoherence mechanisms come from the rotation of the polarization state on the Poincare sphere due to uncontrolled strain-induced birefringence in optical fibers [36]. Free-space transmission of photons could allow for longer coherence times, but requires satellite-based schemes to transmit information over long distances [37]. These depolarization mechanisms offer a first-order benchmark for evaluating the minimal separation between quantum nodes or quantum repeaters.

The photon states that will be considered in this thesis are located in the visible or near-infrared regions of the electromagnetic spectrum, as these wavelengths are best suited for transmission in optical fibers. Eventually, the photon transmission could be further improved either by engineering optical interfaces operating at 1550 nm [38], or by developing nonlinear optical systems allowing to convert higher-loss wavelengths to telecommunication wavelengths [39].

1.2.3 Optically addressable qubits

Optically addressable qubits that could be used for building optical interfaces in quantum repeaters and quantum networks consist of quantum memories that can be coupled to optical fields. The most promising way to realize this is to store the quantum information in a solid-state qubit that exhibit a non-vanishing interaction with photons. In the following, I present the requirements for building efficient optically addressable qubits that will be considered in this thesis.

Energy levels architecture: optical coupling requirements

There are two important level architectures for optically addressable qubits (see Fig. 1.2) that allow for an efficient coupling with the electromagnetic field. The first and simpler architecture (Fig. 1.2 (a)) corresponds to a simple two-level system were both states are coupled by the electromagnetic Hamiltonian and present an energy splitting in the hundreds of THz, allowing for efficient coupling with photons close to the telecommunication wavelengths. This is not the case, for example, for superconductor qubits [40], nuclear spin qubit [19] and electron spin qubits in electrically defined quantum dots [41, 42] (see next section) that present very interesting characteristics for the realization of quantum information pro-

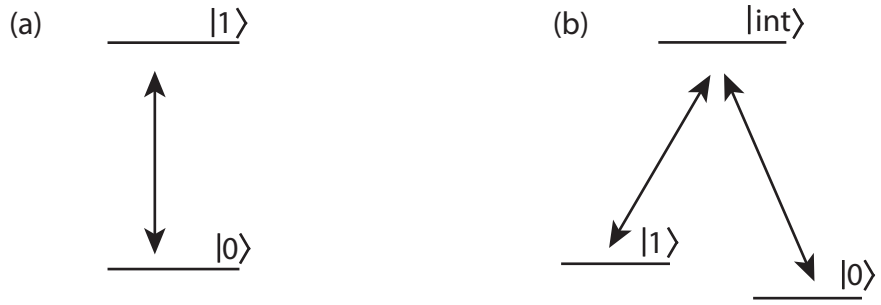

Figure 1.2 Energy levels corresponding to the two important architectures of optically addressable qubits.

cessing and storage, but present energy splittings corresponding to RF frequencies. The first two articles of this thesis mostly focuses on the study of this kind of architecture.

The second less intuitive architecture (Fig.1.2 (b)) corresponds to a Λ system where the two states forming the qubits are coupled to an intermediate metastable state spectrally separated by an energy corresponding to hundreds of THz, allowing to couple the qubit with optical fields through the interaction with this intermediate state. The advantage of this architecture, relatively to the former, is that the coherence time of the qubit is not limited by the spontaneous emission of the qubit from the excited ($|1\rangle$) to the ground ($|0\rangle$) states. The disadvantage, however, is that the schemes used to control the state of the qubit are usually more complicated, leading to a compromise between the speed and fidelity of basic operations, such as initializing, controlling, and reading-out the quantum state [43]. The last article of this thesis focuses on the study of this type of architecture, and more particularly addresses the challenge of optimizing speed and fidelity of initializing a quantum state.

Scalability requirement

The scalability of a platform represents its ability to be expanded at will. This is a very important requirement, as scaling up the number of qubits, e.g. inside a quantum computer, a storage device or a quantum network, should not compromise the proper functioning of the system. In the context of optical interfaces, the scalability requirement refers to the ability to build platforms that couples with photons presenting identical energies; otherwise photons created by one qubit might not interact with other qubits.

More precisely it is necessary that the energy splitting between the qubits be less than the intrinsic linewidth of their emission, which is typically limited by their radiative decay

through the Heisenberg uncertainty principle: $\Delta E \Delta t \geq \hbar/2$.

Coherence requirement

Entangling spatially separated quantum systems requires to keep the coherence of the shared entangled state at least through the time required for: (1) entangling the quantum state between one node and a photon; (2) transmitting this photon through the communication channel, and (3) entangling the photon state with the end-node.

Requirements (1) and (3) regard the processes involved in the entanglement of a quantum state from optical interfaces to photons, and vice-versa: it is necessary that the time required for entangling a qubit and a photon be small relatively to the coherence time of the qubit. This characteristic time depends on two factors: the light-matter coupling strength of the qubit, and the protocol used for realizing the entanglement.

These aspects are connected to the optical coupling requirement: the stronger light-matter coupling is, the more efficiently entanglement can be realized, and, eventually, optically addressable qubits could benefit from being embedded inside an optical cavity in order to enhance light-matter coupling through the Purcell effect [44, 45]. The latter factor concerns the above-mentioned aspects that it is challenging, especially in the Λ architecture, to efficiently and rapidly transfer a quantum state between solid-state and photon qubits; the last article of this thesis address this problematic.

As mentioned above, requirement (2) justifies the need for quantum repeaters, as they would allow to cancel photon qubit decoherence. It as well imposes a strict restriction on the coherence time of optically addressable qubits, as they need to preserve the coherence of the entangled quantum states over a timescale at least longer than that necessary for photons to be transfered between the two entangled nodes ($T_2 > L/c$). For qubits separated by 10 km, for example, this requires a coherence time longer than 30 μs

1.3 Potential candidates for optically addressable qubits

The requirements for optically addressable qubits being established, I will hereafter present the different candidates that have been considered over the last years, in order to understand their advantages, as well as the hurdles preventing their implementation in practical systems. Although important demonstrations of quantum information storage were realized with optical cavities [46] and spin ensembles [18], I will focus this discussion on single quantum states in solid-state platforms as they are the focus of this thesis. To conclude, I will present the system that is proposed and studied in this thesis: isoelectronic centers in semiconductors.

1.3.1 Trapped ions

Trapped laser-cooled ions can be suspended in vacuum using RF electric fields, magnetic field or optical lattice [47]; the optical selection rules of these ions allow to spectrally isolate pairs of electronic states that can be used as qubits. Impressive demonstrations of long distance entanglement were realized using trapped ions [22, 48]. The strong advantage of this system arises from the electronic states forming the qubit that exhibit strong coupling to the electromagnetic field (giving rise to typical spontaneous emission times of several ns [49, 50]), and coherence times that can be longer than 10 s [51], making them well suited for optically interfacing quantum information.

However, the *on-chip* integration of trapped ions is very challenging as it requires a complex architecture to constantly maintain the ions inside the trapping potential. In this thesis, the optical interfaces that are considered circumvent this problem, by proposing optically addressable qubits embedded inside semiconductor hosts, allowing for a much easier integration.

1.3.2 Quantum dots

Quantum dots (QDs) in semiconductors are sometimes described as artificial atoms because they confine electrons and holes in all 3 dimensions, which can thus form excitonic complexes analogue to H, He, Li, Be, B or C atoms with energy levels corresponding to electronic shells $s, p, \ldots$ [52]. The well-developed technologies of semiconductors and heterostructures growth make QDs a very appealing alternatives for trapped ions, as they can be very easily implemented inside quantum networks. There are two types of QDs that have been studied in the context of quantum information: electrically defined [41, 42] and self-assembled QDs [45, 53].

The former type is formed from the application of a voltage that locally modifies the band structure of a semiconductor, thus trapping an electron in a confined volume. This type of quantum dots, however only allows to bind one type of charge (electrons or holes) as the voltage repels the opposite charges. Consequently, band-to-band recombination of the electron is prohibited, and the electron state is not coupled to optical photons.

The latter type consist of self-assembled structures (see Fig. 1.3 (a)) that are formed during the epitaxial growth of a material with a strong lattice mismatch with its substrate (Stranski-Krastanov process) [54]. The band gap of the material forming these islands is smaller than that of the underlying host (most common QDs are formed from InGaAs in GaAs), leading to a confinement of both electrons and holes (see Fig. 1.3 (b)). These structures can therefore

trap excitons and different excitonic complexes whose radiative decay is typically very rapid ($\sim 0.5 - 1$ ns) and located in the visible or near-infrared [55]; they are therefore well-suited for building optically addressable qubits [56]. There are two important types of qubits that can be trap by a self-assembled QD: exciton qubits and spin qubits.

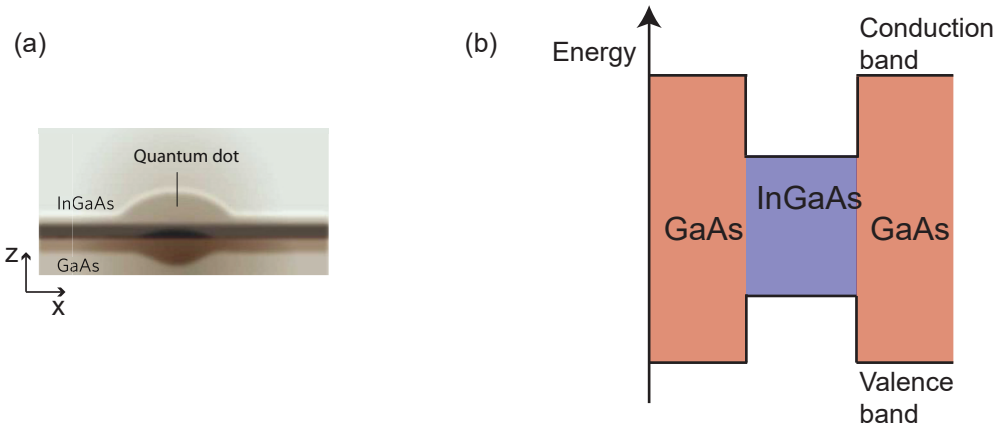

Figure 1.3 (a) Cross-section of a self-assembled InGaAs quantum dot inside a GaAs matrix. Here the growth is realized along the z-axis. (b) The smaller band gap of InGaAs than GaAs, thereby trapping charges inside the QD.

Exciton qubits

Excitons are fundamental excitations in semiconductors corresponding to the Coulomb bonding of an electron in the conduction band and a hole in the valence band. Exciton states confined in QDs exhibit discrete energy levels, and a pair of these states can thus be used for implementing qubits. Typically, exciton qubits correspond to a two-level architecture (see Fig. 1.2 (a)) formed from the coherent superposition between an exciton state ($|X\rangle$) and the vacuum state ($|0\rangle$), where the exciton has been annihilated and a photon created:

$$|\Psi\rangle = a\,|X\rangle + b\,|0\rangle\,. \tag{1.4}$$

This type of qubit was the first for which optical control of a quantum state confined in a quantum dot was demonstrated [57]. However, the coherence time of exciton qubits is limited by the spontaneous emission of excitons (typically $\sim 0.5 - 1$ ns), mitigating their usefulness in the context of quantum networks and quantum repeaters.

Spin qubits

Under a magnetic field, the spin state of an electron confined in a QD can be used to form a solid-state qubit; furthermore, coupling these electron spin states to an intermediate trion state (formed from 2 electrons and 1 hole) allow to form a Λ system necessary for realizing an optically addressable qubits corresponding to the architecture presented in Fig. 1.2 (b). The absence of radiative decay between the two electron spin states allow to extent the coherence time, relatively to exciton qubits, by at least an order of magnitude (typically ~ 10 ns [58, 59]).

The enhanced coherence time of these qubits, without affecting optical coupling, has led to the realization of entanglement between a spin qubit and a photon qubit [39, 60] which is a crucial step toward the entanglement between spatially separated spin qubits, and toward the realization of QD-based quantum networks or quantum repeaters.

The most important threat to electron spin coherence is their hyperfine interaction with nuclear spins. Recently, considerable efforts have therefore been devoted to use hole spin qubits which exhibit lower hyperfine interaction and thus longer coherence times (typically up to ~ 100 ns [61–63]). This has led to the recent realization of entanglement between spatially separated (by 5 m) hole spins [64].

Scalability of QD qubits

The most important disadvantage of implementing qubits in QDs arise from the fact that they are typically formed from $10^5 - 10^6$ atoms, making it very difficult to grow identical structures. This leads to an important inhomogeneous broadening of their emission which is detrimental to their scalability. Typically the emission from excitonic complexes confined in self-assembled QDs exhibit an inhomogeneous broadening of ~ 50 meV, although the homogeneous linewidth of single QDs is typically of the order of ≤ 50 μeV [65].

1.3.3 Nitrogen-vacancy centers in diamond

The very challenging task of growing identical quantum dots has triggered efforts in building qubits formed from spins bound to atomic-size defects in crystals. The most extensively studied impurity-based qubit is the nitrogen-vacancy (NV) center in diamond [66–68] which are formed from a substitutional nitrogen atom next to an empty lattice site within a diamond lattice (see Fig. 1.4 (a)).

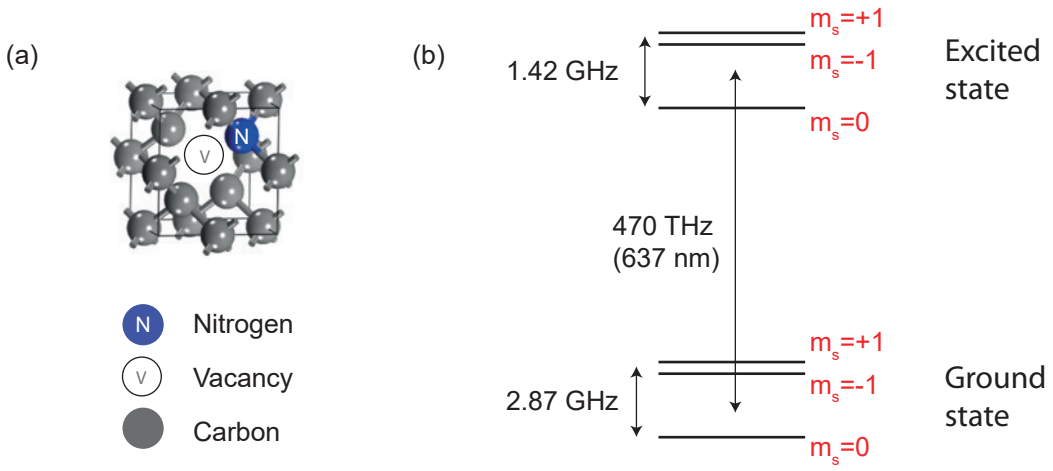

Figure 1.4 (a) NV centers consist of a nitrogen substitutional N impurities next to a vacancy inside a diamond lattice. (b) The energy levels associated to a negatively charged NV center present three $S = 1$ ground states and excited states.

Electronic spin structure

NV centers can present two charge states, neutral (NV^0) and negatively charged (NV^-), where one and two electrons respectively are bound; only the latter however has been studied in the context of quantum information and spin manipulation. The two unpaired electrons of a negatively charged NV center form a $S = 1$ triplet state whose energy level structure is presented in Fig. 1.4 (b). At zero magnetic field, the $m_s = \pm 1$ are shifted from the $m_s = 0$ states by a crystal-field of 2.9 GHz. Under a magnetic field along the quantization axis, the degeneracy between the $m_s = \pm 1$ states is lifted, allowing to isolate two states, for instance $m_s = 0$ and $m_s = -1$, in order to define a qubit.

Although the energy splitting of the qubit resides in the RF range, the ground state can be optically coupled to excited states separated by 470 THz (637 nm) as presented in Fig. 1.4 (b). These excited states and an intermediate singlet state (not shown) can be used as an intermediated state to optically initialize, control, and read-out the qubit state.

Implementation of NV centers in quantum networks

Using electron spins bound to NV centers present several important advantages for building optically addressable qubits. Firstly, as mentioned above, their atomic nature insures an important optical homogeneity necessary for scalability. Secondly the excited states allow for a coupling to optical fields. Although the light-matter coupling is typically an order of magnitude weaker than in quantum dots (leading to spontaneous emission times of ~ 10 ns

[69, 70]), the longer coherence times of electron spins largely compensates. Indeed hyperfine interaction between electrons and nuclei is much weaker in diamond, leading to coherence times up to microseconds in natural diamond and up to miliseconds in isotopically purified diamond [66]. These advantageous characteristics has led to impressive demonstrations of long distance entanglement between electron spins bound to NV centers. Recently, entanglement between NV centers separated by more than 1 km has been demonstrated [25], which is the record for solid-state qubits.

One of the most important challenge preventing the implementation of NV centers in real quantum networks or quantum repeaters concerns their *on-chip* integration. Contrary to QDs that benefit from the well-developed semiconductor growth technologies, diamond are very hard to integrate inside heterostructures, optical cavities, and other semiconductor-based devices. Furthermore, their emission is dominated by phonon sidebands of the direct recombination channel, leading to a strong probability of emitting photons at a different energy than required; consequently, the operation frequency achieved are typically several orders of magnitude lower than in QDs [25, 64].

1.3.4 Isoelectronic centers

Over the last years, significant efforts have therefore been devoted to combine the advantages of NV centers and QDs, by investigating different types of impurities in semiconductor hosts [71–73] :the atomic nature of impurities allow for a optical homogeneity as high as for NV centers, and the semiconductor host allows for an ease of implementation comparable to self-assembled quantum dots.

The work presented in this thesis follows these efforts, as it studies the potential of a novel type of impurities in semiconductors for building optically addressable qubits: isoelectronic centers. Isoelectronic centers are a particular type of impurities in semiconductors that can bind excitons and/or excitonic complexes, such as trions. They can therefore be used similarly as QDs for building exciton qubits or spin qubits, and typically exhibit a strong optical homogeneity. The complete optical control of an exciton qubit bound to these isoelectronic centers has been demonstrated recently [74], triggering the efforts behind this thesis: (1) understanding the different mechanisms governing the dynamics of excitons bound to isoelectronic centers, in order to better understand the potential of exciton qubits; and (2) evaluating the possibility to build spin qubits, by demonstrating the optical initialization of a spin qubit bound to an isoelectronic center.

1.4 Outline of the thesis

The outline of this thesis is as follows:

In Chapter 2, I present a general introduction to the physics of ICs, as well as to the system that will be studied in this thesis: N ICs in GaP and GaAs, and Te in ZnSe.

Chapter 3 presents the scientific approach and motivations underlying each article presente in this thesis.

Chapter 4 to 6 corresponds to the three articles presented in this thesis. The first two articles present an investigation of the different mechanisms underlying the dynamics of excitons bound to ICs in GaP and GaAs (capture, inter-level transfers, and radiative and non-radiative recombination) in order to understand their potential for building optically addressable exciton qubits. The last article switches to the more promising spin qubit platform and demonstrates the initialization of a hole-spin bound to a Te IC in ZnSe. The references of these articles are the following:

Article 1 - Recombinations dynamics of excitons bound to N isoelectronic centers in δ-doped GaP. *Physical Review B*, vol. **89**, 175308 (2014)

Article 2 - Dynamics of excitons bound to N isoelectronic centers in GaAs. *Physical Review B*, vol. **91**, 115201 (2015)

Article 3 - High-fidelity and ultrafast initialization of a hole-spin bound to a Te isoelectronic center in ZnSe. (Under review for *Physical Review Letters*) arXiv:1606.03338

I present a general discussion on the impact of these articles in Chapter 7, and the conclusion of this thesis in Chapter 8.

CHAPTER 2 LITERATURE REVIEW - ISOELECTRONIC CENTERS IN SEMICONDUCTORS

As introduced in the previous section, isoelectronic centers (ICs) are promising in the context of quantum information transmission, because they are atomic-size defects that naturally bind excitonic complexes with high electric dipole moments. This chapter is separated in three sections: (1) a brief introduction to the basics of ICs; (2) an overview of the IC systems that are the subject of this thesis (N in GaAs and GaP, and Te in ZnSe); and (3) the development of the theory describing how the symmetry of the different configurations of ICs allows a clear identification of the fine structure of excitonic complexes.

2.1 On the nature of isoelectronic centers

An impurity in a semiconductor is said to be isoelectronic if it presents the same outer electronic structure (valence) as the atom it replaces. The most common isoelectronic impurities in the literature, as well as those studied in this thesis, are formed from one, two, or few substitutional impurities inside a semiconductor host. Therefore, these substitutional impurities are formed from elements belonging to the same column of the periodic table as the atoms they replace.

Furthermore, isoelectronic impurities are said to form ICs when they create localized states that can trap free carriers; this is an important aspect as most isoelectronic impurities form resonant states either with the conduction or valence band that do not bind charges. It appears that only impurities that differ significantly in size and electronegativity with the host atoms they replace form localized states: for example, P impurities replacing As atoms in GaAs do not form ICs, but N impurities do [75]. Thus very few ICs have been identified, among which three will be the focus of this thesis: N in GaP and GaAs (article 1 and 2, respectively), and Te in ZnSe (article 3).

Contrary to acceptors or donors, ICs do not bring an extra charge and therefore do not generate a Coulomb electric potential inside their host. This fundamental difference between ICs and charged impurities has noteworthy consequences regarding (1) the mechanisms underlying the capture of free carriers, (2) their ability to bind different excitonic complexes, and (3) the number of impurities that can form an IC.

1- Capture of free carriers and localization

Since ICs are neutral defects, they do not bind charges through Coulomb interaction, but through more complex mechanisms whose clear identification is still debated [76, 77]. Currently, the most widely acknowledged model used to describe the interaction between ICs and free carriers (introduced in the host by doping or optical excitation) is the HTL model developed by Hopfield, Thomas and Lynch [78], according to which free carriers capture involves two sequential mechanisms:

1. Firstly, the local variation of the electronic charge density created by an IC can bind either a free electron or hole [79, 80]. ICs that are more electronegative than the atoms that they substitute act as electron traps, whereas those exhibiting a weaker electronegativity act as hole traps. Typically this first bound charge (referred to as the *primary* charge) is strongly localized over few unit cells, and the resulting interaction between the charge and nearby nuclei produces an important lattice relaxation [81]. It has been estimated that this lattice deformation mitigates almost completely the binding potential generated by the electronegativity [82] leading to the peculiar situation where the localization of this primary charge is comparable to charges bound to deep centers in semiconductor [83], but with a binding energy comparable to shallow impurties (typically $1 - 10$ meV) [84, 85].

2. Secondly, the primary charge generates a Coulomb field that extends over a much larger range than the localized potential of the neutral IC, as it decreases following a $\sim 1/r^2$ law. This Coulomb field can therefore bind a second charge of opposite sign (referred to as the *secondary* charge) thus forming a bound exciton.

The fundamental difference between the mechanisms through which charges of opposite signs are bound strongly influences the localization of wave-functions. As mentioned above, it has been estimated that the wave-function of the primary charge is strongly localized by the IC potential over few unit cells (typically few Å) [86]. On the other hand, the secondary charge bound through Coulomb interaction exhibits a much weaker localization similar to charges bound to shallow donors or acceptors. The extension of its wave-function can thus be estimated as the Bohr radius a_b, which is inversely proportional to the effective mass. For light- and heavy-holes in GaAs and GaP, for example this leads to $a_b \sim 1 - 5$ nm [86]. A schematic representation of the envelope wave-functions of a strongly localized electron and a Coulomb bound hole are presented in Fig. 2.1.

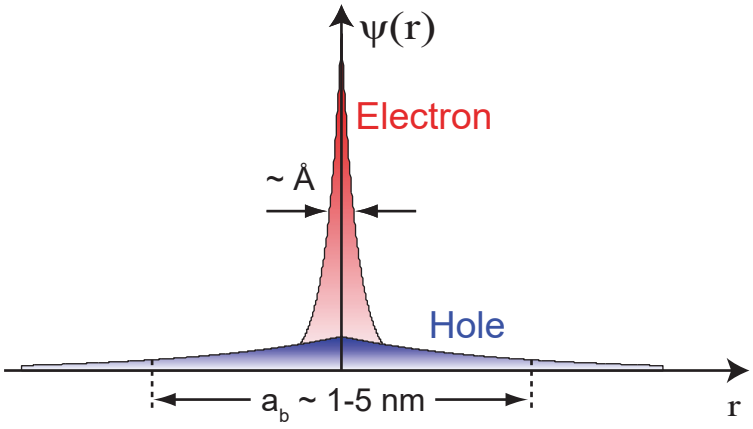

Figure 2.1 Schematic representation of the wave-function of a strongly-localized electron and a Coulomb bound hole. In this case, the IC presented corresponds to an electron trap, indicating that the IC is more electronegative than the host. For a hole acceptor, the wave-functions would be similar, but interchanged.

2- Binding of different excitonic complexes

The Coulomb potential generated by the primary charge can also, depending on the nature, configuration, and environment of the IC, bind more than one charge, leading to the binding of excitonic complexes such as charged excitons (trions) and bi-excitons [87]. This is a crucial aspect as the implementation of spin qubits bound to ICs requires the ability to bind trions (either formed from two electrons and one hole, or two holes and one electron) that can serve as intermediated states to optically control an electron (or hole) spin, as described in the previous chapter for self-assembled quantum dots. The last article of this thesis demonstrates the initialization of a hole spin bound to a Te IC in ZnSe through the fluorescence of a positive trion state.

Although bi-excitons are not studied in this work, there have been many proposals to use the radiative cascade of these excitonic complexes to generated polarization-entangled photon states [88, 89]. Thus a more extensive investigation of these bi-excitonic states in the future might be very relevant to the field of quantum information transmission.

3- Atomic configurations of ICs

ICs can be formed from an arbitrary number of impurities, but most centers that have been identified are formed from one, two or three impurities. Interestingly, the neutrality of ICs insures that, regardless of the number of impurities forming the center, the HTL model of

capture described above still holds: the short-range IC potential binds a primary charge which, in turn, binds a secondary charge (or several charges) through Coulomb interaction to form a bound exciton (or excitonic complexes).

This aspect is very important as it allows these ICs formed from more than one impurity to naturally bind excitons or excitonic complexes identically as single impurities do. The work presented in this thesis mostly focuses on ICs formed from two impurities (dyads) rather than isolated impurities, because they can be optically resolved much more easily, which is a crucial requirement to build optically addressable qubits. Indeed, assuming a uniform doping and non-interacting impurities, it is very challenging to produce samples with surface concentrations low enough to observe single-impurity ICs within the area defined by the limit of optical diffraction (typically $\sim 1\ \mu\text{m}^2$ [90]). On the other hand, the concentration of ICs formed from two impurities separated by less than a few unit cells is much lower, and can thus be much more easily achieved by epitaxy [91–93] or ion implantation [94, 95].

2.2 Description of the various types of ICs

Numerous combinations of impurities and hosts can be used to build ICs with different properties. Among these possibilities, the work presented in this thesis focuses on nitrogen ICs in GaP (Chapter 3) and GaAs (Chapter 4), and tellurium ICs in ZnSe (Chapter 5), which are briefly described in this section.

2.2.1 Nitrogen ICs in gallium phosphide

N ICs in GaP, which were historically the first type of ICs studied, are formed from one, two or few substitutional N impurities located on the anionic sub-lattice of GaP [96]. Since N atoms are more electronegative than P atoms that they substitute, they can bind an electron in a localized volume, which can subsequently bind a hole (either from the light- or heavy-hole valence band) inside a more extended volume, in accordance with the HTL model presented above.

Due to its indirect band gap, bulk GaP is a poor light emitter, because radiative recombination of excitons requires the cooperations of a phonon in order to conserve momentum. However, excitons bound to N ICs in GaP present a much higher probability of radiative recombination, because the localized potential of N-bound states are formed from states spanning the whole Brillouin zone.

This enhanced optical activity is very easily observed in PL spectra of nitrogen-doped GaP: several sharp lines associated to the radiative recombination of exciton bound to N ICs are

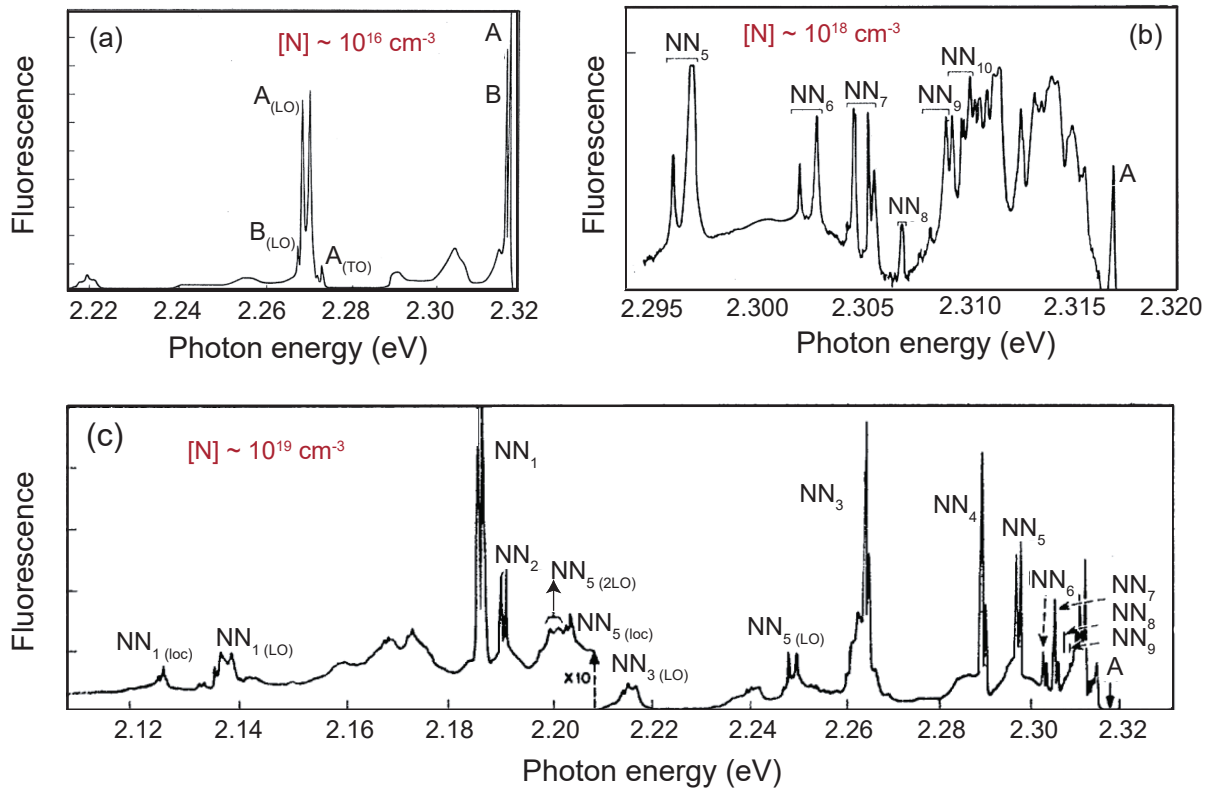

Figure 2.2 Photoluminescence spectrum of nitrogen-doped GaP for different doping concentration. Transition associated to N ICs (A, B and NN_i lines) are labeled, as well as their LO, TO, and local-mode (loc) phonon replica. [96]

.

observed below the band gap, as presented in PL spectra in Fig.2.2 (a)-(c). The N-related transitions observed on each spectrum are separated in different groups (hereafter referred to as multiplets): the shallowest multiplet is formed from two transitions, labeled the A and B lines, and is only observed at low and intermediate concentrations (A is more intense than B, and B completely disappears as the temperature is raised above $\sim$ 5 K [96]); at lower energies, several multiplets (labeled NN_i) are observed asymptotically close to the A and B lines, NN_1 being the deepest. These multiplets are only observed at intermediate and high concentrations, and their fine structure typically exhibit between 4 and 6 transitions at low temperature, e.g. NN_1 exhibit 4 non-degenerate transitions.

These multiplets have been associated to the radiative recombination of excitons bound to either single N impurities or N dyads with different inter-atomic separation [96]. A clear identification of the atomic configuration of the underlying ICs is important to evaluate their potential for building optically addressable qubits, as the lattice deformation induced by an IC

(which depends on their local symmetry in the host) strongly influences the wave-function of bound excitons (see next section) which, in turn, affects coupling to optical fields, inter-level transfers (from one excitonic state to another), non-radiative recombinations, and exciton capture time. In the following, I present a brief overview of the arguments underlying the classifications of the different N ICs in GaP as originally proposed by Thomas and Hopfield [96], as well as a brief overview of the more recent reexaminations of this classification that were proposed [86, 92, 97, 98].

Thomas and Hopfield classification

The first identification of N ICs in GaP was proposed by Thomas and Hopfield in 1966 [96]. In this work, they associated the multiplet formed from the A- and B-lines to the radiative recombination of excitons bound to single N impurities, and the NN_i multiplets to the emission of excitons bound to N dyads presenting different inter-atomic separation. NN_1 was attributed to a dyad with N atoms located in the nearest-neighbor configuration (a schematic representation of two equivalent orientations for this dyads is presented in Fig. 2.3), NN_2 to a dyad in the second nearest-neighbor configuration, and so on for increasing values of the subscript.

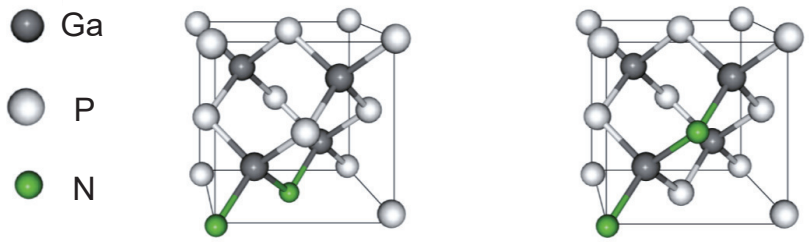

Figure 2.3 NN_1 dyads in GaP corresponding to N impurities located on nearest-neighbor sites of the anionic sub-lattice. Two different orientations are presented.

The arguments that underly their classification are based on three observations: (1) the evolution of the absorption and PL intensity of the different multiplets with N concentration, (2) the spectral position of the different multiplets, and (3) and the fine structure of the emission.

1- Variation of absorption and PL intensity with N concentration

The intensity of the different multiplets present distinct dependences with the N concentra-

tion. At low concentrations ($\sim 10^{16}$ N/cm^3), only the A- and B-lines are observed (Fig. 2.2 (a)); as the N concentration increases, the intensity of the NN_i lines increases faster than the A- and B-lines (Fig. 2.2 (b)); and at high concentrations ($\sim 10^{19}$ N/cm^3), emission from NN_i multiplets completely overcomes that of the A- and B-lines (Fig. 2.2 (b)).

This observation indicates that the shallowest multiplet formed from the A- and B-lines is associated to the recombination of excitons bound to single N impurities, and that the following NN_i are associated to excitons bound to numerous N atoms. The argument behind this association is the following. At low N concentrations, it is highly unlikely to observe two or more impurities separated by less than a few unit cells, and only single impurities are observed. As the N concentration increases, this tendency is reversed as the inter-atomic mean separation between impurities decreases; considering non-interacting N atoms, the concentration of dyads (as well as triplets and larger clusters of N) therefore increases faster, and eventually exceed that of single impurities.

Furthermore, absorption measurements (not shown here) have revealed that the absorption associated to the NN_i lines increased quadratically faster with N concentration than that associated to the A- and B-lines. Since the absorption should be proportional to the concentration of ICs, Thomas and Hopfield concluded that NN_i multiplets must correspond to the emission from N dyads.

2- Spectral positions of N-related transitions

A second clear observation from PL measurements is that the multiplets present a very low inhomogeneous broadening, and are well separated from each other. Thomas and Hopfield argued that the spectral position of every set of transitions can be used to identify the atomic configuration of the underlying IC.

Firstly, the emission energy should be related to the number of impurities forming the ICs, as the exciton binding potential is expected to increase with the number of impurities. This is consistent with the association of the shallowest multiplet observed (formed from the A- and B-lines) to single N impurities, and of the following multiplets (NN_i) to ICs formed from pairs or triplets of impurities.

Furthermore, the exciton binding energies of dyads are expected to strongly depend on their inter-atomic separation; this is based, in first approximation, on the fact that finite potential well typically exhibit binding energies inversely proportional to the square of their width. Using this approximation, Thomas and Hopfield estimated that the exciton binding energy is maximal for dyads with the lowest inter-atomic separation, and decreases asymptotically

with the inter-atomic separation toward the binding potential of the single-atom configuration (which can be viewed as a dyad with infinite separation).

3- Multiplets fine structures

That last observation that guided Thomas and Hopfield classification was that the different multiplet does not exhibit identical fine structures. These differences arise from the fact that the crystal deformation produced by N ICs breaks several symmetry elements of the underlying zinc-blende GaP lattice, thus splitting the different excitonic states into a fine structure uniquely defined by the local symmetry of the IC. Generally speaking, ICs presenting lower local symmetries present more complex fine structures. For example, the highest possible IC symmetry is that of the single impurity, and the corresponding multiplet is formed from the lowest number of transitions (two, the A- and B-lines). On the other hand, dyads present lower symmetries as their orientation breaks rotational and/or inversion symmetry elements of the host, and their fine structures typically exhibit more than two transitions.

Using their estimate of dyads separations, Thomas and Hopfield proposed an identification of the local symmetry for every dyad: NN_1 are nearest-neighbor dyads and should therefore be oriented along [1 1 0] (or any equivalent axis), which corresponds to a C_{2v} symmetry; NN_2 should be oriented along [2 0 0], corresponding to a D_{2d} symmetry; etc. Since it is possible to relate each of these symmetries to a precise PL fine structure (see the theory developed in the following section), Thomas and Hopfield could compared these expected symmetries with the observed fine structures, and did not find significant qualitative disagreements.

Reexaminations of Thomas and Hopfield classification

More recently the IC classification by Thomas and Hopfield has been reexamined both theoretically [86, 99] and experimentally [97, 98]. These reexaminations arise from the theoretical observation that the exciton binding energy associated to different dyads does not necessarily increase monotonously with their inter-atomic separation [86]. Indeed, the exciton binding energy does not only depend on dyad separation, but as well on their local symmetry inside the host lattice, as the atomic arrangement of the dyad can significantly affect the energy involved in the crystal deformation. A clear identification of the local symmetry of every dyad is therefore very important to identify conclusively their atomic configuration (separation and orientation inside the lattice).

It is necessary to reexamine the dyad symmetries identified by Thomas and Hopfield (as they were determined with imprecise estimations of inter-atomic separation) using more

elaborated investigations of the exciton fine structure through (1) application of hydrostatic pressure along different crystallographic orientations, and (2) measurement of the PL from single dyads.

1- PL measurements under hydrostatic pressure

Applying sufficiently strong uniaxial strain can modify the energy associated to the crystal deformation along precise directions, and therefore lower the local symmetry of dyads in a deterministic way. Identifying the variations of the fine structure for different orientations and magnitudes of the applied strain field has thus allowed, using geometrical arguments, to reexamine the symmetry of several dyads [97, 98]:

- Firstly, NN_2 has been reassigned to an IC formed from three N impurities (triad). The identification of transitions associated to excitons bound to a dyad in the second nearest-neighbor configuration (which was originally attributed to NN_2) is still elusive, but theoretical works have proposed that the radiative recombination of excitons bound to such ICs might be dipole-forbidden [99], and thus not observable through optical means.
- Secondly, these experimental works did not allow to conclude on the symmetry associated to NN_5 and NN_6. It is thus assumed that Thomas and Hopfield identification still holds, but further investigations are required to provide conclusive evidence.
- Finally, the orientation determined for NN_7 is not compatible with a dyad in the 7^{th} nearest-neighbor configuration, but to a more separated dyad oriented along $[a\,a\,0]$ where $a > 2$. It is thus assumed that NN_7 correspond to a dyad oriented along $[3\,3\,0]$, but further investigations are necessary to confirm this.

2- Single dyads photoluminescence

Only recently has the ability to optically isolated single dyads been demonstrated in samples with low enough N concentrations obtained either by epitaxy [92, 100, 101] or ion implantation [95]. PL studies on single emitters are very informative as they allow to determine the polarization dependence of every transition forming the exciton fine structure. The polarization pattern of the fine structure is strongly defined by the local symmetry of an IC (as will be discussed in the following section), and therefore furnishes more information to identify the symmetry of a dyad. In ensemble measurements, this polarization information is lost due to the randomization of the different possible orientations for a given dyad symmetry, e.g.

NN_1 dyads can be oriented along 12 equivalent orientations (2 of which are schematically depicted in Fig. 2.3).

These measurements have confirmed the identification of the symmetry of NN_1 and NN_4, but more detailed analysis will be required to unambiguously identify the symmetry of other ICs. NN_2 has not been observed in these samples presenting low N concentrations, indicating that, indeed, it is most probably formed from a larger number of impurities.

Current consensus

The current consensus on the atomic configurations of the different N ICs in GaP (number of atoms and orientation inside the lattice) is presented in Table 2.1. It is important to notice that the notation of Thomas and Hopfield (A- and B-lines, and NN_i) is still used to identify the different multiplet, although NN_i doest not necessarily refers to a dyad and the subscript i does not necessarily identify the inter-atomic separation.

Table 2.1 Current consensus on the different dyad configuration in GaP, as presented in Ref. [97, 98]. The first column identifies the different multiplets using Thomas and Hopfield notation [96], the second column identifies the number of atoms forming the center, and the second and third columns respectively present the local symmetry and orientation inside the host lattice of every IC. Symmetries and orientations that have not been unambiguously identified are presented between parentheses.

Multiplets	Number of atoms	Symmetry	Orientation
NN_1	Dyad	C_{2v}	[1 1 0]
NN_2	Triad	–	–
NN_3	Dyad	C_s	[2 1 1]
NN_4	Dyad	C_{2v}	[2 2 0]
NN_5	Dyad	(C_2)	[3 1 0]
NN_6	Dyad	(C_{3v})	([2 2 2])
NN_7	Dyad	C_{2v}	([3 3 0])
NN_8	Dyad	(D_{2d})	([4 0 0])
NN_9	Dyad	(E)	([4 1 1])
NN_{10}	Dyad	(C_2)	([4 2 0])
A - B	Single N	T_d	–

2.2.2 Nitrogen dyads in gallium arsenide

Defects formed from the substitution of As by N in GaAs constitute the second IC system that will be considered in this thesis. Similarly to N in GaP, N atoms are more electronegative

than the As atoms that they substitute, and they can therefore trap electrons inside a volume defined by few unit cells [86]. These bound electrons can subsequently bind holes (either from the light- or heavy-hole valence band) to form bind excitons [102, 103].

The most notable difference between the two systems is the much lower number of localized states observed in the GaAs band gap. Typical PL spectra of nitrogen doped GaAs (see Fig. 2.4) present only three sets of transitions related to N impurities [43, 102, 104]. These different sets have been associated to the radiative recombination of excitons bound to dyads in the first (NN_1), third (NN_3) and fourth (NN_4) nearest-neighbor configurations in the anionic sub-lattice; in this notation, the subscript is meant to represent the dyad separation.

This classification of the different dyad separations is still a subject of discussion: NN_3 has only been observed and identified recently [43]; and NN_1 and NN_4 were observed several decades ago [102, 104], but their identification heavily relies on theoretical calculations [86]. Observation of deeper N-related transitions (around 1.44 eV [105] and 1.48 eV [106]) have also been reported, but these transitions were not observed in the samples studied in this thesis, nor in other works using different samples [102]. Since these transitions lack clear identification, and have not been reproduce systematically, they will not be considered in this thesis.

The identification of the dyad separation and symmetry associated to $NN_{1,3,4}$ has been determine by (1) the evolution of the spectral position of the different ICs under hydrostatic pressure, and (2) identification of the exciton fine structure through PL measurements on single ICs.

1- PL under hydrostatic pressure

$NN_{1,3,4}$ correspond to the only localized state in GaAs, as all other N impurities form resonant states in the conduction band. Under the application of hydrostatic pressure, these resonant states are pushed one after the other inside the band gap allowing the observation of their PL [102]. This situation results from the fact that a strain field created by the application of hydrostatic pressure does not only modify the exciton fine structure (as presented above for GaP), but as well modifies the energy of the different energy levels of the band structure. Under the application of a strain field, the energy of the conduction band minimum increases faster (~ 10.73 meV/kbar) than that of the N ICs states ($\sim 3.5-5$ meV/kbar) [86, 102, 103], it is thus possible to observe emission from excitons bound to every configuration of IC by applying sufficient hydrostatic pressure.

A summary of estimated spectral positions for every configuration of N impurities is presented

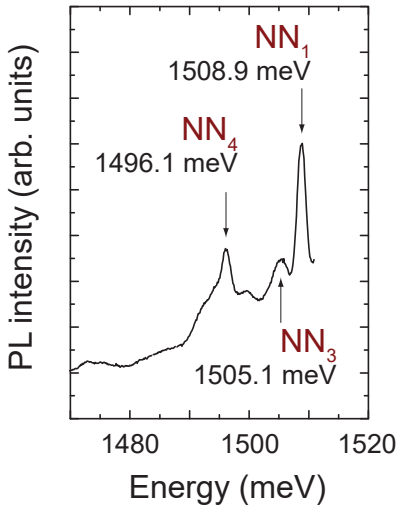

Figure 2.4 Only three transitions (labeled $NN_{1,3,4}$) are observed in PL spectra of N doped GaAs. Figure from Ref. [43].

in Fig. 2.5. NN_i transitions that are observed under hydrostatic pressure have been attributed to different configurations of dyads, but their symmetry and inter-atomic separation have not been identified clearly yet. The subscript i for these transitions thus reflect the spectral position rather than the inter-atomic separation. The last transition to appear, positioned $\sim$ 165 meV above NN_4, has been attributed to excitons bound to single N impurities. Two arguments justify this classification:

1. Similarly to N ICs in GaP, the exciton binding energy is expected to be less for single N impurities than for dyads;

2. The PL intensity of this last transition, when the hydrostatic pressure allows its observation, significantly overcomes that of any other transitions. This is consistent with the fact that, at lower N concentrations, the concentration of single impurities is much more important than that of dyads [102].

Furthermore, the important similarity between the spectral evolution of the different N ICs in GaP and GaAs (see Fig. 2.5) indicates that $NN_{1,3,4}$, which are the deepest transitions, most likely arise from dyad with the low inter-atomic separation. Similarly to GaP, the observation of PL from a dyad in the second nearest-neighbor configuration is still elusive.

2- PL on single emitters

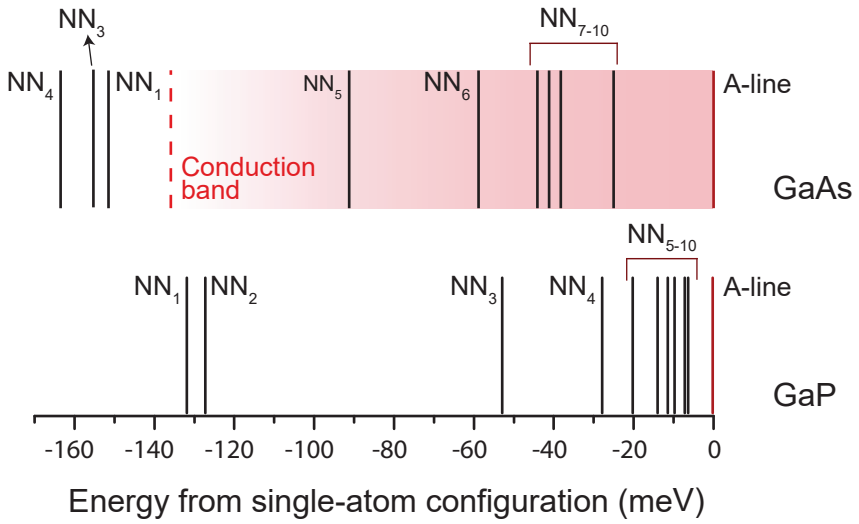

Figure 2.5 Comparison between the spectral position of the different N ICs observed in GaP and GaAs. Most exciton bound to N ICs in GaAs form resonant states in the conduction band. The only three configurations emitting below the band gap are dyads in the first NN_1, third NN_3, and fourth NN_4 nearest-neighbor configurations.

As mentioned above, the presence of N impurities breaks the symmetry of the GaAs host; this deviation from the cubic symmetry lifts the degeneracies between the different excitonic states bound to ICs, and thus allows to identify the local symmetry of dyads. However, GaAs samples that were used in this thesis present a slightly superior inhomogeneous broadening of the exciton emission preventing the observation of fine structures details in ensemble measurements. The origin of this broadening comes from the non-optimal conditions that were used for the growth of these samples. Indeed, N-related peaks in Fig. 2.3 (b) do not present multiplets, but broad lines of emission.

It is therefore necessary to optically isolate single emitters in order to observe the details of the fine structure (spectral and polarization patterns). Nitrogen dyads in GaAs where the first ICs to be optically resolve using confocal microscopy [104], and these measurements of single dyads have allowed to observe the fine structure of NN_1 and NN_4, as shown in the PL spectra presented in Fig.2.6 (a) (NN_3 has as well been isolated recently, but is not shown here). Fig. 2.6 (b) presents spatial PL map where single emitters corresponding to both IC configurations are isolated.

The polarization and spectral dependences of the exciton fine structure therefore allows to identify the symmetry underlying every dyad, which have confirmed the above classification: NN_1 is a nearest-neighbor dyad oriented along [1 1 0], corresponding to a C_{2v} symmetry; NN_3,

is a third nearest-neighbor dyad oriented along [1 1 2], corresponding to a C_s symmetry; and NN_4 is a fourth nearest-neighbor dyad oriented along [2 2 0], corresponding to a C_{2v} symmetry.

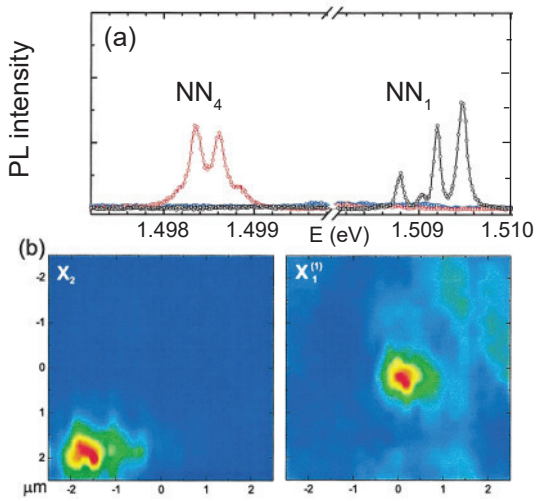

Figure 2.6 Confocal microscopy allows to optically isolate single nitrogen dyads in GaAs. Panel (a) presents micro-PL spectra of two different single emitters: $NN_{1,4}$. Both spectra are extracted from the point of highest in the underneath spatial PL maps (panel (b)) where single dyads are isolated. [104]

3- Theoretical calculations

NN_1 and NN_4 present identical fine structures, as they both exhibit a C_{2v} local symmetry. It is therefore impossible to identify their inter-atomic separation simply through their PL polarization patterns. The only identification of their separation relies on theoretical calculations of the exciton binding energy for both configurations [86]. These calculations estimated that an exciton bound to a dyad in the fourth nearest-neighbor configuration should form localized states deeper in the GaAs band gap, in comparison to a dyad in the first nearest-neighbor configuration. This non-monotonous evolution of the exciton binding energy with the dyad separation was attributed to two principal effects: lattice relaxation and multiband coupling of N bound states, both of which are strongly orientation dependent [86, 99].

Although this theoretical estimation does not provide a conclusive evidence of the separation of NN_1 and NN_4, it is the picture that will be used in this thesis. Similarly to GaP, an imprecise identification of dyad inter-atomic separation is not detrimental to the evaluation of their potential for building optically addressable qubits.

Current consensus on ICs configuration

The current consensus on the atomic arrangement associated to every set of transitions observed at atmospheric pressure is resumed in Table 2.2. The second article presented in this thesis focuses on the study of NN_1.

Table 2.2 Current consensus on the different dyad configuration in GaAs that form localized states at atmospheric pressure [43, 91, 104]. The second and third columns respectively present the local symmetry and orientation of every dyad inside the host lattice.

Multiplets	Energy (μeV)	Symmetry	Orientation
NN_1	1508.9	C_{2v}	[1 1 0]
NN_3	1505.1	C_s	[1 1 2]
NN_4	1496.1	C_{2v}	[2 2 0]

2.2.3 Te dyads in zinc selenide

The last IC system that will be considered in this thesis is formed from Te substitutional impurities in the anionic sub-lattice of ZnSe. Contrary to both previous systems, Te atoms are less electronegative than the Se atoms that they substitute [107]; consequently, Te ICs can bind holes through their short-range potential rather than electrons. Once a hole is bound, its Coulomb potential can bind a free electron to bound an exciton.

Photoluminescence from Te doped ZnSe

Contrary to N doped GaP and GaAs, PL spectra of large ensembles of ICs (macro-PL) in Te doped ZnSe (Fig. 2.7 (a)) do not present sharp emission lines that can be directly related to the radiative recombination of excitons bound to different configurations of ICs. Instead, broad lines (labeled I, II and III) are observed whose reported identification is often contradictory. The line centered around 2610 meV (I) has been attributed to the emission of excitons bound to single Te in Ref. [109–111] and to Te dyads in Ref. [112], but was as well observed in undoped ZnSe where it was attributed to the presence of dislocations [113, 114]. The broad band presenting sharp structures between 2700 and 2775 meV (II) have been attributed to Te dyads in Ref. [112], but could as well originate from phonon replica of the emission from donor-acceptor (D-A) pairs observed between 2275 and 2800 meV (III) as been reported in Ref. [113, 115]. Finally the sharp line observed at 2800 meV has been attributed to the radiative recombination of excitons bound to neutral donors ($D - X_0$) [113, 116]. It

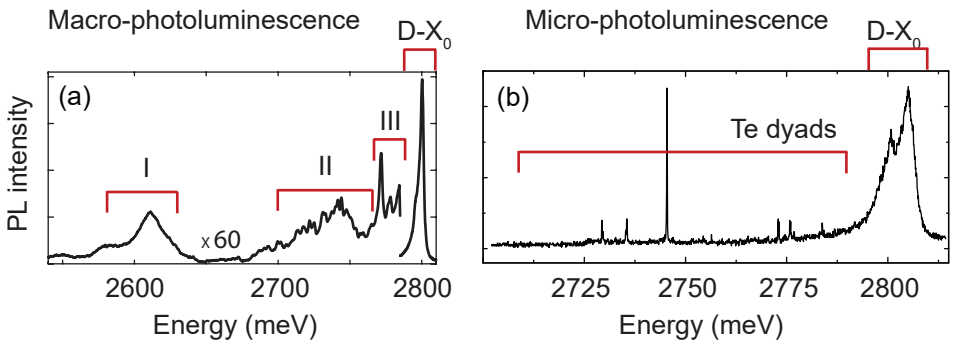

Figure 2.7 (a) Macro-photoluminescence measurements of Te doped ZnSe presents three broad lines of emission labeled I (around 2610 meV), II (between 2770 and 2775 meV), and III (between 2775 and 2800 meV). A strong peak associated to the emission from excitons bound to neutral donors is observed around 2880 meV. Figure from Ref. [108] (b) Micro-photoluminescence reveal several sharp lines associated to Te dyads in region II. Figure from the last article of this thesis.

is thus impossible, through such macro-photoluminescence spectra to identify conclusively Te-related emission lines.

On the other hand, micro-photoluminescence measurements (i.e. PL with a detection area limited by diffraction, typically 1 μm^2) reveals Te-related sharp lines in region II (Fig. 2.7 (b)). These transitions have been attributed to Te dyads presenting different inter-atomic separation [108, 117], because the Te concentration in these samples (i.e. where single ICs could be isolated) are such (typically 2500 μm^{-2}) that it would highly impossible to observe single Te impurities or Te triads [108].

Binding of different excitonic complexes

A very important aspect of Te dyads is their ability to bind different excitonic complexes: excitons, positive trions, and bi-excitons. One single dyad can bind one, two or all three of these excitonic complexes; for example, the micro-PL map in Fig. 2.8 (a) presents the emission from a an exciton (X), a positive trion (X^+) and a bi-exciton as a function of the energy and polarization of the emission. The temporal evolution of these transitions, presented in panel (b), demonstrates that these excitonic complexes are bound to the same dyad, because their spectral fluctuations (which most likely arise from local time-dependent perturbations) are simultaneous. It is still unclear what are the mechanisms that determine what excitonic complexes can be bound to a given dyad, but they most likely arise from the local environment of the dyad, e.g. the presence of a nearby charged impurity [87]. In the

following, I present a brief overview of each of these excitonic complexes.

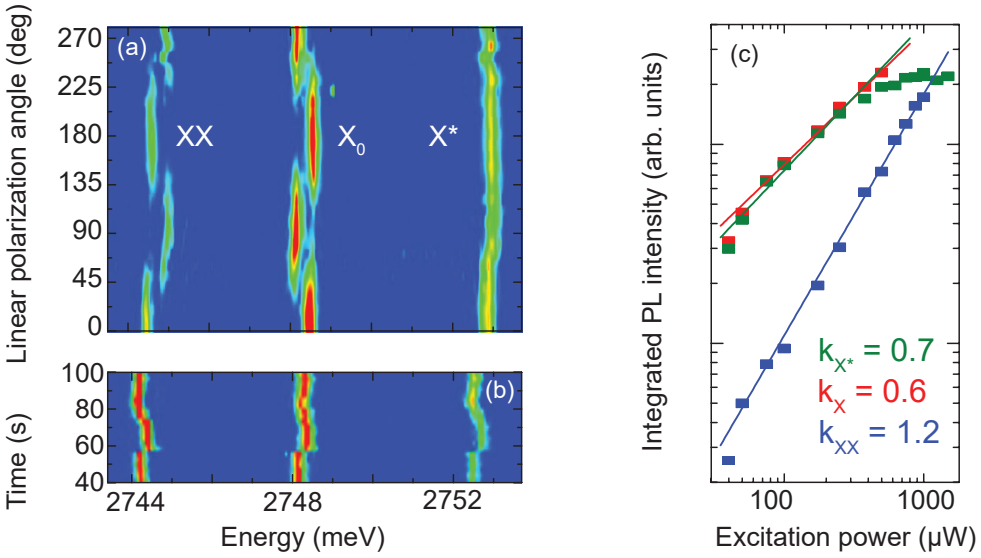

Figure 2.8 (a) Linear (b) temporal mapping of the PL intensity from a Te dyads exhibiting transitions associated to excitons (X_0), trion (X^+ and bi-exciton (XX). (c) The evolution of the exciton, trion and bi-exciton intensities with the excitation powers follows a power law $I \propto P^{k_i}$, where $k_{\mathrm{X}} = 0.6$, $k_{\mathrm{X}^+} = 0.7$, and $k_{\mathrm{XX}} = 1.2$. Figures from Ref. [108].

1- Exciton

The only fine structure that has been reported associated to the emission of excitons is formed from two orthogonal transitions polarized along the crystallographic axes [1 1 0] and [$\bar{1}$ 1 0] [108, 117]. This fine structure is associated to a dyad oriented along [1 1 0], which corresponds to a C_{2v} local symmetry (see section 2.3). Although different inter-atomic separations are expected due to the wide spectral range over which exciton emission is observed, the inhomogeneous broadening in this system, which is more important than for GaP and GaAs, makes it difficult to discriminate between the different dyad separations.

2- Trion

Trions and excitons can be distinguished by observation of their fine structure, which is expected to be very different. This difference arises from the fact that, contrary to the exciton, there is no exchange interaction between the electron and the holes forming the trion, due to the fact that the two holes form a singlet state (see section 3). Consequently, at zero magnetic field, trion emission only present one unpolarized transition as observed in Fig. 2.8 (a). This complex is of the foremost importance in the last article presented in this thesis where the initialization of a spin qubit based on the radiative decay of a trion is demonstrated

3- Bi-exciton

Excitons and bi-excitons present very similar fine structures (as observed in Fig. 2.8 (a)), but the latter can be identified by evaluating the dependence of its photoluminescence intensity as a function of the excitation power. As presented in Fig. 2.8, the intensity of every excitonic complex follows a power law $I \propto P^k$ before saturation, and the extracted exponents clearly identify a bi-exciton transitions ($k_{XX} = 1.2$) as it is twice that of the excitons ($k_X = 0.6$) and trions ($k_{k^+} = 0.7$) [87]. This is consistent with typical values observed for excitonic complexes confined in quantum dots which as well present a factor 2 between (k_X, k_{X^+}) and k_{XX} [118]. However, values of k_X, k_{X^+} and k_{XX} reported in quantum dots typically correspond to 1, 1 and 2, respectively; the difference in k_i values between quantum dots and ICs most likely arises from the apparition of new channels of radiation with the increase of the higher excitation power.

Strain-induced lifting of the LH-HH degeneracy

ZnSe samples that were used in this thesis (as well as in Ref. [108], [87] and [117]), are grown on a GaAs substrate. The slight lattice mismatch between GaAs (a = 565.35 pm) and ZnSe (a = 566.8 pm) induces a biaxial strain in the ZnSe layer that pushes the light-hole (LH) valence band 12.6 meV below the heavy-hole (HH) valence band. Consequently, only HH excitonic complexes formed from heavy-hole are observed as LH states thermalize rapidly before their radiative decay. This is not the case for N ICs in GaP and GaAs, where HH and LH excitons are quasi-degenerate and can be both observed.

2.3 Fine structure of excitons bound to ICs

PL spectra presented in the previous section clearly show that the exciton fine structure is strongly affected by the underlying local symmetry of ICs. Understanding the effect of symmetry effects is a crucial aspect of the work presented in this thesis, particularly in article 1 and 2, as the mechanisms involved in exciton recombination dynamics strongly depends on fine structure splittings and on exciton state mixing.

In the following, I present a brief overview of the theory linking symmetry and exciton fine structure.

2.3.1 Exciton wave-functions

Excitons in semiconductors are formed from the Coulomb bonding of an electron in the conduction band and a hole in the valence band. Their wave-function (Ψ) is thus given by the product of electron and hole wave-functions which, under the envelope function approximation (EFA), can be separated in a slowly varying envelope function $|\Phi_{\mathbf{R}_e,\mathbf{R}_h}\rangle$ and rapidly varying atomic functions (Wannier functions) $|\psi_{\mathbf{R}_e}\rangle$ and $|\psi_{\mathbf{R}_h}\rangle$, corresponding respectively to the electron and hole. The exciton wave-function can thus be written as:

$$|\Psi\rangle = N^{1/2} \sum_{\mathbf{R}_e,\mathbf{R}_h} |\Phi_{\mathbf{R}_e,\mathbf{R}_h}\rangle \, |\psi_{\mathbf{R}_e}\rangle \, |\psi_{\mathbf{R}_h}\rangle \,, \tag{2.1}$$

where $\mathbf{R}_{e,h}$ are atom position vectors, and N the number of atoms located underneath the envelope function.

It is unclear at what extent EFA is a good approximation in the case of excitons bound to ICs, because it relies on the hypothesis that the envelope wave-function varies slowly at the scale of the lattice constant, which is not necessarily the case for the primary charge (see Fig. 2.1). However, previous works have succeeded in accurately representing experimental exciton fine structure using EFA [91]; I shall thus use its framework in this thesis, but further investigation of its range of validity in IC systems would be relevant.

The atomic part of the electron and hole wave-functions ($|\psi_{e,h}\rangle$) can be expressed as a product of a radial function ($|R_{e,h}\rangle$), an angular function ($|\phi_{e,h}\rangle$) and a spin state ($|\chi_{e,h}\rangle$):

$$|\psi_{e,h}\rangle = |R_{e,h}\rangle \, |\phi_{e,h}\rangle \, |\chi_{e,h}\rangle \,. \tag{2.2}$$

The radial part of atomic functions $|R_{e,h}\rangle$ is very difficult to evaluate, requiring numerical techniques. Hereafter, I will thus use separation of variables, and consider only angular and spin parts of the exciton wave-function; the contribution of the radial part will simply be absorbed in free parameters that will be adapted to fit the experimental data. Although this will prevent us from calculating absolute binding energies, it will be possible to determine the energy splittings, as well as the polarizations of emission.

$|\phi_{e,h}\rangle$ states can be expressed as linear combinations of spherical harmonics ($|l,m\rangle$), and spin states $|\chi_{e,h}\rangle$ as linear combinations of spin-up and -down states ($|\uparrow\rangle$ and $|\downarrow\rangle$, respectively).

Excitons that will be considered in this thesis are formed from electrons and holes presenting s- and p-type wave-functions, respectively. Thus the angular part of electron state is simply $|0,0\rangle$, and hole states are formed from linear combinations of spherical harmonics $|1,\pm1\rangle$

and $|1,0\rangle$. It is more convenient to express angular and spin wave-functions of electrons and holes using total angular momentum states $|J,m_j\rangle$, where $\vec{J}=\vec{L}+\vec{S}$. Using this notation, the electron basis is formed from two state ($\{\alpha,\beta\}$):

$$\begin{aligned}\alpha &= |1/2,+1/2\rangle = |\uparrow\rangle \\ \beta &= |1/2,-1/2\rangle = |\downarrow\rangle\,;\end{aligned} \tag{2.3}$$

and the hole basis is formed from four states ($\{\phi_{1-4}\}$):

$$\begin{aligned}\phi_1 &= |3/2,+3/2\rangle_J = |1,1\rangle_l\,|\uparrow\rangle \\ \phi_2 &= |3/2,+1/2\rangle_J = \sqrt{\frac{2}{3}}\,|1,0\rangle_l\,|\uparrow\rangle + \sqrt{\frac{1}{3}}\,|1,1\rangle_l\,|\downarrow\rangle \\ \phi_3 &= |3/2,-1/2\rangle_J = \sqrt{\frac{1}{3}}\,|1,-1\rangle_l\,|\uparrow\rangle + \sqrt{\frac{2}{3}}\,|1,0\rangle_l\,|\downarrow\rangle \\ \phi_4 &= |3/2,-3/2\rangle_J = |1,-1\rangle_l\,|\downarrow\rangle\,.\end{aligned} \tag{2.4}$$

Here, the subscripts l and J refer to uncoupled $|l,m\rangle$ and coupled $|J,m_j\rangle$ states. $\phi_{1,4}$ correspond to heavy-hole states, and $\phi_{2,3}$ to light-hole states. $J=1/2$ states (corresponding to the split-off band) are not considered here, because, in semiconductors lacking inversion symmetry, these states are typically pushed several hundreds of meV below the LH and HH states, allowing us to ignore their contribution [119].

The exciton basis is therefore 8-dimensional (ψ_{1-8}) as it corresponds to the direct product between the electron and hole bases subspaces:

$$\begin{aligned}\psi_{1-8} &= \{\alpha,\beta\}\otimes\{\phi_1,\phi_2,\phi_3,\phi_4\} \\ &= \{\alpha\phi_1,\alpha\phi_2,\alpha\phi_3,\alpha\phi_4,\beta\phi_1,\beta\phi_2,\beta\phi_3,\beta\phi_4\}\end{aligned} \tag{2.5}$$

2.3.2 Invariant expansion of exciton Hamiltonian

In order to evaluate exciton state mixing, energy splitting and optical selection rules, it is necessary to consider the binding Hamiltonian for IC presenting all possible local symmetries. The exciton Hamiltonian used in this thesis are constructed from an invariant expansion,

based on the fact that Hamiltonians must be invariant under time-reversal, and under all symmetry operations of the underlying IC point group (i.e. it must belong to the Γ_1 representation). The former requirement insures energy conservation, and the latter arises from the fact that the ICs and their binding potential share the same symmetry elements. More details on this expansion can be found in Ref. [91, 120–122].

The exciton Hamiltonian considered is a 8×8 matrix (in order to fit the exciton basis presented above) that takes into account three interactions:

- H_e : the electron Hamiltonian;
- H_h : the hole Hamiltonian;
- H_{e-h} : the exchange interaction between the electron and the hole.

In the following I present a brief overview of these different contributions.

Electron Hamiltonian

The electron states considered are the conduction band states α and β; hence they form a two-dimensional subspace, and the electron Hamiltonian (H_e) is a 2×2 matrix. In order to adjust its dimension to the 8-dimensional exciton Hamiltonian, H_e is casted in the required form using a Kronecker product with a four-dimensional identity matrix representing the hole subspace:

$$H_e^{(8\times8)} = H_e \otimes \mathbb{1}^{(4\times4)} \tag{2.6}$$

Since the identity matrix and the Pauli matrices ($\vec{\sigma_i} = (\sigma_x, \sigma_y, \sigma_z)$) form a complete basis for 2×2 matrices, H_e can be constructed from a linear combination of these 4 matrices. However, Pauli matrices are not invariant under time-reversal, thus the only contributing term of the electron Hamiltonian is the unitary matrix:

$$H_e = E_e \mathbb{1}^{(2\times2}, \tag{2.7}$$

where E_e corresponds to the confinement energy of electrons. This Hamiltonian will be identical for all ICs symmetries, because it is the only 2×2 matrix that is invariant under time-reversal and spatial transformations.

Under a magnetic field $\vec{B}$, the electron Hamiltonian can however be further expanded, because the components of the magnetic field (B_x, B_y, B_z) transform identically to the Pauli matrices

under spatial and temporal transformations. This similarity arises from the fact that the Biot-Savart equation describing magnetic fields ($\vec{B} \propto \vec{r} \times \vec{j}$, where $\vec{j}$ stands for the density of electric current) is isomorphic to the cross-product describing angular momentum ($\vec{l} = \vec{r} \times \vec{p}$). Products of Pauli matrix and corresponding coordinates of the magnetic field ($\sigma_i B_i$, $i = x, y, z$) are therefore invariant under both time-reversal and spatial transformations, and the electron Hamiltonian under a magnetic field becomes:

$$H_e = E_e \mathbb{1} + \sum_{i=x,y,z} g_i^{(e)} \sigma_i B_i, \tag{2.8}$$

where $g_{x,y,z}^{(e)}$ are the anisotropic electron g-factors. The local symmetry of ICs can impose restrictions on the electron g-factors: for example, x, y and z directions belong to the same symmetry representation of the T_d point group (which corresponds to the symmetry of single N ICs in GaP, see Appendice A), imposing $g_x^{(e)} = g_y^{(e)} = g_z^{(e)}$; for dyads presenting a C_{2v} symmetry (e.g. NN_1 in GaP and GaAs), on the other hand, x, y and z are not equivalent (see Appendice B), leading to $g_x^{(e)} \neq g_y^{(e)} \neq g_z^{(e)}$ in general.

Since σ_z is diagonal with different sign for both elements, a magnetic field oriented along the quantization axis (Faraday configuration) lifts the degeneracy between the electron spin states α and β: this is the well-known Zeeman interaction. A magnetic field perpendicular to the quantization axis (Voigt configuration) both lifts the degeneracy and mixes electron spin states, due to the off-diagonal elements of matrices $\sigma_{x,y}$.

It is finally possible to consider the second-order diamagnetic shift proportional to $B_{x,y,z}^2$ which are also invariant under spatial and temporal transformations. The final Hamiltonian is therefore:

$$H_e = E_e \mathbb{1} + \sum_{i=x,y,z} \left(g_i^{(e)} \sigma_i B_i + \delta_i B_i^2 \mathbb{1} \right), \tag{2.9}$$

where $\delta_{x,y,z}$ are the diamagnetic shift parameters. Similarly as for g-factors, the local symmetry can impose restrictions on these parameters.

Hole Hamiltonian

The hole Hamiltonian can be determined similarly, although a basis of 16 linearly independent 4×4 matrices needs to be considered; this basis is formed from linear combinations of J matrices and their product. The dimension of H_h is further adjusted using a Kronecker product with a two-dimensional identity matrix representing the electron subspace. For the

symmetries that will be considered in this thesis, only even powers of J-matrices transform as Γ_1, and the only contributing terms are:

$$H_h = E_h \mathbb{1}^{(4\times4} + \sum_{i=x,y,z} v_i J_i^2. \tag{2.10}$$

Eventually the E_h term can be absorbed in the E_e parameter of the electron Hamiltonian, which corresponds to fixing the maximum of the valence band to $E = 0$.

This Hamiltonian takes into account the crystal-field perturbation created by the presence of the IC in the crystal (the hole Hamiltonian is usually referred to as the crystal-field Hamiltonian H_{cf}). v_i parameters are referred to as the crystal-field parameters, and describe the distortion of the lattice induced by the IC: positive values indicates a perturbation that generates a tension in the crystal, while negative values indicate a compression [123]. This Hamiltonian also takes into account the confinement effects experienced by LH and HH, because these effects are isomorphic to the diagonal part of H_{cf}.

Again, for defects presenting a tetrahedral symmetry (T_d), x, y, and z are equivalent, and the crystal-field coefficients (v_i) are all equal; for dyads presenting a C_{2v} symmetry, all coefficients are considered independently.

Similarly to the electron Hamiltonian, an external magnetic field adds terms corresponding to the Zeeman interaction (proportional to B) and to the diamagnetic shift (proportional to B^2):

$$H_h = E_h + \sum_{i=x,y,z} \left(v_i J_i^2 + g_i^{(h)} J_i B_i + \delta_i^{(h)} B_i^2 \mathbb{1} \right). \tag{2.11}$$

Exchange interaction Hamiltonian

The combination of electron and hole Coulomb interaction with the Pauli exclusion principle gives rise to the exchange interaction, which couples electron and hole spins. Its Hamiltonian is obtained through the expansion of terms involving invariant products between angular momentum operators of electrons and holes, i.e. Pauli and J matrices. This leads directly to a 8×8 matrix that does not need to be size-adjusted:

$$H_{ex} = \mathbb{1}_e \otimes \mathbb{1}_h + \sum_{i=x,y,z} a_i \sigma_i J_i + \sum_{i=x,y,z} b_i (\sigma_i J_i^3). \tag{2.12}$$

The $\mathbb{1}_e \otimes \mathbb{1}_h$ term is usually absorbed with E_e and E_h. The contribution of the last terms (b_i)

is usually negligible in comparison to a_i terms due to higher powers of the angular momentum operator (J^3) involved, and will be neglected hereafter.

Again, the local symmetry of the ICs influences the relations between the different exchange coefficients similarly as for g-factors and crystal-field coefficients. The values of the a_i parameters describes the strength of the exchange interaction along the corresponding axis, and are thus related to the overlapping of the electron and hole wave-functions along these axes: larger coefficients indicate more important overlap [91].

The influence of the magnetic field in the expansion of the exchange Hamiltonian is considered to be of second order and is neglected [120].

Exciton Hamiltonian

The total exciton Hamiltonian is formed from these three contributions, and therefore takes into account 6 free parameters at $B = 0$ T (ignoring the uniform energy shift induced by the unitary terms): $a_{x,y,z}$ and $v_{x,y,z}$. The parameters can be adjusted until the energy eigenvalues agree with the observed fine structure splitting; subsequently, the eigenvectors reveal the strength of exciton mixing for every state and allow calculation of the optical selection rules.

Although the exciton basis defined in Eq. 2.5 is very intuitive, it is usually more convenient to define bases adapted to the symmetry of the underlying IC, i.e. where the exciton states belong to single representations of the IC point group. Table 2.3 presents such symmetry-adapted bases for IC with a tetrahedral symmetry T_d (e.g. single N in GaP) and C_{2v} symmetry (e.g. NN_1 in GaP and GaAs); these are the two most important IC symmetries in this thesis.

Table 2.3 Symmetry-adapted exciton bases ψ_{1-8} for T_d and C_{2v} point group. In C_{2v}, ψ_{1-4} correspond to heavy-hole excitons, and ψ_{5-8} to light-hole excitons.

T_d		C_{2v}	
Rep.	Wave-function	Rep.	Wave-function
Γ_3	$\psi_1 = \frac{1}{\sqrt{2}}(\alpha_e\phi_4 - \beta_e\phi_1)$	Γ_1	$\psi_1 = \frac{1}{\sqrt{2}}(-\beta_e\phi_4 + \alpha_e\phi_1)$
	$\psi_2 = \frac{1}{\sqrt{2}}(\alpha_e\phi_2 - \beta_e\phi_3)$	Γ_2	$\psi_2 = \frac{1}{\sqrt{2}}(\beta_e\phi_1 + \alpha_e\phi_4)$
	$\psi_3 = \frac{1}{\sqrt{8}}(\alpha_e\phi_1 + \sqrt{3}(\alpha_e\phi_3 - \beta_e\phi_2) - \beta_e\phi_4$	Γ_3	$\psi_3 = \frac{i}{\sqrt{2}}(\beta_e\phi_4 + \alpha_e\phi_1)$
Γ_4	$\psi_4 = \frac{-i}{\sqrt{8}}(\alpha_e\phi_1 - \sqrt{3}(\alpha_e\phi_3 + \beta_e\phi_2) + \beta_e\phi_4$	Γ_4	$\psi_4 = \frac{i}{\sqrt{2}}(-\beta_e\phi_1 + \alpha_e\phi_4)$
	$\psi_5 = \frac{1}{\sqrt{2}}(\alpha_e\phi_4 + \beta_e\phi_1)$	Γ_1	$\psi_5 = \frac{1}{\sqrt{2}}(-\beta_e\phi_2 + \alpha_e\phi_3)$
	$\psi_6 = \frac{1}{\sqrt{8}}(\alpha_e\phi_3 - \sqrt{3}(\alpha_e\phi_1 + \beta_e\phi_4) - \beta_e\phi_2$	Γ_2	$\psi_6 = \frac{1}{\sqrt{2}}(\beta_e\phi_3 + \alpha_e\phi_2)$
Γ_5	$\psi_7 = \frac{i}{\sqrt{8}}(\alpha_e\phi_3 - \sqrt{3}(\alpha_e\phi_1 - \beta_e\phi_4) - \beta_e\phi_2$	Γ_3	$\psi_7 = \frac{i}{\sqrt{2}}(\beta_e\phi_2 + \alpha_e\phi_3)$
	$\psi_8 = \frac{1}{\sqrt{2}}(\alpha_e\phi_2 + \beta_e\phi_3)$	Γ_4	$\psi_8 = \frac{i}{\sqrt{2}}(-\beta_e\phi_3 + \alpha_e\phi_2)$

The hermicity of the exciton Hamiltonian (H_X) imposes that its matrix elements $H_X^{(ij)} = \langle\psi_{\Gamma_i}| H_X |\psi_{\Gamma_i}\rangle$ be scalar and thus belong to the Γ_1 representation. Exciton state mixing is therefore allowed only between states that belong to the same symmetry representation $\Gamma_i = \Gamma_j$. For example, state mixing for exciton bound to ICs presenting a C_{2v} symmetry, is only observed between heavy-hole excitons (ψ_{1-4}) and light-hole excitons (ψ_{5-8}) that belong to the same representation: $\psi_1 \leftrightarrow \psi_5$, $\psi_2 \leftrightarrow \psi_6$, $\psi_3 \leftrightarrow \psi_7$ or $\psi_4 \leftrightarrow \psi_8$. Determining the strength of this mixing requires however a complete examination of the Hamiltonian.

2.3.3 Optical selection rules

In order to compare the Hamiltonian eigenvalues with the observed fine structure splittings, it is necessary to evaluate the optical activity of every state, as the experimental technique used in this thesis rely on PL measurements. In first approximation, the coupling Hamiltonian between exciton states and the vacuum state $|0\rangle$ (where the exciton has been annihilated and a photon created) is the electric dipole operator $\hat{\mathbf{d}} = -e\hat{\mathbf{r}}$, with matrix elements $\langle\Psi_i| - e\hat{\mathbf{r}} |0\rangle$.

In the following, I evaluate the optical selection rules associated to excitons bound to IC of T_d and C_{2v} symmetry.

ICs symmetry and exciton fine structure

Typically ICs presenting lower symmetries exhibit more complex exciton fine structures, and lifting of degeneracies can be determined by diagonalizing the exciton Hamiltonian. Fig. 2.9 presents the evolution of the exciton fine structure as the symmetry of the underlying potential is lowered from vacuum (complete rotational group O(3)), to T_d (symmetry of a single substitutional impurity inside a zinc-blende lattice), and to C_{2v} (symmetry associated, among others, to NN_1).

1- O(3) symmetry: exciton in vacuum

An exciton in vacuum is invariant under every symmetry operations of a sphere, forming the O(3) group; the rotational symmetry thus insures that angular momentum of the exciton J is a good quantum number. Under this symmetry, $a_x = a_y = a_z$ and $v_x = v_y = v_z = 0$ (due to the absence of crystal-field), and only the degeneracy between the $J = 1$ triplet and $J = 2$ quintuplet is lifted. Due to the conservation of angular momentum, only $J = 1$ states are optically active (see Fig. 2.10).

2- T_d symmetry: single N in GaP

Single substitutional impurities (such as single N ICs in GaP) share the point group symmetry

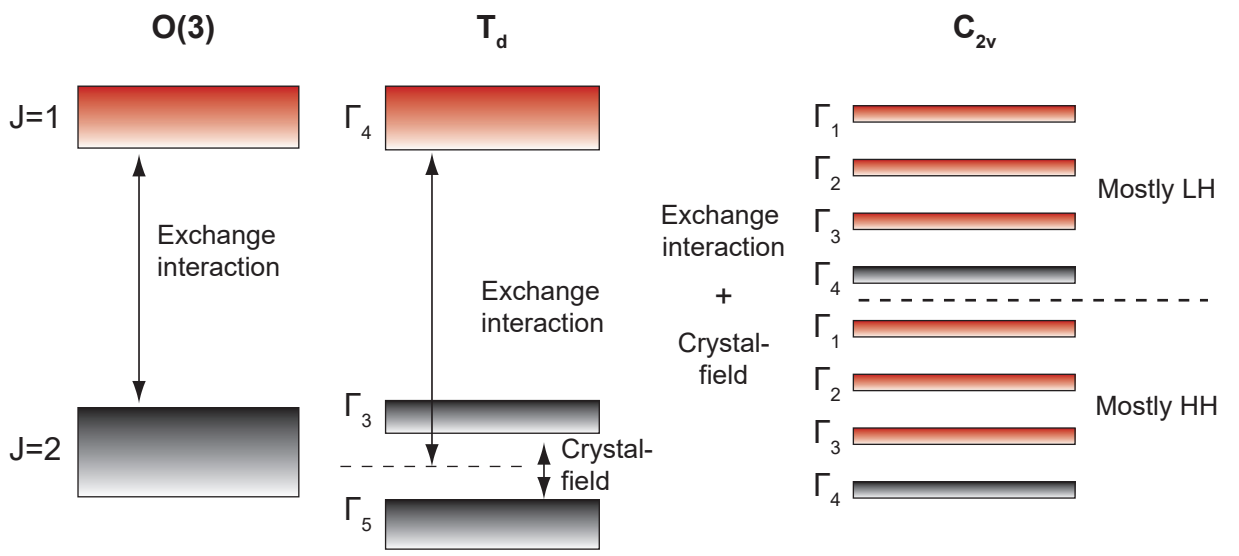

Figure 2.9 Schematic diagrams of excitons energy levels under different symmetries: O(3) is the symmetry of vacuum, T_d corresponds to a substitutional impurity inside a zinc-blende lattice, and C_{2v} is the local symmetry of NN_1 in GaAs and GaP. Red (black) levels correspond to optically active (dark) excitons.

of their host which, in the case of GaP, GaAs and Znse, corresponds to the tetrahedral symmetry (T_d). A T_d crystal-field breaks the rotational symmetry; consequently angular momentum (J) is no longer a good quantum number, as $J = 1$ and $J = 2$ excitons are mixed. The excitonic states are thus formed from admixtures of basis states ψ_{1-8} (presented in table 2.3) that belong to the symmetry representation Γ_3, Γ_4 or Γ_5.

The isotropic crystal-field ($v_x = v_y = v_z \neq 0$) lifts the degeneracy of the $J = 2$ quintuplet to form a Γ_5 triplet and a Γ_3 doublet, both of these sub-levels are not coupled to the electromagnetic field, as $\langle \Gamma_{3,5} | \vec{r} | 0 \rangle = 0$. The fine structure is completed by a bright Γ_4 triplet.

The fine structure observed for excitons bound to single N ICs in GaP is presented in Fig. 2.10 (a), and agrees with this picture. The previously identified A-line is the most intense transitions, and arises from the radiative recombination of Γ_4 excitons. In general however, Γ_5 and Γ_3 excitons can also be observed in luminescence experiments at very low temperatures ($T \sim 1.6\ K$), although with much weaker intensity, either because local perturbations (e.g. electric fields or vibrations) lower the symmetry of the system or because the second order quadrupole operator opens weaker radiative channels [96]. The observation of only one weak transition is attributed to an energy splitting too small to spectrally resolve Γ_3 and Γ_5

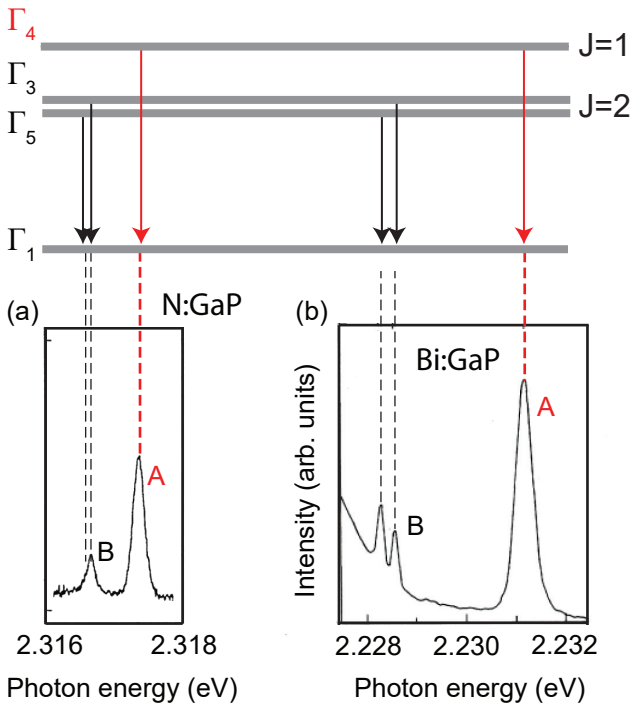

Figure 2.10 The photoluminescence of isolated N (a) and Bi (b) ICs in GaP presents one strong optical transition labeled the A-line (red), associated to the dipole-allowed radiative decay of a Γ_4 exciton, and two weak transitions labeled B-lines (black) associated to the dipole-forbidden radiative decay of Γ_3 and Γ_5 excitons (only obsever at very low temperature, $T \sim 1.6\ K$) [124]. For N impurities, the two B-lines are not spectrally resolved. [96]

transitions [124].

All three transitions can however be observed in a similar but less studied IC system formed from single substitutional Bi impurities in GaP, which confirms the expected selection rules. The exciton fine structure, presented in Fig. 2.10 (b), clearly exhibits one bright transition corresponding to the Γ_4 triplet, and two weak transitions corresponding to the Γ_5 triplet and the Γ_3 doublets [124].

3- C_{2v} symmetry: NN_1 *in GaP and GaAs*

In lower symmetries, the fine structure of the emission presents a more complex polarization dependence, because the components of the electric dipole operator (x, y, z) do not necessarily belong to the same symmetry representation. It is therefore necessary to evaluate all components of the electric dipole operator separately, with the x, y, z axes defined in Fig. 2.11: x is oriented along the dyad, z along the C_2 axis, and y is perpendicular to both x and y.

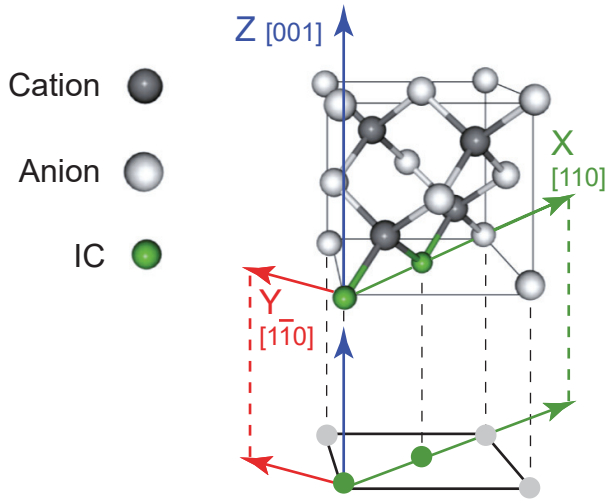

Figure 2.11 Axes of a dyad in nearest-neighbor configuration presenting a C_{2v} symmetry.

The x, y, z components of the dipole operator, for exciton states forming the C_{2v}-adapted basis (ψ_{1-8}), are presented in the third column of Table 2.4. We observe that 5 out of the 8 symmetry-adapted exciton states are optically active, while the three others have a vanishing electric dipole moment. Interestingly, the symmetry of ψ_1 (Γ_1) is compatible with the electric dipole operator, but the calculation of its coupling to the vacuum state nonetheless leads to a vanishing oscillator strength.

Table 2.4 oscillator strength of the different exciton states forming the C_{2v} symmetry-adapted basis

Representation	Wave-function	$\langle\psi_i\vert\,\hat{r}\,\vert 0\rangle$	
Γ_1	$\psi_1 = \frac{1}{\sqrt{2}}(-\beta_e\phi_4 + \alpha_e\phi_1)$	$(0,0,0)$	Heavy-hole
Γ_2	$\psi_2 = \frac{1}{\sqrt{2}}(\beta_e\phi_1 + \alpha_e\phi_4)$	$(\frac{1}{\sqrt{2}},0,0)$	
Γ_3	$\psi_3 = \frac{i}{\sqrt{2}}(\beta_e\phi_4 + \alpha_e\phi_1)$	$(0,0,0)$	
Γ_4	$\psi_4 = \frac{i}{\sqrt{2}}(-\beta_e\phi_1 + \alpha_e\phi_4)$	$(0,\frac{1}{\sqrt{2}},0)$	
Γ_1	$\psi_5 = \frac{1}{\sqrt{2}}(-\beta_e\phi_2 + \alpha_e\phi_3)$	$(0,0,\frac{2}{\sqrt{3}})$	Light-hole
Γ_2	$\psi_6 = \frac{1}{\sqrt{2}}(\beta_e\phi_3 + \alpha_e\phi_2)$	$(\frac{-1}{\sqrt{6}},0,0)$	
Γ_3	$\psi_7 = \frac{i}{\sqrt{2}}(\beta_e\phi_2 + \alpha_e\phi_3)$	$(0,0,0)$	
Γ_4	$\psi_8 = \frac{i}{\sqrt{2}}(-\beta_e\phi_3 + \alpha_e\phi_2)$	$(0,\frac{1}{\sqrt{6}},0)$	

Since the exciton Hamiltonian mixes states belonging to identical symmetry representations, the exciton fine structure of C_{2v} dyads consists of 3 pairs of optically active exciton states

presenting emission polarized along the dyad symmetry axes x, y and z, and 2 two dark states, as depicted in Fig. 2.12. These states are labeled respectively $X_{1,2}$, $Y_{1,2}$, $Z_{1,2}$ and $D_{1,2}$, where the letter refers to the axes of polarization or to dark states. In systems where the strength of the exchange interaction is comparable to that of the crystal field such as N in GaAs, exciton mixing is relatively low, and exciton states can be referred to as *mostly* HH-states (subscript 1) or as *mostly* LH-states (subscript 2).

Fig. 2.12 (a) and (b) present a polarization map of the PL intensity for an exciton bound to two different NN_3 dyads in GaAs. The observation of orthogonally polarized transitions (either along $0° - 90°$ or $45° - 135°$) is particular to the C_{2v} symmetry; the 45° offset between the two sets of polarizations is due to the different orientations of the two dyads. The orientation of each dyad is schematically depicted at the top of the figure: panel (a) presents a dyad oriented along [1 1 0] that lies inside the plane of the sample (*in-plane* dyad), while panel (b) presents a dyad oriented along [1 0 1] (*out-of-plane* dyad).

Although the perpendicularly polarized transitions identify a C_{2v} symmetry, the six dipole-allowed transitions ($X_{1,2}$, $Y_{1,2}$ and $Z_{1,2}$) are not all observed for both dyads. For in-plane dyads, the z-axis is oriented along the optical axis of detection, thus preventing the observation of $Z_{1,2}$. For out-of-plane dyads (Fig. 2.12 (b)), on the other hand, the 6 dipole-allowed transitions are experimentally accessible, because none of their symmetry axes are colinear with the detection optical axis [90]. The lower-energy z-polarized transition is however usually not observed, because exciton state mixing is too weak to provide a non-negligible oscillator strength for Z_1.

2.4 Fine structure of positive trions bound to ICs

Although the observation of negative trions and bi-excitons bound to N dyads in GaAs [43, 108] and of bi-excitons bound to Te dyads in ZnSe [108] has been reported , the only excitonic complexes studied in this thesis are positive trions bound to Te dyads in ZnSe: the last article presented in this thesis demonstrates the initialization of a hole spin qubit through the radiative decay of such a positive trion. The following treatment is therefore dedicated to determining the optical selection rules of this excitonic complex, as well as the composition of its wave-function.

2.4.1 Trions wave-functions

Trions are sometimes referred to as charged excitons, because they are formed from adding a supplementary charge to an exciton leading to either a negatively charged exciton (2 electrons

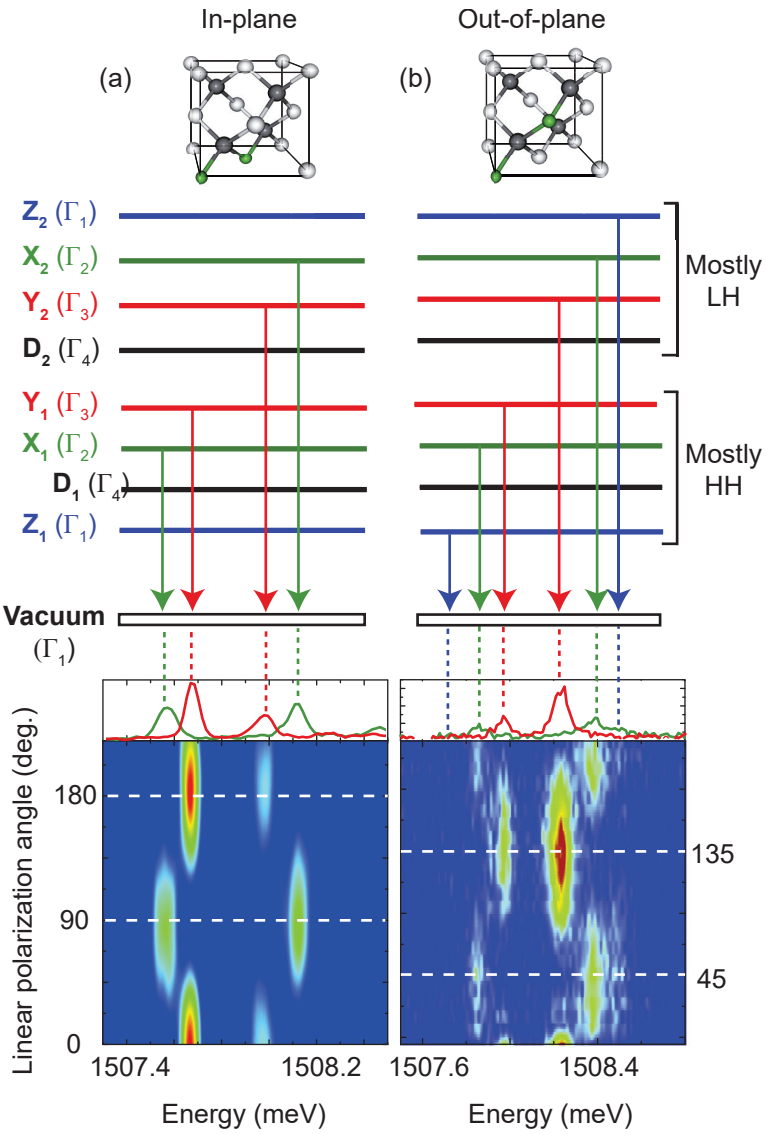

Figure 2.12 NN_1 dyads in GaAs present a C_{2v} symmetry exhibit up to 6 linearly polarized transitions, oriented along $0° - 90°$ for *in-plane* dyads (a), and along $45° - 135°$ for *out-of-plane* dyads (b). However, in-plane dyads only present 4 transitions corresponding to $X_{1,2}$ and $Y_{1,2}$, because the experimental configuration does not allow to monitor the emission from $Z_{1,2}$, and out-of-plane dyads only present 5 optical transitions due to the vanishing electric dipole moment of Z_1. [90, 125]

and 1 hole) or a positively charged exciton (2 holes and 1 electron). In both cases, the charges of same sign form a spin-free singlet state, thus the wave-function of a positive trion ($|X^+\rangle$) can be written as:

$$|X^+\rangle = |S\rangle_h \, |\chi\rangle_e \,, \tag{2.13}$$

where $|S\rangle_h$ corresponds to a hole singlet state, and $|\chi\rangle_e$ to an electron spin state.

As mentioned in the previous section, ZnSe samples used in this thesis (and in previous works on single Te dyads [87, 117]) were grown on a GaAs substrate, and the biaxial strain induced by the lattice mismatch shifts heavy-hole states ($\phi_{1,4}$) 12.7 meV below light-holes ($\phi_{2,3}$). Consequently, only PL from heavy-hole states is observed as light-hole excitonic complexes thermalize rapidly within their radiative lifetime. Furthermore, the only Te dyad symmetry that has been identified in ZnSe is the C_{2v} symmetry [91, 108, 117], and under this symmetry heavy-hole state mixing is forbidden by the symmetry (according to the hole Hamiltonian presented in Eq. 2.10). Positive trion states can therefore be explicitly written as:

$$|X^+\rangle = \frac{1}{\sqrt{2}} \left(\phi_1^{(1)} \phi_4^{(2)} - \phi_4^{(1)} \phi_1^{(2)} \right) |\chi\rangle_e \,. \tag{2.14}$$

Here, $\phi_{1,4}$ are heavy-hole states as defined in Eq. 2.4. The trion state is therefore solely determine by the electron spin state $|\chi\rangle_e$ which forms a twofold non-degenerate space $\{\alpha, \beta\}$ at $B = 0\ T$.

Contrary to excitons, the final state associated to the radiative decay of a positive trion is not $|0\rangle$, but a bound hole state. Since the hole state space is limited to heavy-hole states whose mixing is forbidden by the C_{2v} symmetry, these final states form a twofold degenerate space $\{\phi_1, \phi_4\}$ at $B = 0\ T$.

Optical selection rules

The radiative decay decay between degenerate trion and hole states gives rise to a single transition, and inspection of the angular momenta of these initial and final states allows to determine the degree of polarization of the photons generated. The angular momentum of the initial states corresponds to the spin of the electron $S = \pm 1/2$, and that of the final state correspond to the angular momentum of the hole $J = \pm 3/2$. Conservation of angular momentum therefore implies that radiative decay of trions with spin up (down) leaves a hole in a spin-up (-down) state, and generates a photon polarized circular left (right), as depicted in Fig. 2.13, schematically in panel (a) and experimentally in panel (c). The transitions from

a spin-up (-down) trion to a spin-down (-up) hole are forbidden due to the impossibility to produce $J = 2$ photons.

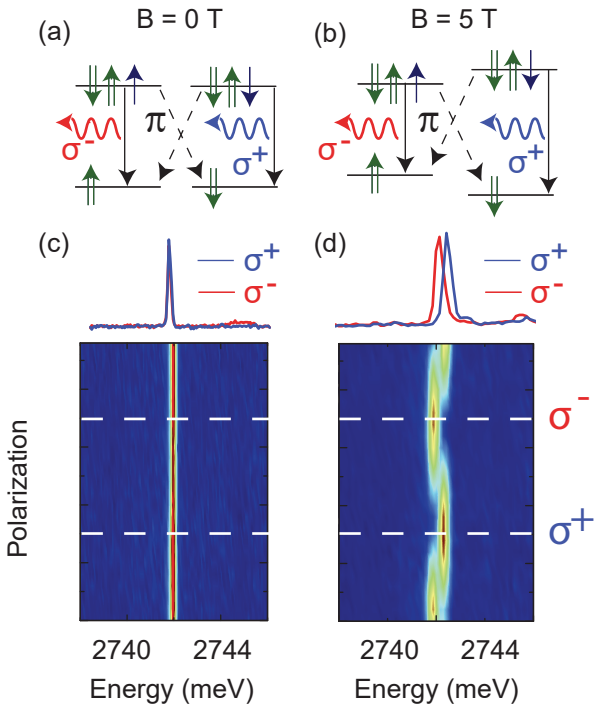

Figure 2.13 Conservation of angular momentum implies that only transitions between spin-up (-down) trions and spin-up (-down) hole states. These optical transitions are respectively polarized circularly left (σ^-) and right (σ^+). Transitions between spin-up (-down) trions and spin-down (-up) hole states are forbidden in the absence of hole state mixing.

According to the electron and hole Hamiltonians defined in the previous section, the degeneracies between trions and bound holes are lifted under a magnetic field in Faraday configuration. Since $g^{(e)} \neq g^{(h)}$ in general, there is a net Zeeman splitting between the σ^+ (circular right) and σ^- allowing to spectrally resolve them (see Fig. 2.13 (b) and (d)).

2.4.2 Determination of the charge of the trion

The last article of this demonstrates the initialization of a hole spin qubit bound to a Te dyad using a scheme based on the positive trion optical selection rules. Determining the sign of the supplementary charge of the trion is therefore crucial, and two arguments were proposed in the literature to justify the positive sign [87].

Firstly, all excitonic complexes bound to Te dyads exhibit a diamagnetic shift of $\sim 1\mu\text{eV}/\text{T}^2$ [87], which allows to assign a positive charge to bound trions. Indeed the diamagnetic shift of

a charge in a semiconductor depends on the extension of its wave-function: localized carriers exhibit a smaller diamagnetic shift than free carriers [126]. The diamagnetic shift associated to the radiative decay of trions corresponds to the difference between those of the trions and of the residual charge. If the trion were negative, the final state would be a free electron, and the variation of the wave-function extension between the initial and final states would be much greater than for the radiative decay of the exciton. However, since the diamagnetic shift of the trion is comparable to that of the exciton, I can conclude that the residual charge is strongly localized, and therefore needs to be a hole.

Secondly, the emission of the trion is usually observed at higher energy than that of the exciton (see for example Fig. 2.8 (a)), indicating that trions binding energy is lower than exciton. If trion states were negatively charged, the interaction between the supplementary charge and the exciton would lead to a stronger binding energy than for neutral excitons, because the interaction between the added electron and the strongly localized hole would be superior to electrons repulsion. It is therefore permitted to conclude that the added charge is a hole.

CHAPTER 3 SCIENTIFIC APPROACH AND MOTIVATIONS

The general objective underlying the three articles presented in this thesis is to evaluate the potential of different IC systems for hosting optically addressable qubits. The first two article evaluates the potential of N dyads in GaP (article 1) and GaAs (article 2) for binding exciton qubits, and the last article evaluate the potential of Te dyads in ZnSe for binding spin qubits (hole-spin). In the following, I present a brief overview of the scientific approach and motivations underlying the work realized in each of these articles.

3.1 Article 1 and 2: Dynamics of excitons bound to ICs

As presented in the introduction, exciton qubits are the most elementary implementation of optically addressable qubits in semiconductor nanostuctures; they were thus the first type of qubits to be studied in quantum dots (QDs) [57] as well as in ICs systems [74]. However, these exciton qubits are strongly affected by several mechanisms including charge capture, inter-level transfers, and radiative and non-radiative recombination. Extensive studies of the dynamics of excitons confined in QDs were therefore realized over the last years in order to understand the nature and importance of these different mechanisms, as well as their dependence on the semiconductor host material and other parameters such as temperature and magnetic field (see Ref. [127] and references within). A clear understanding of these mechanisms is crucial to optimize (1) coherence time (strongly dependent on thermally activated exciton inter-level transfers and non-radiative recombination) and (2) interaction with optical fields (depending on charge capture and spontaneous emission rate).

Although the mechanisms involved in exciton dynamics are expected to be similar for ICs and QDs, fundamental differences between these two systems (e.g. light- and heavy-hole near degeneracy, extension of wave-functions and binding potential) call for a reexamination. A clear understanding of these mechanisms was lacking for most ICs as previous studies were mostly limited to N dyads in GaP, and presented only qualitative or phenomenological descriptions of exciton dynamics [84, 101, 128–132].

The first two articles present a complete modeling of exciton recombination in order to identify and evaluate the importance of the different mechanisms involved in the dynamics of excitons bound to ICs. In the following I present the motivations underlying the choice of ICs systems, as well as an overview of the experimental and theoretical method used in these works.

3.1.1 Motivations underlying the choice of ICs systems

N dyads in GaP - Article 1

As presented in the previous chapter, N ICs in GaP present a wide variety of atomic configurations (number of atoms, local symmetry, inter-atomic separation...). This configuration complexity allows for an extensive examination of the role played by the ICs local symmetry and binding potential (ranging from $\sim$ 140 meV for NN_1 to $\sim$ 10 meV for N) on the dynamics of excitons.

Previous works on excitons bound to N dyads in GaP have revealed that the mechanisms involved in exciton capture and non-radiative recombination can be strongly affected by the dyad binding potential. Indeed, it has been argued that the deepest ICs (NN_{1-3}) bind excitons through the above-mentioned sequential HTL model, but that shallowest centers ($i \geq 6$) could preferentially bind excitons through the capture of free excitons or from the tunneling of excitons bound to single N [84, 132]. It is however still unclear what is the importance of each of these mechanisms, particularly for dyads presenting intermediate binding energies (NN_{4-5}). Similarly, it was argued that, depending on the exciton binding energy, exciton non-radiative recombination arises either from the escape of the hole (for NN_{1-3}) or of the whole exciton (for $i \geq 6$), leading to a free exciton state or to an uncorrelated electron-hole pair [84, 131]

Furthermore, since the symmetry of the dyad modifies the exciton fine structure splitting and state mixing, it is expected to influence as well the nature and strength of the different inter-levels transfer mechanisms. Although the presence of these mechanisms have been identified in previous works [78, 84], they have not been studied extensively yet, making it challenging to evaluate their influence on the optical properties of N dyads.

3.1.2 N dyads in GaAs - Article 2

The most important motivation for studying N dyads in GaAs resides in their enhanced coupling to optical fields in comparison to ICs in GaP. Although the localization of excitons bound to N ICs in GaP increases their oscillator strength with respect to free excitons (as presented in the previous chapter), it typically leads to PL decay times ranging in the tens of nanoseconds (up to $\sim$ 100 ns) [101, 128–130], whereas PL from excitons bound to N dyads in GaAs decays on a timescale of $\sim$ 1 ns or less [106]. In the context of optically addressable qubits, this is a very important aspect as strong electric dipole moments allow for a more efficient manipulation of exciton and spin quantum states.

Furthermore, the exciton dynamics in GaAs present a more complex behavior than in GaP,

due to the facts that (1) the characteristic times of exciton radiative decay and inter-level transfers are comparable; and (2) the magnitude of exchange interaction is similar to that of the crystal-field, leading to a more important exciton state mixing. This enhanced complexity has allowed to realize a more elaborated investigation of exciton dynamics where the different mechanisms were not considered phenomenologically, but through direct calculation of the corresponding Hamiltonian matrix elements (e.g. inter-level transfers were evaluated directly through hyperfine interaction and LA-phonon coupling Hamiltonians, rather than through generic free parameters).

3.1.3 Methods

In article 1 and 2, the method used for studying the exciton dynamics was based on a comparison of time-resolved PL (TRPL) measurements with calculated intensities obtained through balance of populations models, allowing to extract quantitative information on the different mechanisms involved during exciton recombination. Hereafter, I present a brief overview of the experimental and analytical methods used in these works.

Experimental setup

In both articles, TRPL measurements were realized with the experimental setup depicted in Fig. 3.1. The excitation was provided by a Ti:sapphire laser with a repetition rate of 80 MHz set between 780 and 840 nm. In the first article (related to GaP) the excitation frequency was doubled using second harmonic generation inside a LBO crystal allowing to excite free carriers in the GaP host, and the repetition rate was reduced to 8 MHz with a pulse picker in order to match the longer PL decay rates.

The emission was analyzed using a spectrometer with a resolution of $\sim$ 50 μeV (allowing to spectrally discriminate the different excitonic states forming the fine structure) and an avalanche photodiode (APD) with a time resolution of $\sim$ 50 ps allowing to monitor the temporal evolution of the PL intensity; CW PL measurements were realized with a CCD camera. A motorized half-wave plate (HWP) and a polarizer (POL) were used to analyze the polarization of the emission.

Measurements were realized using a confocal microscope with a spatial resolution of ~ 0.8 μm allowing to spatially resolve a restricted number of dyads (Article 1) and single dyads (Article 2), as depicted in the inset of Fig. 3.1. In Article 1, we estimated that the average number pf dyads observed was less than ten considering the nominal sheet density of N (10^{11}cm^{-2}), and the microscope resolution. The samples were held on three piezoelectric nano-positioners

allowing independent motion along x-, y-, and z- axes, and placed in a He cryostat allowing to reach temperatures down to 4 K.

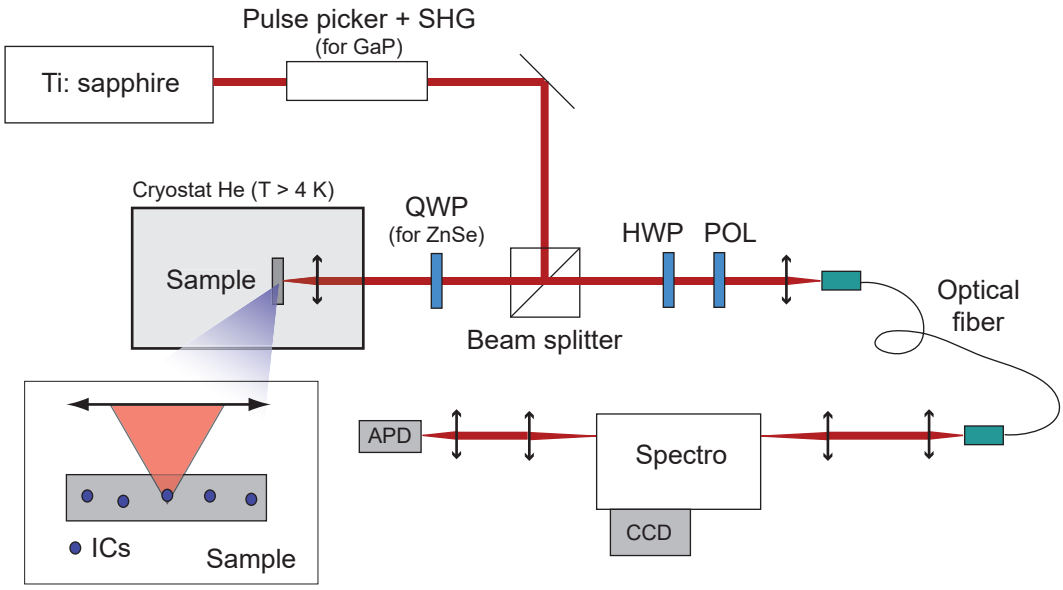

Figure 3.1 Time-resolved PL setup used in article 1 and 2. The inset presents a close-up on the sample.

Analytical model: balance of populations

Balance of population models use differential equations to describe the temporal evolution of the occupation probability for every state forming a fine structure [133]. Following each laser pulse, the exciton follows a random path between the different energy state of the fine structure (each path is not equivalent and its probability of occurrence depends on the strength of inter-level transfers) until its radiative (or non-radiative) recombination. Averaging over many repetition of the laser, we obtain occupation probabilities for all states that follow a set of differential equations whose general form correspond to:

$$\frac{\mathrm{d}n_i}{\mathrm{d}t} = -\left(\Gamma_{rad}^{(i)} + \Gamma_{nr}^{(i)} + \sum_{j\neq i}\Gamma_{tr}^{(i\to j)}\right) n_i + \Gamma_{cap}^{(i)} n_0 + \sum_{j\neq i}\Gamma_{tr}^{(j\to i)} n_j \tag{3.1}$$

$$\frac{\mathrm{d}n_0}{\mathrm{d}t} = -\sum_i \Gamma_{cap}^{(i)} n_0$$

Here, n_i corresponds to the population of the different excitonic states and n_0 to the population of photo-generated free carriers. The parameters $\Gamma_{rad}^{(i)}$, $\Gamma_{nr}^{(i)}$ and $\Gamma_{cap}^{(i)}$ correspond, respectively, to the rate of exciton radiative decay, non-radiative emission, and capture for the state (i), and $\Gamma_{tr}^{(i\to j)}$ to the inter-level transfer rate, from state i to state j.

The instantaneous PL intensity from each exciton state ($I_i(t)$) was calculated as:

$$I_i(t) = \Gamma_{rad}^{(i)} n_i. \tag{3.2}$$

The Γ parameters were then adjusted in order to fit *simultaneously* the experimental TRPL curves for all exciton states and all temperatures. This has allowed to extract quantitative values for the different parameters associated to the mechanisms involved in the exciton dynamics.

3.2 Article 3: Initialization of a hole-spin qubit bound to a Te dyad in ZnSe

Contrary to excitons, the coherence time of spin qubits is not limited by their radiative decay, and they thus represent a more promising platform for building optically addressable qubits. As presented in the introduction, considerable efforts have been devoted recently to using hole-spins rather than electron spins, because their weaker interactions with nuclear spins can lead to coherence times that are at least an order of magnitude longer [126, 134].

Te ICs in ZnSe are a natural system for hosting hole-spins as Te impurities act as hole acceptors, and, as presented in Chapter 2, they can bind positive trions necessary to realize the initialization, control, and read-out of hole-spin. The last article presented in this thesis demonstrates the initialization of a hole-spin bound to a Te dyad in ZnSe which corresponds to the first demonstration of hole-spin initialization in an impurity-based system, as previous demonstrations were only realized in QDs.

In the following I present the theoretical arguments underlying the enhanced coherence time of hole-spins in ZnSe, relatively to electron spins in III-V semiconductors, which was the most important motivation driving this work, as well as a general description of the experimental setup that was used.

3.2.1 Enhanced coherence times of hole spins in ZnSe

The most important source of spin decoherence for localized carriers, such as those bound to IC systems, arises from their interaction with nuclear spins [135, 136]. Although the dipole magnetic field created by a single nucleus is very small, the total contribution of

all the atoms located below the wave-function of a bound charge can lead to an effective magnetic field (called the Overhauser field) of several Tesla [137] (see Fig. 3.2 (b)). Even at millikelvin temperatures, this Overhauser field fluctuates from its equilibrium value with an amplitude proportional, in first approximation, to its standard deviation ($\propto \sqrt{n}$ for n nuclei). This fluctuating magnetic field interacts with the spin moment of the carriers, leading to a dephasing of spin state on a timescale of $T_2 \sim 10$ ns for electrons in InAs QDs [138]).

The magnetic interaction with nuclear spins is mitigated for hole-spins bound to Te dyads, for two reasons: ZnSe exhibits a very low concentration of nuclear spins thus limiting the Overhauser field fluctuations, and the magnetic interaction between nuclear spins and holes is much weaker than with electrons.

Nuclear spins in ZnSe

The Overhauser field is strongly reduced in ZnSe, because most isotopes of Zn, Se and Te have vanishing nuclear spins. In Tables 3.1, 3.2 and 3.3, I present the natural abundance of the different isotopes of these three elements; more than 90 % of all isotopes are spin-free. Eventually, it would be possible to isotopically purify Zn, Se and Te atoms, in order to build spin-free materials.

Semiconductors with very low concentrations of nuclear spins are very appealing for hosting spin qubits; the longest electron spin qubit coherence time observed right now is in isotopically enriched Si^{28} where electrons bound to phosphorus donors exhibit $T_2 \sim 1\ s$ [139]. Silicon however is an indirect band gap semiconductor and optical coupling is therefore strongly quenched, making it less attractive in the context of optical interfaces in quantum networks. ZnSe appears as a good compromise as it is one of the direct band gap semiconductors that offers the lowest concentration of nuclear spins. In contrast, most-studied III-V direct band gap semiconductors (GaAs and InAs) are formed from elements for which 100 % of the stable isotopes present non-vanishing nuclear spins, preventing from isotopically purifying them.

Hole spin hyperfine interaction

The advantage of using hole-spins rather than electrons resides in their p-orbitals that weakly interact with nuclear spins. The interaction between the magnetic moments of nuclei and electrons (or holes) is described by the hyperfine interaction. Initially developed in the context of atomic physics, hyperfine interaction corresponds to the interaction between the magnetic moments of nuclei and electrons. The hyperfine interaction Hamiltonian [136] for holes is identical to that for electrons, and can be separated in two terms (ignoring the

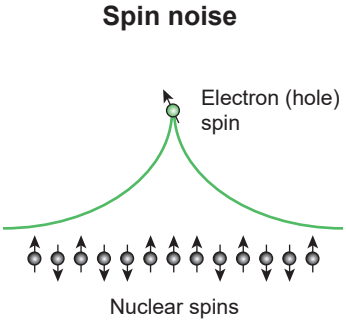

Figure 3.2 Spin noise is the result of the fluctuating nuclear magnetic moments under the wave-function of the electron (or hole).

interaction between nuclear spins and orbital motion of holes), the Fermi contact ($h^{(f)}$) and the dipole-dipole ($h^{(d)}$) interactions:

$$h^{(f)} = \frac{\mu_0}{4\pi}\frac{8\pi}{3} g_h \mu_B \sum_k g_k \mu_k (\mathbf{S}\cdot\mathbf{J_k})\delta(\mathbf{r_k}), \tag{3.3}$$

$$h^{(d)} = \frac{\mu_0}{4\pi} g_h \mu_B \sum_k g_k \mu_k \frac{3(\mathbf{n_k}\cdot\mathbf{S})(\mathbf{n_k}\cdot\mathbf{I_k}) - S\cdot I_k}{r_k^3}. \tag{3.4}$$

Here, the summation is taken over the k atoms found underneath the hole wave-function, the g_h and g_k are the hole and isotopic g-factors, $\mathbf{J}$ and $\mathbf{I_k}$ are the operators associated to the hole pseudo-spin ($\vec{J} = \vec{L} + \vec{S}$) and to nuclear spins, $\mathbf{r_k} = \mathbf{r} - \mathbf{R_k}$ is the hole position operator defined relatively to the nuclear spin position (R_k), and $\mathbf{n_k} = \mathbf{r_k}/r_k$.

The important difference here between these two contributions comes from the spatial dependence: the Fermi contact contribution vanishes everywhere in space, except at the origin of the nucleus (due to the delta function); and the dipole-dipole contribution decreases as $1/r^3$ in space.

Hole wave-functions are constructed from p-type orbitals that vanishes at the origin, contrary to the s-type orbitals forming electron wave-functions (see Fig. 3.3). Therefore, only the dipole-dipole interaction contributes to the hyperfine interaction between hole and nuclear spins. It is very challenging to evaluate what are the relative weights of $h^{(f)}$ and $h^{(d)}$ to the hyperfine interaction, but experimental works have estimated that the interaction between hole and nuclear spins is at least an order of magnitude less than it is for electrons ([134, 140]).

Table 3.1 Natural abundance of the principal isotopes of Zn

Element	Zn				
Isotopes	^{64}Zn	^{66}Zn	^{67}Zn	^{68}Zn	^{70}Zn
Spin	0	0	5/2	0	0
Natural abundance	49.2 %	27.7 %	4.0 %	18.5 %	0.6 %

Table 3.2 Natural abundance of the principal isotopes of Se

Element	Se					
Isotopes	^{74}Se	^{76}Se	^{77}Se	^{78}Se	^{80}Se	^{85}Se
Spin	0	0	1/2	0	0	0
Abundance	0.9 %	9.4 %	7.6 %	23.8 %	49.6 %	8.7 %

Table 3.3 Natural abundance of the principal isotopes of Te

Element	Te						
Isotopes	^{122}Te	^{123}Te	^{124}Te	^{125}Te	^{126}Te	^{128}Te	^{130}Te
Spin	0	1/2	0	1/2	0	0	0
Abundance	2.6 %	0.9 %	4.7 %	7.1 %	18.8 %	31.7 %	34.1 %

3.2.2 Experimental setup

The optical initialization of hole-spins was realized with an experimental setup very similar to the TRPL setup depicted in Fig. 3.1. Second harmonic generation was used to double the frequency of the Ti:sapphire in order to photo-generate free carriers in the ZnSe host (typically $\lambda \sim 420 - 440$ nm). Furthermore, a quarter-wave plate (QWP, see Fig. 3.1) was used to provide a circularly polarized excitation, and to analyze the degree of circular polarization of the PL.

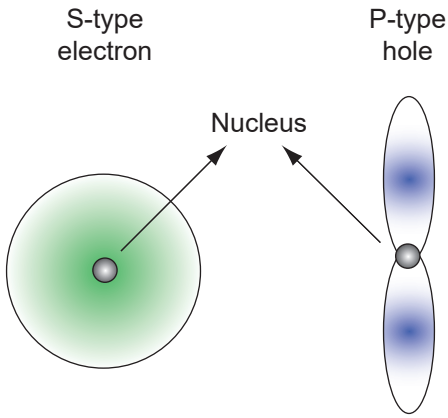

Figure 3.3 Amplitudes of s- and p-type wave-functions associated to hole and electrons, respectively. Contrary to electron, hole wave-functions typically vanish at the position of the nucleus, mitigating hyperfine interaction.

CHAPTER 4 ARTICLE 1 - RECOMBINATION DYNAMICS OF EXCITONS BOUND TO NITROGEN ISOELECTRONIC CENTERS IN δ-DOPED GAP

Authors:

Philippe St-Jean, Gabriel Éthier-Majcher, Yoshiki Sakuma, and Sébastien Francoeur

This work was published in *Physical Review B*, volume **89**, pp. 075308 (1-8), (2014)

4.1 abstract

Using time-resolved luminescence, we report on the recombination lifetime of excitons bound to nitrogen isoelectronic centers (ICs) in delta-doped GaP. For all ICs considered (A-line and NN_i, with $i = 1, 3, 4, 6$), the recombination lifetime is identical for all transitions composing the fine structure, indicating a fast transfer between all eight excitonic states. From 5 to 60 K, the lifetime decreases by three orders of magnitude and is characterized by three distinct regimes successively dominated by 1) transfers between thermally mixed bright and dark states, 2) hole escape for $i \leq 4$ or exciton escape for $i \geq 6$ and the A-line, and 3) exciton capture through hopping from single nitrogen centers to nitrogen dyads. Improving on previous population balance models to include both light- and heavy-hole states, we accurately reproduce this temperature evolution of the lifetime and quantify the radiative lifetime of all transitions, the energy position of dark states, and the exciton capture time.

4.2 Introduction

Over the last decade, considerable interest has been devoted to the implementation of single-electron and single-exciton storing devices for classical and quantum information processing. Storage has been achieved in various systems such as epitaxial quantum dots[141, 142], nitrogen-vacancy centers in diamond[143, 144] and phosphorous donors in silicon[145, 146], leading to impressive realizations such as atomic-size memories and single qubit initialization and manipulation. Further developing these systems beyond these first demonstrations remains however a challenging task: electrostatically-defined quantum dots only operates at extremely low temperatures, phosphorous donors in silicon cannot be addressed optically, self-assembled quantum dots suffer from large inhomogeneous broadening, and NV centers in diamond are difficult to integrate in semiconductor devices.

Interestingly, the number of atomic impurities, such as dopants and color-centers, is truly impressive and a number of them could be equally suitable or more advantageous that those already actively investigated. If many impurity-host systems have already been extensively studied, it was most often in a different context and with different objectives. It may therefore prove advantageous to revisit some of them, determine if they can be addressed and probed individually, and explore their respective advantages for their use as building blocks for the implementation of quantum functionalities. Isoelectronic impurities in semiconductors are interesting candidates as they may provide some of the required characteristics.

Isoelectronic centers (ICs) are isovalent impurities that can trap, through a disruption in electronic charge density of the host semiconductor crystal, either an electron or hole depending on the electronegativity of the impurity. Then, this primary charge, can trap an itinerant charge of the opposite sign to form a bound exciton. The ability to optically resolve a single IC has been demonstrated for nitrogen dyads in GaAs[104], AlAs[93] and GaP[92] and for tellurium dyads in ZnSe[108, 117]. Many of their characteristics are reminiscent of quantum dots, since they can bind excitons, biexcitons and charged excitons[87], they can be addressed both optically and electrically, and there properties can be tuned by varying the number of atoms composing the IC. However, in contrast to quantum dots, their atomic dimension provide atomically sharp emission lines free of inhomogeneous broadening and well-defined symmetries, both of which are highly desirable for most applications.

Extensively studied several decades ago for applications as light-emitting diodes, N isoelectronic centers in GaP is probably is the most well understood isoelectronic impurities in III-V semiconductors. It is also one of the most interesting impurity-host system, since a large variety of IC configurations can be directly observed: the single-nitrogen IC, several dyads with various interatomic separations[96], and other configurations involving three or more isoelectronic impurities[98] all emit within the forbidden gap. However, a critical aspect for the realization of single-charge storage and its exploitation for computation schemes is a complete understanding of the exciton dynamics, which we address in this work.

We report a detailed study of the recombination dynamics of excitons bound to various nitrogen isoelectronic centers (ICs) in gallium phosphide. Using samples with very low nitrogen concentrations, we measured the time dependence of the PL intensity of several configurations (single-atom configuration and dyads with various interatomic distances) as a function of temperature. By modeling our data with a numerical simulation of the excitonic populations and inter-level transfers, we extract fundamental parameters such as the rate of spontaneous emission, the bright and dark states splitting, the activation energy of non-radiative channels and the capture time. Many parameters describing the exciton dynamics

are quantified for the first time.

The article is organized as follows. First, we describe the nature of the samples and the effect of the IC symmetry of the excitonic fine structure. Then, we present the temperature evolution of the recombination rate for all IC configurations studied and a three-level population balance model allowing an insightful analysis of the experimental data. Finally, we discuss the dynamical processes governing the exciton dynamics.

4.3 Samples and experimental setup

Nitrogen δ-doped layers, inserted between a 1 µm GaP buffer and a 200 nm GaP cap, were grown by a low-pressure metal-organic chemical vapor deposition on undoped GaP(001) substrates. The nitrogen density of several δ-doped layers was measured by secondary ion mass spectroscopy. The δ-doped layer that we used had a sheet density of $10^{11}\,\mathrm{cm}^{-2}$. Assuming a random distribution, we estimate a dyad surface concentration of about $1\,\mu\mathrm{m}^{-2}$, which is only slightly superior to that of our diffraction-limited confocal microscope system ($\sim 2\,\mu\mathrm{m}^{-2}$). Extensive details on the growth technique, characterization of the samples, and calculation of the concentrations are presented in Ref. [92, 100]. In contrast to previous work on nitrogen ICs in GaP[128–130], the measurement presented in this work were obtained on very small ensemble of emitters, which will allow a much deeper analysis of the exciton dynamics.

Time-resolved photoluminescence (PL) measurements of exciton bounds to various nitrogen isoelectronic centers were performed at temperatures ranging from 5 to 60 K. Excitation was provided by a frequency doubled 1 ps mode-locked Ti:sapphire laser set at 840 nm. To access relatively long lifetimes, the laser repetition rate was reduced to 8 MHz using a pulse picker. The time-dependence of the PL signal was analyzed using a spectrometer with a spectral resolution of 50 µeV and an avalanche photodiode with a time resolution of less than 50 ps. A motorized $\lambda/2$ wave plate and a polarizer were used to analyze the polarization of the emission.

4.4 IC configurations and excitonic fine structures

The nitrogen ICs studied in this work are shown in Figure 4.1. The A-line corresponds to excitons bound to isolated nitrogen atoms and NN_i refers to exciton bound to nitrogen dyads of various interatomic separations and symmetries. This assignment follows the one proposed in Ref. [96], where the lowest energy transition (NN_1) is assigned to nearest-neighbor nitrogen atoms on the anionic sublattice. At higher energies, we observe the third nearest-neighbour dyad (NN_3), the fourth (NN_4), the sixth (NN_6), and, finally, the single atom configuration

at 2.316 eV. The fine-structure of each configuration is described in the following section. We do not observe transitions associated to NN_2 and NN_5 in these δ-doped layers. We attribute this to their particular configuration[98] and symmetry[96, 97], which remain to be unambiguously determined from single emitter studies.

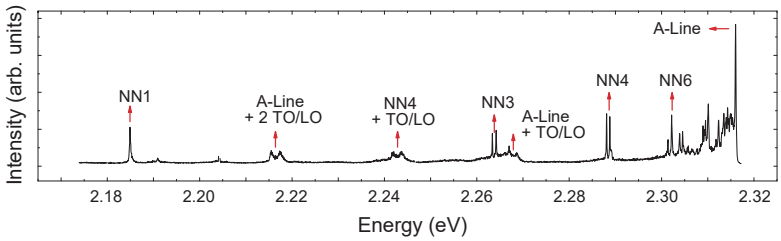

Figure 4.1 Photoluminescence spectrum measured at 30 K. The sharp lines correspond to the emission from ICs : single-atom configuration (A-Line) and dyads (NN_i). Phonon replica of the A-Line and NN_4 are also observed.

The excitonic fine structure is determined by the electron-hole exchange interaction, which splits bright $J = 1$ triplet states and dark $J = 2$ quintuplet states, and the crystal field in the vicinity of the isoelectronic center which splits and mixes bright and dark states. The observed fine-structure is uniquely determined by the symmetry of the center and can be accurately modeled using an invariant expansion.[91] The symmetry of dyad configurations was previously analyzed[97] and our polarization-resolved PL measurements are consistent with these identifications. Because of the crystal field, the exciton total angular momentum J does not provide a rigorous description of quantum states and symmetry-adapted representations should be used[91]. However, since the exchange interaction dominates the crystal field, we use the notation $J = 1$ or $J = 2$ to bring out the main component of these mixed state. This will be helpful for the discussion of the relative oscillator strength and the lifetime of various states.

The T_d symmetry of the single nitrogen atom configuration in GaP does not lift the degeneracy of the $J = 1$ triplet states and only a single bright and unpolarized transition (A-line) is observed. $J = 2$ states split into a doublet and a triplet and both states are not radiatively coupled to the ground state. However, at very low temperatures, previous works have measured a single unresolved and unpolarized transition associated to these $J = 2$ states (B-line). The presence of this transition is attributed to the spontaneous emission that becomes faster than the thermally activated exciton transfer to higher energy bright states. It remains unclear if this emission arises from a quadrupole transition or a local symmetry perturbation.

Due to their lower symmetry, the fine structure of dyads is richer. For instance, NN_1 is of C_{2v} symmetry and the degeneracy of all excitonic states is lifted, leading to a fine structure composed of 8 individual states : one set of states ($B_{X,Y,Z}$) leading to *bright* transitions, one set ($W_{X,Y,Z}$) leading to relatively *weak* transitions, and two unobservable *dark* states ($D_{1,2}$). All allowed transitions are linearly polarized and the subscripts X, Y, and Z represent polarizations along [110], [1$\bar{1}$0], and [001], respectively. Since the nitrogen atoms are located in (001) plane, C_{2v} dyads can only be oriented along [110] and [1$\bar{1}$0], implying that only four out of the six transitions can be observed: $B_{X,Y}$ and $W_{X,Y}$.

Figure 4.2(a,b) shows the intensity of these four transitions as a function of energy and linear polarization angle at 4 K. Two bright transitions are observed at high energy ($B_{X,Y}$) and two weak transitions ($W_{X,Y}$) at lower energies. The intensity difference can be explained by considering the dominant angular momentum component of these four states. The high energy states $B_{X,Y}$ evolved directly from $J = 1$ states and therefore have a strong allowed component. In contrast, $W_{X,Y}$ evolved from $J = 2$ states and have become allowed by the mixing of some $J = 1$ component induced by the low-symmetry crystal field associated with the dyad. The last two states, $D_{1,2}$, do not mix and remain strictly forbidden. Their spectral position is unknown, but the analysis of the PL dynamics will reveal that they are below $W_{X,Y}$ and that their energy position depends on the interatomic separation of the dyad.

The relative intensity of B and W transitions depends on temperature. At 30 K, the PL spectra of NN_1 shown in Fig. 4.2(c,d) reveals that only $B_{x,y}$ transitions can be observed. The complete evolution of the intensity of $B_{X,Y}$ and $W_{X,Y}$ transitions with temperature is presented in Fig. 4.2(e). Similarly to the case of the isolated nitrogen low-energy B-line, the rapid quenching of the low energy transitions W with temperature can be explained by a fast and effective exciton transfer, activated by temperature, to high-energy bright states. Above 30 K, the intensity of $B_{X,Y}$ decreases because of thermally activated non-radiative processes that will be discussed in the next sections.

Similar results were obtained for all other dyad configurations: sets of bright and weak transitions separated by about 1 meV were observed at low temperatures while at higher temperatures only bright transitions remained.

As mentioned earlier, the nitrogen dyad surface density was slightly above the highest density that could be optically resolved. Accordingly, no polarization contrast was expected from measurements on small ensembles of nitrogen dyads. The large contrast observed for all transitions associated to NN_1 (shown in Fig. 4.2) and NN_3 (not shown) likely results from the non-equivalence between the [110] and [1$\bar{1}$0] directions in the surface dynamic during nitrogen deposition. Similar effects have been reported for MBE-grown III-V and II-VI semiconductors

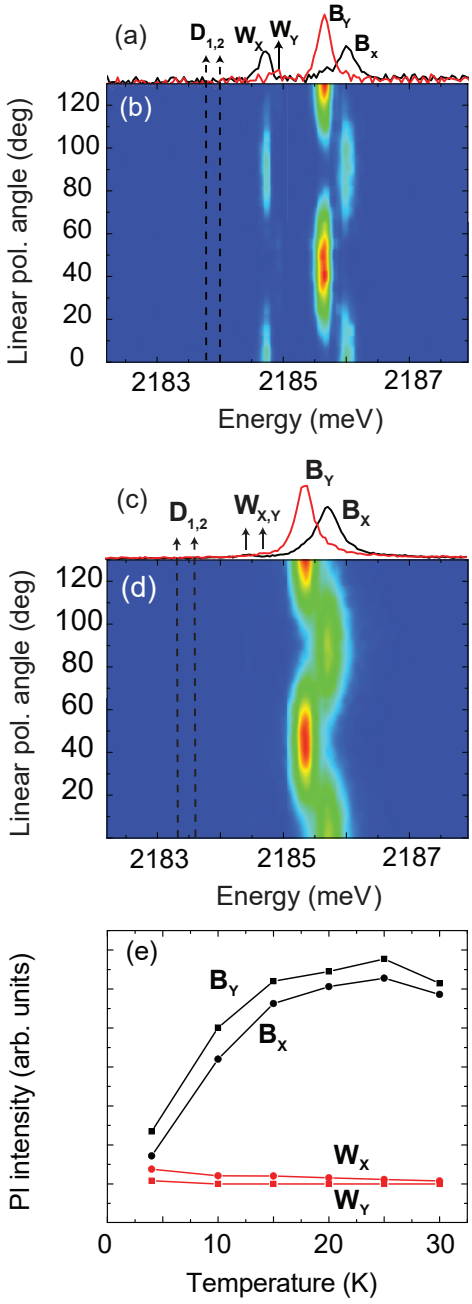

Figure 4.2 PL intensity as a function of energy and polarization for dyad NN_1 at (a,b) T = 4 K and (c,d) T = 30 K. The attribution of all excitonic transitions is presented in figures (a) and (c) where the black and red curves spectra show the PL polarized at 0º and 90º, respectively. (e) PL intensity as a function of temperature for bright ($B_{x,y}$) and weak ($W_{x,y}$) transitions. Dark transitions ($D_{1,2}$) are not observed.

[147] and for nearest-neighbour Te dyads in δ-doped ZnSe layers[117]. Interestingly, no polarization contrast could be observed for NN_4 and NN_6, indicating that this effect depends on the interatomic separation of dyads.

4.5 Excitonic recombination regimes

We proceed with the description of the time-dependence of the photoluminescence. The first important aspect is that all transitions composing the excitonic fine structure exhibited exactly the same time dependence. For example, the dynamics of all four transitions shown in Figure 4.2(a) for NN_1 were independently measured and were found to be identical at every temperature. This was also the case for all other dyads studied. This result indicates that the transfer rate between these states is much faster that the radiative lifetimes associated to each of these levels. This allows us to easily compare the recombination dynamics of various nitrogen dyads using only one decay curve for every configuration. Furthermore, in contrast with previous measurements made on samples with much higher nitrogen concentrations, the lifetime did not exhibit any variation with excitation intensity.[128]

Figure 4.3 (a) shows the measured decay time of the luminescence from NN_6 at 10, 28, and 60 K. To extract quantitative information, these intensity curves were modeled with the sum of an exponential rise term and a bi-exponential decay (red curves). Three characteristics times were thus obtained: the rise time τ_r, the short decay time τ_s, and the long decay time τ_l. The rise time, representing the characteristic time of capture of the exciton, ranges between 400 ps and 600 ps. This capture time is not affected by temperature and does not vary with the dyad configuration. However, the time dependence of the intensity varies significantly with temperature. At $T = 10$ K, a bi-exponential behavior is clearly observed with a short decay time (τ_s) of 3.0 ns and a longer decay time (τ_l) of 176 ns. As temperature is increased to 28 K, two effects are easily noticed. First, the short decay component is overtaken by the long decay component and a mono-exponential decay is observed. Second, the long decay time quickly drops from 176 ns to 16.5 ns. At 60 K, τ_l is further reduced and reaches a maximal value of 0.4 ns, which is very similar to the rise time.

The temperature evolution of the recombination rate attributed to the the longer decay ($\Gamma_l = {}^1/_{\tau_l}$) is presented in panel (b) of Figure 4.3. As the temperature is raised from 5 to 60 K, three distinct regimes are clearly observed. In regime I, at lowest temperatures, a bi-exponential decay is observed. Upon increasing the temperature, the importance of τ_s quickly vanishes and τ_l dominates. As shown in Fig. 4.3, the emission rate $\Gamma_l = \tau_l^{-1}$ increases relatively slowly up to 25 K. This behavior is typical of a recombination dynamic driven by thermally mixed allowed and forbidden states, as has been observed for CdSe

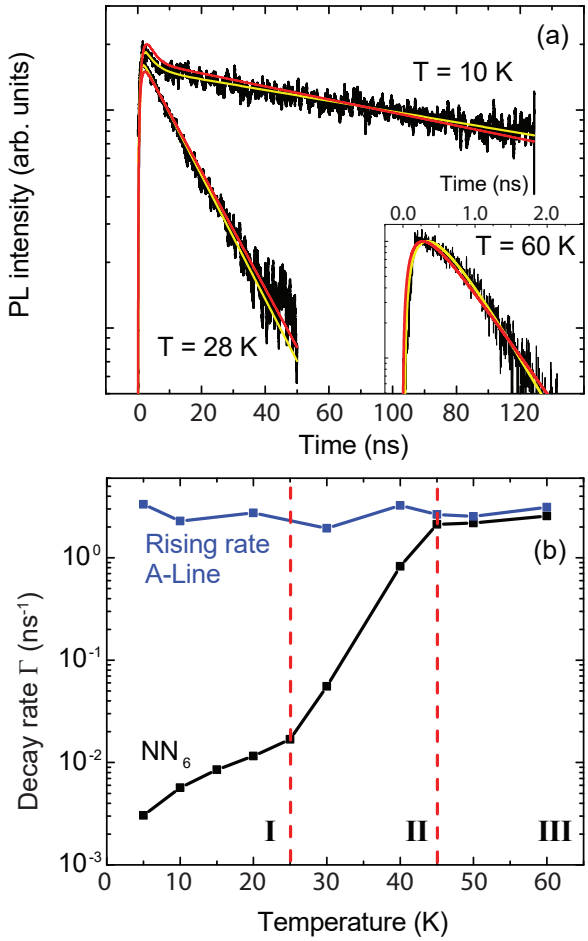

Figure 4.3 (a) Temporal dependence of the PL intensity of NN_6 at T = 10, 28 and 60 K. The red curves represent a single exponential intensity rise followed by and a single- or bi-exponential decay and the yellow curves represent calculated PL decay curves, obtained by the balance of populations model presented in section V, that best fitted the data. (b) The black curve shows the emission rate, $\Gamma_l = \tau_l^{-1}$, of NN_6 as a function of temperature and the blue curve shows the inverse of the rise time of the PL from excitons bound to isolated nitrogen atoms (A-line). The vertical lines separate the three PL decay regimes discussed in the text.

quantum dots[133] and for Te ICs in ZnSe [117]. A theoretical model describing the origin of both the slow and the fast components have been developped by Labeau et al[133]. However, in contrast with these two systems, our system involves degenerate heavy- and light-hole bands and twice the number of levels participate in the time dynamics. Furthermore, the temperature evolution of the intensity of the different transitions forming the fine-structure (Fig. 4.2 (e)) clearly shows that a transfer between B and W states can not be neglected and that it has to be taken into account. Therefore, a more complete model is necessary to properly described our data, which will be presented in the next section.

In regime II, the time decay of the luminescence is mono-exponential and, as a function of temperature, Γ_l increases exponentially. This increase is associated to the thermal-activation of competing recombination mechanisms. To explain the quenching of the luminescence intensity with temperature[148], three mechanisms were suggested : 1) the escape of the whole exciton, 2) the escape of the loosely bound hole, leaving a single bound electron, and 3) the complete unbinding of the exciton, resulting in a free electron and a free hole. The analysis of the data with the model presented in the next section will allow extracting an activation energy and determination of the dominant mechanism as a function of the dyad interatomic separation.

Finally, in the third regime, a plateau is observe as Γ_l reaches a maximum value of $2.5\,\mathrm{ns}^{-1}$, corresponding to a lifetime of 400 ps. This lower lifetime limit coincides with the rise time of the luminescence of the A-line. This suggests that, in regime III, the recombination dynamics of NN_6 is dominated by the capture of excitons by single-atom ICs followed by their hopping to the dyad. Hopping between nitrogen dyads has already been observed[149] and it has been demonstrated that hopping from single nitrogen atoms is an important populating mechanism of dyads[132, 150]. Although hopping in GaP:N is efficient for distance over at least 10 nm, the very low dyad density of our samples makes inter-dyad hopping negligible. However, as the nitrogen surface density is three orders of magnitude higher, hopping from single-atom ICs is most likely.

4.6 Time dynamics model

A population balance model is developed to analyze and explain the time dynamics of the photoluminescence intensity as a function of the temperature. To reduce complexity and limit the number of parameters required, the proposed model groups into a single level all excitonic states with similar characteristics, therefore requiring three independent excitonic levels instead of eight. These levels and the population transfer processes considered are shown in figure 4.4.

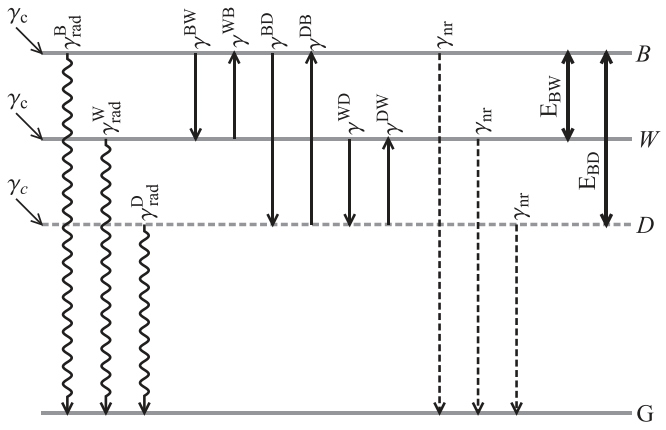

Figure 4.4 Three-level model used for the analysis of the exciton dynamics. All transfer processes considered (γ) are described in the text and E refers to energy difference between the three excited levels.

The first level B is formed from the three bright states $B_{X,Y,Z}$ located at high energy, the second level W is formed from the three weak states $W_{X,Y,Z}$ of intermediate oscillator strength and located exactly E_{BW} below B (this value is extracted from the PL spectra), and the third level D is formed from the two dark states $D_{1,2}$. The energy position of these dark states E^{BD} is not known and will be determined from the experimental decay curves. The two following arguments are used to justify this simplification. The PL intensities of B_X and B_Y (and that of W_X and W_Y) evolve identically with temperature, indicating that excitonic populations and oscillator strengths for these states are similar. Secondly, the energy splitting between similar levels is small ($\sim 100\,\mu$eV) relatively to kT in the experimental temperature range. Therefore, all intra-levels transfers can be considered equivalent.

Populations in these three levels (n_B, n_W and n_D) evolve with time according to the following balance equations,

$$\begin{aligned}
\frac{\mathrm{d}n_B}{\mathrm{d}t} =& -\left(\gamma^B_{rad} + \gamma_{nr} + \gamma^{BW} + \gamma^{BD}\right) n_B \\
&+ \gamma^{WB} n_W + \gamma^{DB} n_D + \gamma_c n_0 \\
\frac{\mathrm{d}n_W}{\mathrm{d}t} =& -\left(\gamma^W_{rad} + \gamma_{nr} + \gamma^{WB} + \gamma^{WD}\right) n_W \\
&+ \gamma^{BW} n_B + \gamma^{DW} n_D + \gamma_c n_0 \\
\frac{\mathrm{d}n_D}{\mathrm{d}t} =& -\left(\gamma^D_{rad} + \gamma_{nr} + \gamma^{DB} + \gamma^{DW}\right) n_D \\
&+ \gamma^{BD} n_B + \gamma^{WD} n_W + \gamma_c n_0
\end{aligned} \tag{4.1}$$

where n_0 represents the population of photo-generated carrier and γ_c represents the rate at which an IC captures an exciton. γ^B_{rad}, γ^W_{rad} and γ^D_{rad} are the rates of spontaneous emission of the three levels. The rate of thermally activated non-radiative processes γ_{nr} is given by,

$$\gamma_{nr}(T) = \gamma^0_{nr}\left(\frac{1}{\exp\left(E_{nr}/k_B T\right) - 1}\right) \tag{4.2}$$

where γ^0_{nr} is a characteristic rate and E_{nr} is the activation energy, which we will both assume equal for all three levels. The transfer rate from low-energy level i to a high energy level j through spin-flip processes is given by

$$\gamma^{ij}(T) = \gamma^0\left(\frac{1}{\exp\left(E_{ij}/k_B T\right) - 1}\right) \tag{4.3}$$

and the transfer rate for a high-energy level j to a low energy-level i is $\gamma^{ji}(T) = \gamma^{ij}(T) + \gamma^0$. γ^0 is assumed constant for all levels and E_{ij} is the energy separation between levels i and j.

Numerical solutions to this system of differential equations allows calculating the PL decay curves as a function of temperature. The free parameters are γ_{capt}, mainly dependent on the rising edge of the PL, and $\gamma^{B,W,D}_{rad}$, γ^0_{nr}, E_{nr}, γ^0, and the energy splitting between B and D, E_{BD}, mostly dependent on the decay of the PL.

For a given IC configuration, the values for these parameters were determined by *simultaneously* fitting all PL decay curves obtained between 5 and 60 K. Figure 4.3(a) compares the experimental and the numerical PL decay curves for NN_6 (yellow curves) for temperatures located in each of the three regimes discussed earlier. As can be seen, a single set of parameters reproduces all the important characteristics of the decay curves measured at 10, 28 and 60 K and for all other temperatures studied (not shown). The parameters extracted

for NN_6 and all other IC configurations are presented in Table 4.1. Although the number of extracted parameters may appear relatively large, their determination from a fit involving about 10 individual PL decay curves spanning a wide temperature range allowed extracting reliable values. Furthermore, the decay curve proved quite sensitive to each parameters and no other meaningful sets of values could be found, indicating that this approach is robust and accurate.

The long rate of emission, Γ_l, is extracted from calculated curves for each IC configurations studied and presented as the continuous lines in Figure 4.5(b). As can be observed, the temperature variation of the decay rate of NN_6 first presented in Fig. 4.3(b) and that of NN_1, NN_3 and NN_4 are extremely well represented. This excellent agreement indicates that the model proposed and its underlying assumptions capture all important aspects of the carrier dynamics, which is discussed next, as function of the IC configuration.

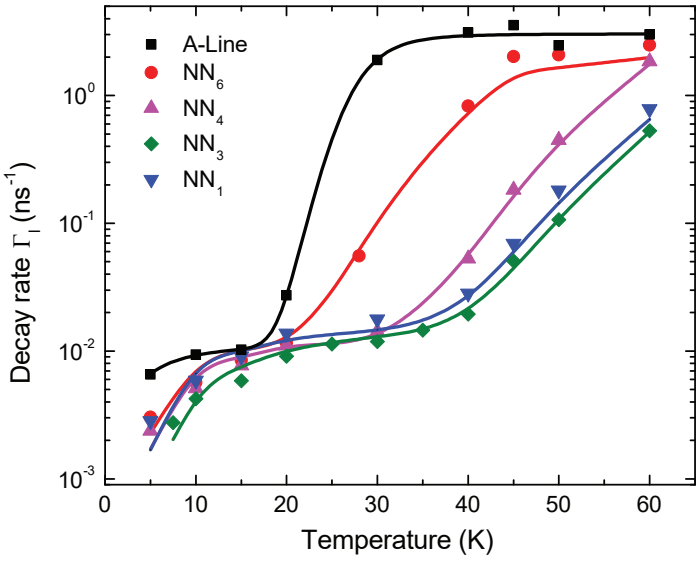

Figure 4.5 Temperature dependence of the emission rate, $\Gamma_l = \tau_l^{-1}$, extraced on the experimental (symbols) and calculated (lines) PL decay curves for all ICs configurations.

ICs	Energy (eV)	γ^B_{rad} (10^7 s^{-1})	γ^W_{rad} (10^6 s^{-1})	γ^D_{rad} (10^4 s^{-1})	γ^0_{nr} (10^{12} s^{-1})	E_{nr} (meV)	γ^0 (10^{10} s^{-1})	E_{BD} (meV)	E_{WD} (meV)
A-Line	2.3171	2.3	–	$\leq$1	0.5	13.9	0.04	0.6	–
NN_6	2.3035	5.3	0.95	$\leq$1	0.33	21.3	0.02	1.2	0.6
NN_4	2.2891	5.0	1.0	$\leq$1	2.8	38.2	2.7	1.4	0.7
NN_3	2.2645	6.1	1.5	$\leq$1	1.9	41.5	6.1	1.5	0.8
NN_1	2.1850	5.8	1.0	$\leq$1	2.5	44.2	1.0	2.1	1.0

Table 4.1 Experimental values describing the exciton dynamics. The capture rate ranged between 400 and 600 ps and did not vary with temperature or IC configuration. For the single-atom configuration, the *weak* states (B-line) was not observed.

4.7 Discussion on the processes governing the dynamics

Table 4.1 reveals that similar values for spontaneous emission rates γ_{rad} were obtained for all IC configurations and that no significant dependence on the interatomic separation can be identified. The spontaneous lifetime is about 18 ns for B states, 0.90 µs for W states and superior to 100 µs for D states. In agreement with previous PL intensity measurements [96], B states have an oscillator strength about an order of magnitude stronger than W states. As expected, the oscillator strength of D states is so small relatively to W and B states that any values0 under $1 \times 10^4\,\mathrm{s}^{-1}$ lead to satisfactory results.

Energy E_{nr} is directly related to the mechanism responsible for the intensity reduction with temperature and its value can be used to identify it. Table 4.1 shows that these activation energies are more than one order of magnitude greater that the energy splitting between levels forming the fine-structure. This confirms our earlier hypothesis that, in first approximation, all the excitonic states of an IC are equally affected by the non-radiative process and that a single parameter (γ_{nr}^0) can be used for all excitonic levels.

For ICs with the lowest interatomic separations and highest binding energies ($NN_{1,3,4}$), activation energies between 38 and 44 meV are obtained. In contrast, the value for NN_6, 21 meV, is significantly lower and is about half that of configurations with larger interatomic separation. This difference in activation energy points to two distinct PL quenching mechanisms[84, 148]. For dyads of low interatomic separations, the binding energy of the localized electron is relatively large and the activation energy measured is associated to the escape of the Coulomb-bound hole[148], with the electron remaining bound to the dyad. For dyads of large interatomic separations and single-atom centers, the activation energy E_{nr} is close to the optical binding energy, indicating that the whole exciton escapes.

Although the escape mechanism for $NN_{1,3}$ has already been identified as hole escape, which is consistent with our findings, no clear identification of the mechanisms associated to shallower centers has been made yet. Ref. [148] and [84] have respectively identified hole escape and exciton escape the mechanisms governing NN_4, and both have tentatively suggested exciton escape for NN_6. Our results clearly indicate that the quenching of NN_4 is dominated by hole escape while that of NN_6 is dominated by exciton escape. From NN_1 to NN_4, the hole binding energy decreases by 6 meV, because, as the dyad interatomic separation increases, the electron localization decreases and so does the strength of the Coulomb interaction between the electron and the hole.

The bright and dark states splitting (E_{bd}) is 0.6 meV for single-nitrogen ICs. As mentioned earlier, this exchange splitting is expected to be larger for dyads and should increase as the

internuclear distance decreases, but it has never been measured before. The data of Table 4.1 reveals that this is indeed the case: the splitting increases from 1.2 meV for NN_6 to 2.1 meV for NN_1. The exchange interaction is inversely proportional to the confinement volume[151]. and since the hole binding energy and potential do not vary significantly for NN_{1-4}, the hole wavefunction is not affected and the magnitude of the splitting can thus be related to the extension of the electron wavefunction. With this analysis, the data clearly indicates that the electron wavefunction are significantly more localized for dyads than for single atom ICs. Finally, this localization increases significantly as the interatomic separation decreases.

As initially assumed from the similar lifetimes for all transitions composing the fine structure of a given IC configuration, inter-level transfer rates dominate spontaneous emission rates. For high (NN_6 and A-line) and low ($NN_{1,3,4}$) interatomic separation configurations, γ^0 exceeds γ^B_{rad} by one and three orders of magnitude, respectively. This indicates that one or more spin-flip mechanisms efficiently randomize excitonic states. These may include hyperfine interaction between the electron and nuclei[152], electron-hole exchange interaction[153], deformation-potential interaction described by the Bir-Pikus Hamiltonian[154], spin-orbit coupling[155], and electrical interaction with neighboring charges[156]. However, it has been demonstrated that spin-flip mediated by phonon-assisted spin-orbit interaction is suppressed in strongly confined quantum dots [157]. Also, transfer rates between dark and bright states in quantum dots, due to the interplay of the exchange interaction and the Bir-Pikus Hamiltonian, were estimated to be very large ($T > 150$ ns)[154, 158], compared to the exciton lifetime. Therefore, it is believed that hyperfine interaction or influence of neighboring charges likely dominate the inter-level transfer of excitons in this system.

In the discussion of the decay rate of NN_6 in regime III, we suggested that dyads are populated through the fast hopping of excitons from single-nitrogen ICs since the decay rate of NN_6 plateaus at a value corresponding to the rise time of the A-line (see Fig.4.3(b)). The calculated decay rates, presented in Fig. 4.5, clearly show this behavior for NN_6. For dyads with a larger binding energy, the activation energy of hopping from single-nitrogen ICs is superior and higher temperatures would be necessary to unambiguously conclude that it is the dominating capture mechanism of excitons.

4.8 Conclusion

In conclusion, we presented an extensive study of the recombination dynamics of excitons bound to nitrogen isoelectronic centers in GaP formed by single-atom and two-atom isoelectronic centers. For all ICs studied, the temperature dependence of the decay times clearly exhibits three different regimes where the dynamics is dominated by : 1) thermally activated

transfer between the different excitonic states forming the fine structure at low temperatures, 2) thermally activated non-radiative channel of emission at intermediate temperatures, and 3) a fast hopping from the single-atom configuration to dyads at high temperatures. By fitting the data with PL decay curves calculated with a balance of populations model we were able to extract the fundamental parameters governing these three regimes : the time of capture of excitons, the rate of spontaneous emission of all excitonic states forming the fine structure, the dark and bright states splitting, the activation energies of non-radiative processes. Most of these parameters were calculated for the first time and the precise values of the activation energies of the non-radiative processes allowed a clarification of their nature which is the escape of the hole for $NN_{1,3,4}$ and the transfer to a free excitonic state for NN_6 and the A-line.

These findings suggest that nitrogen ICs are interesting candidates for classical single-electron memories of atomic dimensions. Since the hole binding energy is significantly less than that of the electron for $NN_{1,3,4}$, a relatively weak electric field could be applied to break the exciton and expel the hole, leaving the electron in a long-lived metastable state until a hole is brought back to induce excitonic emission. On the other hand, the fast spin-flip mechanisms observed represent an obstacle for the realization of exciton qubits. However, as the nature of these mechanisms is not yet understood, it remains to be determined if their effect could be mitigated, as it has been demonstrated for example for the hyperfine interaction in quantum dots [159]. Interestingly, inter-level transfers do not play a similar role for nitrogen ICs in GaAs, indicating that different impurity-host combinations present remarkably different sets of characteristics. Other IC systems of interest that would likely provide advantageous coherence times include hole traps like Te dyads in ZnSe and electron-traps like Be dyads in isotopically purified Si.

CHAPTER 5 ARTICLE 2 - DYNAMICS OF EXCITONS BOUND TO NITROGEN ISOELECTRONIC CENTERS IN GAAS

Authors:

Philippe St-Jean, Gabriel Éthier-Majcher, and Sébastien Francoeur

This work was published in *Physical Review B*, volume **91**, pp. 115201 (1-11), (2015)

5.1 Abstract

A detailed analysis of the dynamic of excitons bound to two nitrogen atoms forming an isoelectronic center of C_{2v} symmetry in GaAs is presented. The temperature dependence of photoluminescence (PL) intensities under both continuous and pulsed excitations reveals 1) overall decay rates significantly slower than that of spontaneous emission, 2) a decay rate anisotropy between states of orthogonal symmetry representations, and 3) a complementary behavior of relative intensities measured from states of identical symmetry representations. A comprehensive model of the exciton fine structure and the exciton dynamics allows the determination of the strength of the exchange and crystal-field interactions, the light- and heavy-hole splitting and composition of exciton states, the exciton capture time, the rates of spontaneous and non-radiative emission, and the rates of inter-level transfers induced by interactions with nuclear spins and by longitudinal acoustic phonons. It is found that the rate of electron spin-flips is comparable to that measured in quantum dots, but that the near degeneracy of light- and heavy-holes results in an efficient transfer channel between light-and heavy-holes states of identical symmetry representation.

5.2 Introduction

The ability to write, manipulate and read out quantum states is a fundamental requirement for quantum information processing and, over the last decade, several promising optically-addressed systems for qubits storage and operations have been identified and studied. Seminal demonstrations were realized using electrostatic and epitaxial quantum dots[58, 160], nitrogen-vacancy centers and other defects in diamond[143, 161], and phosphorous donors in isotopically purified silicon[139, 146]. Each of these systems provides a unique set of advantageous characteristics, but also faces a number of challenges, making the evaluation of their long-term prospects for quantum information applications difficult. It is therefore not surprising that the search for other material systems is ongoing. In fact, the choice is wide and

remains largely unexplored. This is particularly true for bound states created by impurities or other point defects in crystalline hosts[67, 71, 162, 163]. Recently, we have demonstrated that charges trapped on isoelectronic centers (ICs) in semiconductors are promising candidates, as they combine two fundamentally advantageous characteristics not commonly found together: the optical homogeneity of atomic defects and the high dipole moment of semiconductor quantum dots[74].

ICs are atomic defects built from one, two, or a small number of impurities forming an isovalent center. Through a deformation of the lattice and a disruption of the electronic charge density of the host material, this center can either trap an itinerant electron or hole, depending on the nature of the impurities. This primary charge can then trap via Coulomb interaction a secondary charge of opposite sign to form an exciton. These defects were first studied several decades ago, but the ability to individually address and optically control them has only been demonstrated recently[104]. Although a number of isoelectronic impurities have been identified for many semiconductor materials, pairs of nitrogen atoms (dyads) in GaAs[104], GaP[100] and AlAs [93], and of Te atoms in ZnSe[117] are the most studied impurity/host systems to date. The physics of ICs is reminiscent of quantum dots, since conduction and valence band states remain valid for describing bound electrons and holes states. IC characteristics can be tuned by varying the composition (number or type of impurities), configuration (interatomic separation and symmetry), and orientation within the host lattice. They can be addressed both electrically or optically. Furthermore, ICs can bind single charges, excitons, biexcitons and charged excitons[108], a technological advantage observed for only very few atomic-size defects[164]. However, in contrast to other optically controlled qubits, their intrinsically low inhomogeneous broadening, high photo-stability, and high electric dipole moments may be strategically advantageous for scaling up quantum information applications with minimal implementation complexity.

To determine their potential as building blocks for quantum information, it is critical to establish a better understanding of IC characteristics (charge trapping mechanisms, exciton fine structure, energy levels associated with various configurations,...) and of the behavior of bound charges. In this work, we reveal several fundamental aspects related to exciton states bound to N dyads in GaAs and their spin dynamics, from the exciton capture rate to interlevel transfer rates. The scope of the experimental data and the depth of the present analysis exceeds everything that has previously been done on Te dyads in ZnSe[117] and N dyads in GaAs[106] and GaP[165]. Furthermore, in contrast with many previous work on semiconductor nanostructures[133], this analysis rigorously take into account the reduced symmetry of the system (C_{2v}) and the considerable light- and heavy-hole mixing of exciton states. It therefore allows for a richer and more complete understanding of the various

mechanisms governing the exciton dynamics.

The paper is organized as follows. Section II briefly describes the sample structure and experimental methods used. Section III presents experimental results. It includes the exciton fine structure and the temperature dependence of time-resolved PL curves and of PL intensities. Section IV presents a comprehensive model used to simulate the exciton dynamics and reproduce the experimental data of Section III. Section V demonstrates that this model satisfactorily accounts for all experimental observations and presents an insightful discussion on the important mechanisms governing the exciton dynamics. Finally, Section VI briefly summarizes our findings.

5.3 Samples and methods

A single GaAs:N layer of 25 nm was grown between two 5 nm layers of undoped GaAs(001), and inserted between two $Al_{0.25}Ga_{0.75}As$ barriers. The concentration of the nitrogen doped layer is such that the dyad surface density is 1 μm^{-2} allowing to spatially resolve single dyads using a diffraction-limited confocal microscope with a resolution of 0.8 μm at 820 nm.

The known nitrogen dyad configurations that emit in the band gap of GaAs exhibit C_{2v} symmetry[104] and have been assigned to two substitutional nitrogen atoms positioned in first and fourth nearest-neighbor sites on the anionic sublattice[86]. In this work, we present emission characteristics of the nitrogen dyad emitting at 1.508 eV, which has been attributed to the first nearest-anionic neighbor configuration, NN_1.

Micro-photoluminescence measurements were performed on single dyads at temperatures ranging from 5 to 12 K. Excitation was either provided by a 1 ps mode-locked Ti:sapphire laser operating at 800 nm with a repetition rate of 80 MHz or a CW 780 nm laser. The photoluminescence signal was analyzed using a spectrometer and an avalanche photodiode providing a spectral resolution of 60 μeV and a temporal resolution of less than 100 ps. A motorized $\lambda/2$ wave plate and a polarizer were used to analyze the polarization of the emission.

5.4 Experimental results

5.4.1 Fine structure of the emission

Figure 5.1 (d) and 5.1 (e) show the photoluminescence intensity from a single nitrogen dyad as a function of energy and linear polarization angle. The fine structure of the excitonic emission arises from the combined effects of confinement, electron-hole exchange interaction,

and crystal-field interaction. Although similar to what is usually observed from conventional quantum dots, the quasi-degeneracy of heavy- and light-hole states results in a richer fine structure involving twice the number of excitonic states. The specifics of the emission fine structure and polarization can be used to unambiguously identify the symmetry of the dyad[91], as was done for N in GaP[100] and GaAs[104], and for Te dyads in ZnSe[117]. The four transitions presented in Fig. 5.1 clearly identify a dyad with a C_{2v} symmetry.

Under C_{2v} symmetry, the degeneracy between the eight excitonic states formed by the $J = 2$ quintuplet and the $J = 1$ triplet is completely lifted[91, 108]. Mixing of these states gives rise to two dark states ($D_{1,2}$) not coupled to the electromagnetic field and six bright states exhibiting linearly polarized emission: two polarized along the dyad ($X_{1,2}$), two polarized perpendicular to the dyad and the C_2 axis ($Y_{1,2}$), and two polarized along the C_2 axis ($Z_{1,2}$).

Transitions in the spectra of Fig. 5.1 are labeled according to the orientation of their polarization (X, Y, Z) and to their relative energy (1 and 2 for the low- and high-energy manifold, respectively). The absence of $Z_{1,2}$ transitions in the spectra shown in Fig. 5.1 (d) and 5.1 (e) indicate that this particular center is formed from two nitrogen atoms located in the plane of the sample and oriented along $\langle 110 \rangle$. Transition Z_2 is only observed from out-of-plane dyads for which a PL spectrum is presented in Fig. 5.1 (c) in order to complete the set of optical transitions observed from this isoelectronic center configuration[90].

5.4.2 Luminescence decay time anisotropies

Time-resolved photoluminescence (TRPL) was performed on X_1, X_2, Y_1, and Y_2 at temperatures of 5, 6.5, 8, 10 and 12 K. Above 12 K, the photoluminescence intensity abruptly vanishes. Figure 5.2 presents a representative subset of the data used in this work to analyze the exciton dynamics: Panel (a) shows the TRPL curves of the four allowed transitions at 8 K, and Panel (b) shows the TRPL curves of Y_1 at all temperature studied. As can be seen from the two panels, all curves are very well represented by a the sum of one rising and one decaying mono-exponentials (red curves). It was also the case for the 12 other PL decay curves.

The rise time of the photoluminescence varies between 250 ps and 500 ps and does not exhibit a dependence on temperature or on the excitonic state involved, indicating that the exciton or charge carrier capture process does not sensitively depend on these two aspects for the temperature range studied. In contrast, the decay time of the luminescence significantly depends on both. As indicated on Fig. 5.2 (a), at 8 K, the decay time of X_1 and X_2 are respectively 5.8 and 5.7 ns and those of Y_1 and Y_2 are respectively 4.3 and 4.6 ns. Interestingly, decay times of states involving identical polarizations are quite similar, but

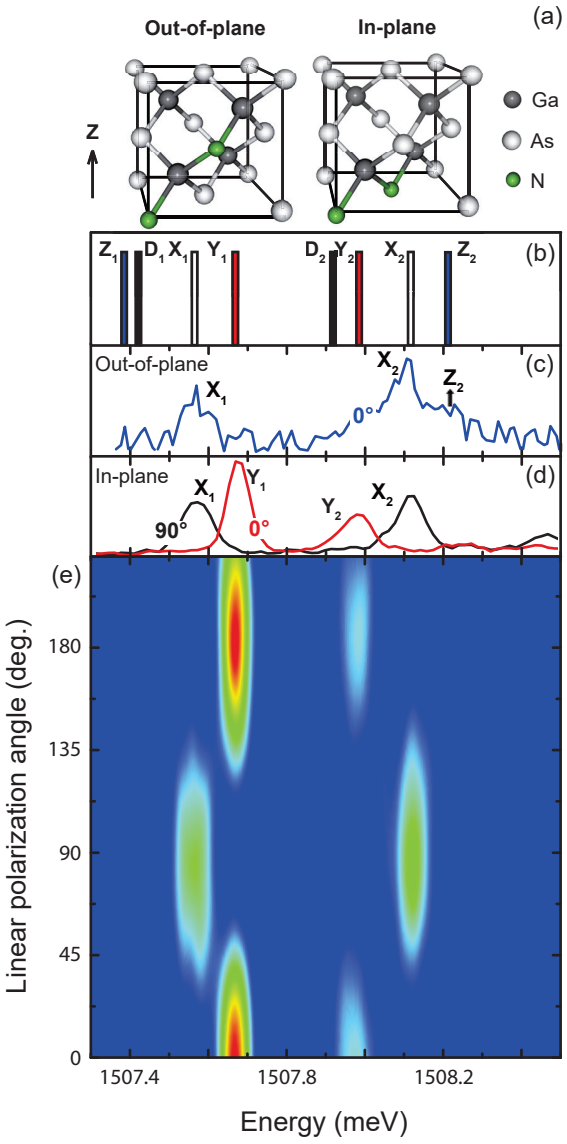

Figure 5.1 (a) In-plane and out-of-plane configurations for dyads of C_{2v} symmetry. (b) Calculated spectral position of all excitonic states of a nitrogen dyad oriented along $\langle 110 \rangle$. (c) Photoluminescence intensity polarized parallel to an out-of-plane nitrogen dyad of C_{2v} symmetry. (d) Photoluminescence intensity polarized perpendicular (0°, red curve) and parallel (90°, black curve) to the in-plane nitrogen dyad studied in this work. (e) Photoluminescence intensity map as a function of energy and linear polarization of the emission.

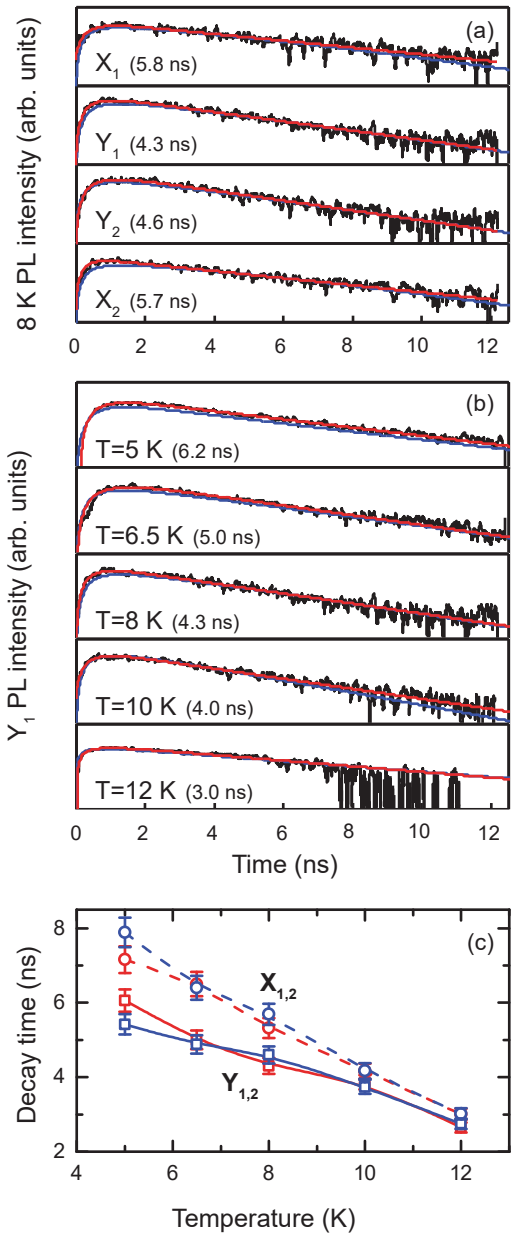

Figure 5.2 Time-resolved PL from the single nitrogen dyad presented in Fig. 5.1. Panel (a) shows all four excitonic transitions at $T = 8\ K$ and (b) shows transition Y_1 at all temperatures studied. For both panels, the red curves show the sum of one rising and decaying mono-exponentials that best fitted the data; decay times are indicated. Blue curves show the PL intensities calculated from the model presented in Section 5.5. (c) Temperature evolution of extracted decay times. Y_1 and Y_2 (X_1 and X_2) are represented by the red and blue squares (circles). Dashed (X_i) and solid (Y_i) lines are added to guide the eye.

they strongly differ for states involving orthogonal polarizations. This decay time *anisotropy* is very well illustrated in Panel (c) of Fig. 5.2, as it is observed at all temperatures, although most significantly at low temperatures.

In addition to this anisotropy, we note that the measured PL decay times are about 10 times slower than the anticipated spontaneous emission lifetimes. Determined from resonantly driven Rabi oscillations, dipole moments reveal radiative lifetimes on the order of 500 ps.[74]

5.4.3 Revealing symmetries in photoluminescence intensities

Relative luminescence intensities as a function of temperature exhibit surprisingly rich information also pertaining to the exciton dynamics. Panel (a) of Fig. 5.3 presents the relative intensity of the four transitions and Panel (b) shows the evolution of the total intensity. Relative intensities show distinctive behaviors depending on both the transition energy and polarization. Intensities of $X_{1,2}$ are almost equal at 5 K, but the higher-energy X_2 strongly dominates the lower-energy X_1 at higher temperatures. In contrast, transitions $Y_{1,2}$ show dissimilar intensities at 5 K, but their intensities converge at higher temperatures. At all temperatures, the sum of the intensity of X_1 and X_2 and of Y_1 and Y_2 make up 50% of the total intensity.

5.4.4 Quenching of the photoluminescence total intensity

Figure 5.3(b) shows an Arrhenius plot of the total intensity measured from the four allowed transitions as a function of temperature. A rapid intensity drop of more than 3 orders of magnitude is observed as temperature is raised from 5 to 12 K. It is due to thermally activated non-radiative processes quenching the radiative emission. Finally, all experimental results presented in this section are representative of those measured on other nitrogen dyads emitting at 1.508 eV.

5.5 Exciton dynamics model

Identical decay times for similarly polarized transitions together with striking symmetries in photoluminescence intensities suggests that efficient $X_1 \leftrightarrow X_2$ and $Y_1 \leftrightarrow Y_2$ transfers occur before radiative emission. Furthermore, the X and Y decay time anisotropy along with the fact that all decay times measured significantly exceed spontaneous emission lifetimes suggest that recombination dynamics is also influenced by a second inter-level transfer mechanism connecting bright and dark states together. Although valuables clues can be directly extracted from the data, a comprehensive understanding of the exciton dynamics

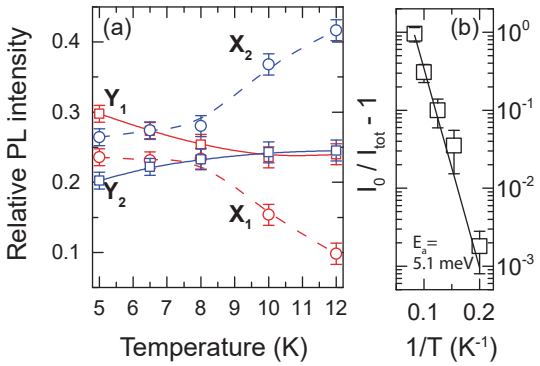

Figure 5.3 (a) Temperature dependence of the relative PL intensity of the four allowed excitonic transitions. Y_1 and Y_2 (X_1 and X_2) are represented by the red and blue squares (circles). Dashed (X_i) and solid (Y_i) lines are added to guide the eye. (b) Arrhenius plot of the total PL intensity measured from all four transitions shown in Fig. 5.1. The solid curve shows the calculated intensity of a thermally activated process.

requires a quantitative model. In this section, we present the model used to analyze the time and temperature dependence of the PL, extract information on the angular component of exciton wave-functions, reproduce exciton transition energies and determine radiative and non-radiative rates along with inter-level transfer rates.

Fig. 5.4 presents the structure of the model and the parameters (shown inside gray boxes) required to numerically reproduce the experimental data (labeled in red). This model is divided in three parts. Part I calculates exciton energies and wave-functions from an Hamiltonian that takes into account the exchange and the crystal field interactions, and light- and heavy hole confinement effects. A rigorous treatment of C_{2v} symmetry requires six parameters. Part II uses these wave-functions to calculate transfer rates associated to spontaneous emission and non-radiative emission, and inter-level transfer rates induced by the hyperfine interaction and by acoustic phonons. The relative influence of these four mechanisms is modulated by five parameters: $\Gamma_0^{(\mathrm{rad})}$, $\Gamma_0^{(\mathrm{nr})}$,$W_0^{(\mathrm{hf})}$, $\Gamma_0^{(\mathrm{ap})}$, and the energy barrier E_f associated to the non-radiative process. Except for spontaneous emission, exciton transfers are thermally activated and sensitively depend on temperature. Finally, part III dynamically calculates exciton populations and PL intensities using a 9-level population balance model. It exploits the transfer rates calculated in part II with the addition of a parameter describing the exciton capture rate ($\Gamma^{(\mathrm{capt})}$). Here, we present a detailed description of these three parts.

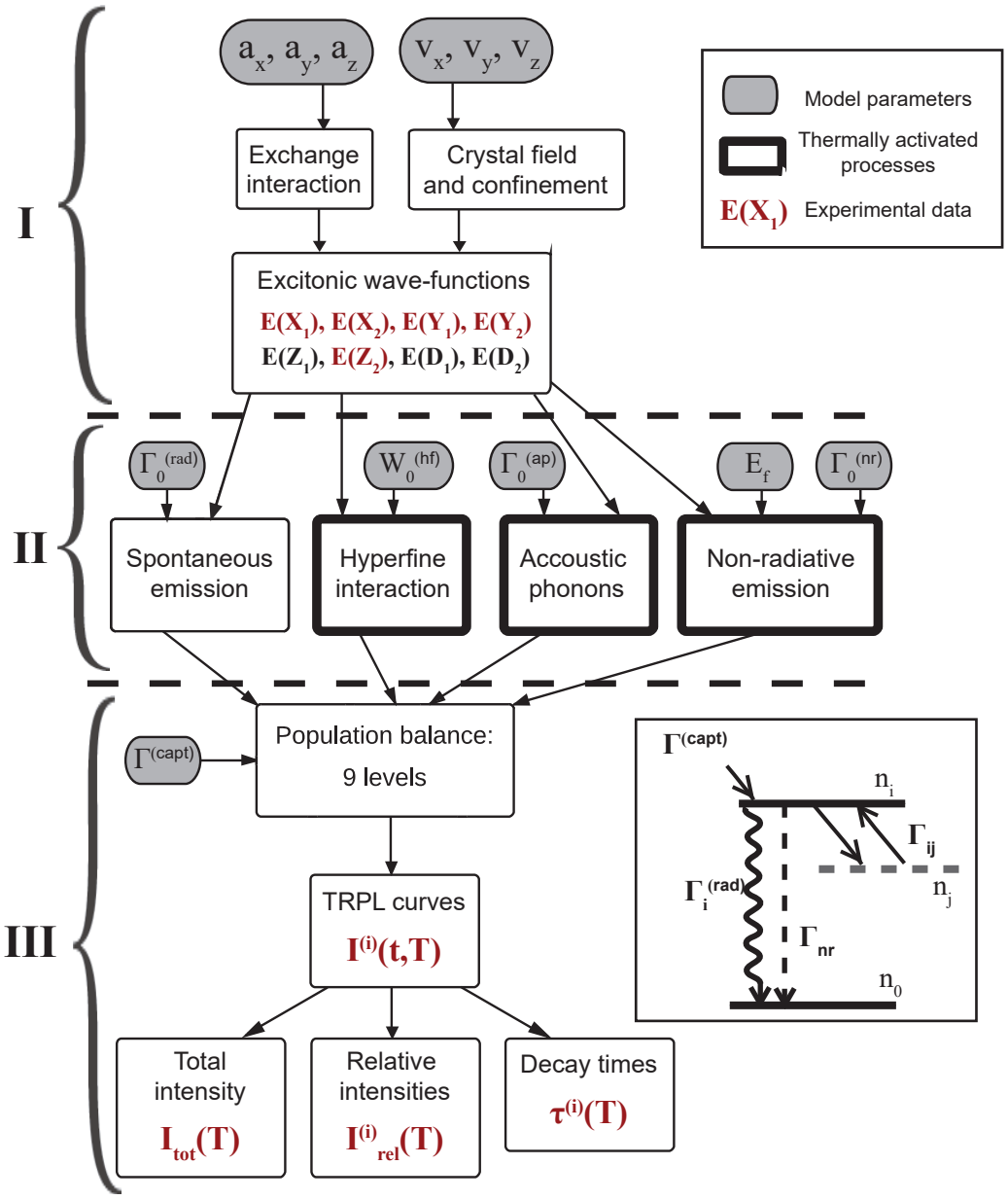

Figure 5.4 Schematic representation of the model used to calculate excitonic energies and wavefunctions, time-resolved luminescence curves, and luminescence intensities. Quantities in gray boxes are adjustable parameters and quantities labeled in red are those directly compared to the experimental data. Boxes with thicker contour indicate temperature dependent transfer mechanisms. Inset: Population balance model for excitonic state i involving the ground state 0 and the seven other excitonic states for which $i \neq j$.

5.5.1 Part I - Excitonic wavefunctions

The perturbation Hamiltonian lifting the degeneracy between the eight states of the bound exciton takes into account three effects: the electron-hole exchange interaction, the crystal-field perturbation produced by the dyad on the crystal, and the confinement effects experienced by light- and heavy-holes.

Under C_{2v} symmetry, the three principal axes are inequivalent and the Hamiltonian is,

$$H = -\sum_{i=x,y,z} a_i J_i S_i + \sum_{i=x,y,z} v_i J_i^2, \tag{5.1}$$

where **J** and **S** represent the total angular momentum of the hole and the electron spin. The first term in the Hamiltonian corresponds to the exchange interaction, where $a_{x,y,z}$ are the non-degenerate exchange parameters. Similarly, the crystal-field Hamiltonian is composed of three coefficients, $v_{x,y,z}$. The diagonal part of this Hamiltonian is isomorphic to the effect of confinement on light- and heavy-hole bands, such that these coefficients also take into account effects of confinement on the exciton fine structure. More details about the development of this Hamiltonian can be found in Ref. [91].

The remote spin-orbit split-off valence states are ignored and this hamiltonian is expanded in a basis of eight excitonic states built from two electron states ($\alpha_e = |1/2, 1/2\rangle$, $\beta_e = |1/2, -1/2\rangle$) and 4 hole states ($\phi_1 = |3/2, 3/2\rangle$, $\phi_2 = |3/2, 1/2\rangle$, $\phi_3 = |3/2, -1/2\rangle$ and $\phi_4 = |3/2, -3/2\rangle$). Symmetry-adapted exciton wavefunctions are presented in Table 5.1 and Figure 5.5 along with their representations and dipole moments. ψ_{1-4} and ψ_{5-8} are respectively built from light- and heavy-hole states and superscripts (x, y, x or d) either indicate the polarization orientation or a dark state not interacting with the radiation through the usual dipolar term.

Exciton energies and wavefunctions are obtained by diagonalizing Eq. 5.1. Mixing between light- and heavy-holes states of identical representations generates eight coupled wavefunctions Ψ_i. This approach has already been used to analyze the excitonic fine structure of in-plane[166] and out-of-plane nitrogen dyads[90].

5.5.2 Part II - Exciton transfer mechanisms

Exciton energies and wavefunctions are then used to calculate transfer rates associated with spontaneous emission to the ground states, non-radiative processes, and inter-level transfers.

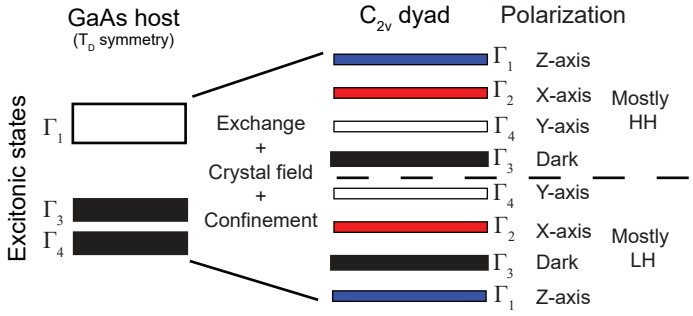

Figure 5.5 Schematic diagrams of energy levels for a free exciton in a GaAs crystal and for an exciton bound to a nitrogen dyad of C_{2v} symmetry. The ordering of the levels is obtained from Eq. 5.1 and the PL data.

Spontaneous emission and non-radiative processes

The rate of spontaneous emission from excitonic state $|\Psi_i\rangle$ to the ground state $|0\rangle$ is calculated using

$$\Gamma_i^{(\mathrm{rad})} = \Gamma_0^{(\mathrm{rad})} |\langle \Psi_i | \hat{r} | 0 \rangle|^2. \tag{5.2}$$

where $\hat{r}$ is a vector of unit length. In this expression, the radial part of atomic and envelope wave-functions were decoupled from angular and spin coordinates and were absorbed into $\Gamma_0^{(\mathrm{rad})}$, which is to be determined experimentally. The angular part $\langle \Psi_i | \hat{r} | 0 \rangle$ is explicitly integrated to obtain the relative dipole moment of excitonic transition i.

As shown in Fig. 5.3(b), the total PL intensity is strongly influenced by temperature, indicating the presence of thermally activated non-radiative processes. Assuming the presence of an external state f positioned at energy E_f, the non-radiative rate for state i is

$$\Gamma_i^{(\mathrm{nr})} = \frac{\Gamma_0^{(\mathrm{nr})}}{\exp\left(\Delta E_i / k_B T\right) - 1}, \tag{5.3}$$

where $\Delta E_i = E_f - E_i$ is the activation energy associated to the transfer from i to state f. $\Gamma_0^{(\mathrm{nr})}$ is a constant describing the strength of phonon-exciton interactions enabling non-radiative processes. It does not depend on the exciton state and it is determined experimentally.

Wavefunction	Representation	$\langle\psi_i\vert\,\hat{r}\,\vert 0\rangle$
$\psi_1^{(z)} = \frac{1}{\sqrt{2}}(-\beta_e\phi_4 + \alpha_e\phi_1)$	Γ_1	$(0,0,0)$
$\psi_2^{(x)} = \frac{1}{\sqrt{2}}(\beta_e\phi_1 + \alpha_e\phi_4)$	Γ_2	$(\frac{1}{\sqrt{2}},0,0)$
$\psi_3^{(d)} = \frac{i}{\sqrt{2}}(\beta_e\phi_4 + \alpha_e\phi_1)$	Γ_3	$(0,0,0)$
$\psi_4^{(y)} = \frac{i}{\sqrt{2}}(-\beta_e\phi_1 + \alpha_e\phi_4)$	Γ_4	$(0,\frac{1}{\sqrt{2}},0)$
$\psi_5^{(z)} = \frac{1}{\sqrt{2}}(-\beta_e\phi_2 + \alpha_e\phi_3)$	Γ_1	$(0,0,\frac{2}{\sqrt{3}})$
$\psi_6^{(x)} = \frac{1}{\sqrt{2}}(\beta_e\phi_3 + \alpha_e\phi_2)$	Γ_2	$(\frac{-1}{\sqrt{6}},0,0)$
$\psi_7^{(d)} = \frac{i}{\sqrt{2}}(\beta_e\phi_2 + \alpha_e\phi_3)$	Γ_3	$(0,0,0)$
$\psi_8^{(y)} = \frac{i}{\sqrt{2}}(-\beta_e\phi_3 + \alpha_e\phi_2)$	Γ_4	$(0,\frac{1}{\sqrt{6}},0)$

Table 5.1 Symmetry-adapted exciton wavefunctions, C_{2v} representations and dipole moments (expressed in units of ($\langle s|x|x\rangle$, $\langle s|y|y\rangle$, $\langle s|z|z\rangle$)). ψ_{1-4} and ψ_{5-8} are built from heavy- and light-hole states, respectively.

Inter-level transfers mechanism

Inter-level transfers between excitonic states involve processes flipping the spin of the electron or hole, or both. The most relevant spin-flip mechanisms for isoelectronic centers are discussed below.

Spin-orbit induced transfers The spin relaxation of electrons ($\sim$ 100 ps) and holes ($\sim$ 100 fs) in bulk semiconductors is dominated by spin-orbit interaction[167, 168]. In quantum dots, much longer relaxation times are experimentally found at low temperatures, revealing that carrier localization strongly quenches spin-orbit related mechanisms[140, 169–173]. Indeed, theoretical calculations estimate that spin-orbit interaction leads to electron and hole spin relaxation times exceeding 1 μs in strongly confined quantum dots ($\leq$ 10 nm)[157, 174, 175]. Although the localization of electrons bound to ICs like N dyads in GaAs is not accurately known, two important aspects indicate a strong localization: the rapid variation of the exciton binding energy with the separation between the two nitrogen atoms[102] and the very small diamagnetic[176] shift (1.27 μeV T^{-2}) associated to the bound electron[166]. Furthermore, empirical pseudopotential calculations suggest that the electron wavefunction is concentrated within the volume of a few unit cells[86]. Spin-orbit related processes are thus expected to be of secondary importance.

Hyperfine induced transfers The dominant electron spin relaxation mechanism in semiconductor quantum dots is the simultaneous spin-flip of an electron and a nucleus induced by the hyperfine interaction.[137, 177] The calculation of transfer rates between non-degenerated excitonic states requires second-order perturbation theory, because the energy involved in

the spin flip of a nuclear spin does not match the exciton energy splitting[178, 179] and a phonon interaction is necessary to fulfill energy conservation. Analytical models reveal that the rates are inversely proportional to N, the number of nuclei under the electron wavefunction. Therefore, in comparison with quantum dots where $N \sim 10^5$, the strong localization of the electron mentioned above could lead to very efficient hyperfine induced exciton transfers.

The calculation of transfer rates starts from the Hamiltonian describing the hyperfine contact interaction between a bound electron and nearby lattice nuclei,

$$\begin{aligned} H^{(\mathrm{hf})} =& \sum_k A_k \vec{S} \cdot \vec{I}_k \\ =& \sum_k A_k \left(\frac{1}{2} \left(S_+ I_{-,k} + S_- I_{+,k} \right) + S_z I_{z,k} \right), \end{aligned} \tag{5.4}$$

where the summation runs over all nuclei sites. $A_k = A_{0,k}\nu_0 |\Psi(\vec{r}_k)|^2$, where $A_{0,k}$ are the hyperfine constants, ν_0 is the primitive cell volume and $|\Psi(\vec{r}_k)|^2$ is the electron density at site k. $\vec{S}$ and $\vec{I}_k$ are the electron and nucleus spin operators, and $S_\pm$ and $I_\pm$ are the usual ladder operators. Since they have been shown to be less efficient, spin-flips involving holes and nuclei are neglected.[134, 180]

The first two terms of Eq. 5.4 lead to electron-nucleus spin flips. The nuclear spin-flip energy ($\hbar\omega_n$) is negligible compared to the energy difference between exciton states and inter-level transfers must be assisted by phonon emission or absorption ($\hbar\omega_{\vec{q}}$). The transfer rate is therefore determined by both the hyperfine $H^{(\mathrm{hf})}$ and exciton-phonon $H^{(\mathrm{ph})}$ interactions. Using second-order perturbation and Fermi's golden rule, the transfer rate from $|\Psi_i\rangle$ to $|\Psi_j\rangle$ is

$$\Gamma_{ij}^{(\mathrm{hf})} = \Gamma_0^{(\mathrm{ph})} \sum_{\mu,\mu'} P(\mu) \left| \frac{\langle \Psi_v, \mu' | \, H^{(\mathrm{hf})} \, | \Psi_i, \mu \rangle}{E_{ij}} \right|^2, \tag{5.5}$$

where

$$\begin{aligned} \Gamma_0^{(\mathrm{ph})} =& \frac{2\pi}{\hbar} \left| \langle \Psi_j | \, H^{(\mathrm{ph})} \, | \Psi_v \rangle \right|^2 \delta\left(E_i - E_j\right) \\ & \cdot \begin{cases} N_B(E_{ij}) & \text{if } E_j > E_i \\ N_B(E_{ij}) + 1 & \text{otherwise} \end{cases} \end{aligned} \tag{5.6}$$

is the phonon-exciton scattering rate, $N_B(E_{ij})$ is the phonon occupation probability given by the Bose-Einstein statistic, $|\Psi_v\rangle$ is a virtual state with angular component similar to that of Ψ_j, and $E_{ij} = |E_j - E_i|$. $E_j > E_i$ corresponds to phonon absorption and $E_j < E_i$ to phonon emission. μ and μ' refer to the initial and final nuclear spin states and $P(\vec{\mu})$ is their occurence probability. In the absence of nuclear polarization, $P(\mu)$ is the same for all possible values of μ. Equation 5.5 is simplified by collecting into a single parameter, $W_0^{(\mathrm{hf})}$, all quantities independent of the excitonic states involved. This includes normalization constants arising from the radial and envelope parts of wave-functions, hyperfine constants A_k, and physical constants. In addition, the phonon-exciton interaction is assumed to be identical for all states j, such that the influence of $\langle\Psi_j| H^{(\mathrm{ph})} |\Psi_v\rangle$ is also collected in $W_0^{(\mathrm{hf})}$. The hyperfine transfer rate is thus given by,

$$\begin{aligned}\Gamma_{ij}^{(\mathrm{hf})} =& W_0^{(\mathrm{hf})} \sum_{\vec{\mu},\vec{\mu'}} P(\vec{\mu}) \left| \frac{\langle\Psi_j, \vec{\mu'}| \left(S_+ I_- + S_- I_+\right) |\Psi_i, \vec{\mu}\rangle}{E_{ij}} \right|^2 \\ & \cdot \begin{cases} N_b(E_{ij}) & \text{if } E_j > E_i \\ N_b(E_{ij}) + 1 & \text{otherwise} \end{cases} \end{aligned} \tag{5.7}$$

Matrix elements are evaluated using wave-functions $|\Psi_i\rangle$ and, as expected, non vanishing transfer rates occur between dark or Z-polarized states and X- or Y- polarized states. The value for $W_0^{(\mathrm{hf})}$ is determined by fitting the model to the experimental data.

Acoustic phonons induced transfers For epitaxial quantum dots, valence band degeneracy is lifted by confinement and external strains, leading to negligible exciton transfers between light- and heavy-hole manifolds[154]. For isoelectronic centers, the Hamiltonian presented in Eq. 5.1 couples nearly degenerate light- and heavy-hole excitonic states and, as a result, new processes can significantly influence the exciton dynamics.

Through their deformation of the lattice, phonons creates a momentary perturbation providing the impulse and energy needed for inter-level exciton transfers. These exciton-phonon interactions arise principally through the piezoelectric and deformation potential couplings generated by acoustic phonons, but, for exciton states, piezoelectric coupling is relatively unimportant because the electron and hole wavefunction overlap reduces polar interactions[181, 182]. Deformation potential coupling is treated using the Bir-Pikus strain Hamiltonian which, for a system of C_{2v} symmetry, is

$$
\begin{aligned}
H^{(\mathrm{dp})} =& 4 \sum_{i=x,y,z} \left(d_{xi} J_x^2 + d_{yi} J_y^2 + d_{zi} J_z^2 \right) \langle \epsilon_{ii} \rangle \\
&+ \frac{2}{\sqrt{3}} \left(e_{xz} \{ J_x, J_z \} \langle \epsilon_{xz} \rangle + e_{yz} \{ J_y, J_z \} \langle \epsilon_{yz} \rangle + e_{xy} \{ J_x, J_y \} \langle \epsilon_{xy} \rangle \right),
\end{aligned}
\tag{5.8}
$$

where the notation $\{J_i, J_z\}$ denotes an anticommutator, d_{ij} and e_{if} are deformation potentials, and $\langle \epsilon_{ij} \rangle$ are phonon-induced strains averaged over the hole wavefunction. This Hamiltonian couples any given heavy-hole (light-hole) state with its light-hole (heavy-hole) counterpart of identical representation through longitudinal strain elements (ϵ_{ii}) and with the three remaining light-hole (heavy-hole) states through shear strain elements (ϵ_{ij}, $i \neq j$). Simplifications are necessary to reduce the complexity of this Hamiltonian to a tractable level. First, it has been demonstrated that deformation potential coupling is dominated by LA phonons[183, 184], as long wavelength TA phonons are akin to lattice translations at the scale of a localized exciton. Thus, coupling induced by TA phonons through shear components are neglected by setting $d_{ij} = 0$ for $i \neq j$. This assumption implies that transfers can now only occur between light- and heavy-hole states of similar symmetry representations. The next simplification consists in assuming that deformation potentials are simply proportional to the crystal-field parameters solutions of Eq. 5.1, $d_{ii} = dv_i$. These simplifications lead to,

$$
H^{(\mathrm{df})} = 4d \left(v_x J_x^2 + v_y J_y^2 + v_z J_z^2 \right) \left(\langle \epsilon_{xx} \rangle + \langle \epsilon_{yy} \rangle + \langle \epsilon_{zz} \rangle \right)
\tag{5.9}
$$

By combining d, strain components and all other constants into a single parameter $\Gamma^{(\mathrm{ap})}$, the transfer rate from $|\Psi_i\rangle$ to $|\Psi_j\rangle$ induced by LA phonons is then

$$
\begin{aligned}
\Gamma_{ij}^{(\mathrm{ap})} =& \Gamma_0^{(\mathrm{ap})} |\langle \Psi_i | H^{(dp)} | \Psi_j \rangle|^2 \\
&\cdot \begin{cases} N_B(E_{ij}) & \text{if } E_j > E_i \\ N_B(E_{ij}) + 1 & \text{otherwise.} \end{cases}
\end{aligned}
\tag{5.10}
$$

As will be seen, this light- and heavy-hole coupling explains the efficient population transfer between bright states of identical polarizations.

5.5.3 Part III - Population balance model

The time evolution of the population of all eight excitonic states can be obtained by solving 9 coupled differential equations. The population balance model schematically represented in the inset of Fig. 5.4 leads to eight equations of the form,

$$\frac{\mathrm{d}n_i}{\mathrm{d}t} = -\Big(\Gamma_i^{(\mathrm{rad})} + \Gamma_i^{(\mathrm{nr})} + \sum_{j\neq i}\Big(\Gamma_{ij}^{(\mathrm{hf})} + \Gamma_{ij}^{(\mathrm{ap})}\Big)\Big)n_i + \sum_{j\neq i}\Big(\Gamma_{ji}^{(\mathrm{hf})} + \Gamma_{ji}^{(\mathrm{ap})}\Big)n_j + \Gamma^{(\mathrm{capt})}n_0, \tag{5.11}$$

and,

$$\frac{\mathrm{d}n_0}{\mathrm{d}t} = -\Big(\sum_i \Gamma^{(\mathrm{capt})}\Big)n_0, \tag{5.12}$$

where n_i is the population of state i ($i = 1-8$) and n_0 is the exciton reservoir population. Index j runs over the indices of all other states for which $j \neq i$. $\Gamma^{(\mathrm{capt})}$ is the exciton capture rate, which is in this model identical for all states and independent of temperature. All other transfer rates were defined earlier.

These equations are solved numerically as a function of time and temperature using $n_0 = 1$ and $n_i = 0$ for initial conditions. The time-evolution of exciton populations are calculated with time increments of 4 ps. The instantaneous PL intensities given by

$$I_i(t,T) = n_i(t,T)\Gamma_i^{(\mathrm{rad})} \tag{5.13}$$

can be directly compared with experimental TRPL curves and decay times $\tau(T)$. The PL intensity under continuous excitation is obtained by time-integrating $I(t,T)$.

5.6 Results and analysis

The model parameters listed in Fig. 5.4 were determined in two phases. First, the exchange and crystal-field coefficients were deduced from the observed optical transition energies and three additional physical considerations. Then, the parameters describing the exciton dynamics were determined by *simultaneously* fitting all experimental time decay curves and intensities.

5.6.1 Excitonic fine structure

A reliable determination of exchange (a_i) and crystal-field (v_i) coefficients minimally requires six conditions. The first set of conditions is provided by the five transition energies shown in Fig. 5.1: $X_{1,2}$ and $Y_{1,2}$ measured from an in-plane dyad and Z_2 measured from an out-of-plane dyad. Z_1 is associated with a very low oscillator strength in high-quality samples and its energy position could not be reliably determined.

A second set of conditions is obtained from these three additional considerations. First, the average value of exchange coefficients must be positive, such that dark (triplet) states are pushed below bright (singlet) states. Second, the dyad orientation with respect to the measurement axes is obtained from the polarization information gathered from both in-plane and out-of-plane dyads. This identification allows associating to each transition the required wavefunction symmetry representation and restricts the range of values for the exchange and crystal-field coefficients[90]. Finally, we use the fact that the relative intensities of Y_1 and Y_2 plateaus at 25% for $T > 10$ K (see Fig. 5.3). In this temperature regime, the thermal energy (> 1000 μeV at 12 K) overcomes the energy difference between Y_1 and Y_2 (180 μeV) such that the exciton occupation probability is uniformly distributed over both states. Populations can then be factored out of Eq. 5.13 and relative intensities are determined by spontaneous emission rates, or, according to Eq. 5.2, by their dipole moments. Equal intensities therefore imply,

$$|\langle Y_1|\hat{r}|0\rangle|^2 = |\langle Y_2|\hat{r}|0\rangle|^2. \tag{5.14}$$

This condition sets the relative weight of light- and heavy-hole components of Y_1 and Y_2 and, because the sums of light- and heavy-hole components are conserved, it affects the energy and wavefunction of the other six states. It considerably narrows down the range of admissible values and facilitate the search of the optimal solution.

These two sets of conditions are used to extract the following values of the exchange and crystal-field coefficients,

$$\begin{aligned} a_x &= 142.0\ \mu\text{eV}, \quad a_y = 202.0\ \mu\text{eV}, \quad a_z = 180.8\ \mu\text{eV}, \\ v_x &= 116.0\ \mu\text{eV}, \quad v_y = 198.4\ \mu\text{eV}, \quad v_z = -82.4\ \mu\text{eV}. \end{aligned}$$

As can be seen from Fig. 5.1(a), a precise agreement between calculated (vertical rectangles) and experimental energy values is obtained.

In Ref. [166], the uncertainty in the value of exchange and crystal-field coefficients was

estimated to be less than 25 %. We believe that the values reported here are more accurate, since additional restrictions were taken into account, such as the intensity ratio Y_1/Y_2 and the spectral position of Z_2. Small variation of the coefficients did not significantly affected energies and wave-functions and the uncertainty is estimated at about 10 %.

Although D_{2d} or other higher symmetry versions of Eq. 5.1 could not satisfactorily reproduce experimental results, the three exchange coefficients are nonetheless relatively similar and differ by less than 20% from their average value (182 μeV). In addition to strain produced by the dyad onto its environment, crystal-field coefficients indirectly take into account light- and heavy-hole confinement effects. The light- and heavy-hole splitting resulting from strain and confinement is $v_x + v_y - 2v_z$, leading to a value of 474 μeV. This energy splitting is considerably larger than the exchange energy, indicating that the exciton states preserve a dominant light- or heavy-hole character. In contrast, the exchange interaction dominates the crystal field and confinement effects for nitrogen dyads in GaP. [165]

Solution to Eq. 5.1 also provide excitonic wavefunctions. They are given in Table 5.2, along with their energy and relative dipole moment. Excitonic states can be divided in two groups: the low (high) energy group Ψ_1 (Ψ_2) shows a dominant heavy-hole (light-hole) character, illustrating again that crystal-field and confinement effects dominate the exchange interaction. The heavy- and light-hole mixing is relatively important fo[185], but it is particularly weak for D and Z states. We will therefore refer to states X_1, Y_1, Z_1, D_1 as *heavy-hole* states, and to states X_2, Y_2, Z_2, D_2 as *light-hole* states.

As expected, the relative oscillator strength is equally distributed along the three polarization directions. Interestingly, light-hole excitons (Ψ_2) gather three times the oscillator strength of heavy-hole excitons (Ψ_1).

5.6.2 Exciton dynamics

The six parameters related to the exciton dynamics were determined by *simultaneously* fitting the experimental dataset composed of 20 TRPL curves and 20 integrated intensities. They are listed in Table 5.3. Their determination was facilitated by the distinctive effects each transfer mechanism has on decay times and relative intensities and by their relative importance as a function of temperature.

As shown by the blue decay curves of Fig. 5.2, the calculated time-evolutions reproduce that of the four allowed transitions at 8K and that of Y_1 at all five temperatures. As already mentioned, only a fraction of the data experimentally measured and numerically modeled is shown, but the agreement is just as satisfactory for the 12 other TRPL curves. The

Wavefunction (Ψ_i)	PL energy (μeV)	Relative dipole moment
$\|Z_2\rangle = 0.115\psi_1 + 0.993\psi_5$	854.7	0.33
$\|X_2\rangle = 0.449\psi_2 + 0.894\psi_6$	721.7	0.24
$\|Y_2\rangle = -0.259\psi_4 + 0.957\psi_8$	571.7	0.17
$\|D_2\rangle = -0.092\psi_3 - 0.996\psi_7$	503.5	0
$\|Y_1\rangle = -0.966\psi_4 - 0.259\psi_8$	261.7	0.17
$\|X_1\rangle = 0.894\psi_2 - 0.449\psi_6$	171.7	0.10
$\|D_1\rangle = -0.996\psi_3 + 0.092\psi_7$	7.1	0
$\|Z_1\rangle = -0.993\psi_1 + 0.115\psi_5$	0	0.004

Table 5.2 Calculated wavefunctions, energies and relative dipole moments of excitons bound to a dyad of C_{2v} symmetry. The PL energies are relative to the state with the lowest emission energy, $|Z_1\rangle$. States ψ_{1-8} are presented in Table 5.1.

$\Gamma_0^{(\mathrm{capt})}$ (ns^{-1})	$\Gamma_0^{(\mathrm{rad})}$ (ns^{-1})	$\Gamma_0^{(\mathrm{nr})}$ (ns^{-1})	E_f (meV)	$\Gamma_0^{(\mathrm{ap})}$ (ns^{-1})	$W_0^{(\mathrm{hf})}$ ($\mu\mathrm{eV}^2/\ \mathrm{ns}^{-1}$)
0.051	15.4	151	4.7	4.2	263

Table 5.3 Parameters describing the exciton dynamics.

experimental decay times shown in Fig. 5.2(c) are reproduced and compared to calculated values in Fig. 5.6(a). As can be seen, the calculated decay times reproduce all important aspects of the experimental data set: 1) the distinctive decay time associated to all transitions at $T \leq 5$ K, 2) the convergence of the decay time associated to similarly polarized transitions at higher temperatures, 3) the decay time anisotropy between X and Y transitions at $T \leq 10$ K, and 4) the vanishing anisotropy at higher temperatures. The model also satisfactorily reproduces the relative intensity of all four transitions as a function of temperature. As can be seen in Panel (b) and (c), Y_1 (X_2) dominates the spectra at low (high) temperatures, X (Y) transitions show equal intensities at low (high) temperatures, and X and Y transitions make half of the total intensity. Finally, the calculated PL intensity shown in Panel (d) accurately reproduce the effect of the temperature-dependent quenching mechanism. As the model satisfactorily capture all aspects of the experimental data, an in-depth interpretation of the exciton dynamics is possible.

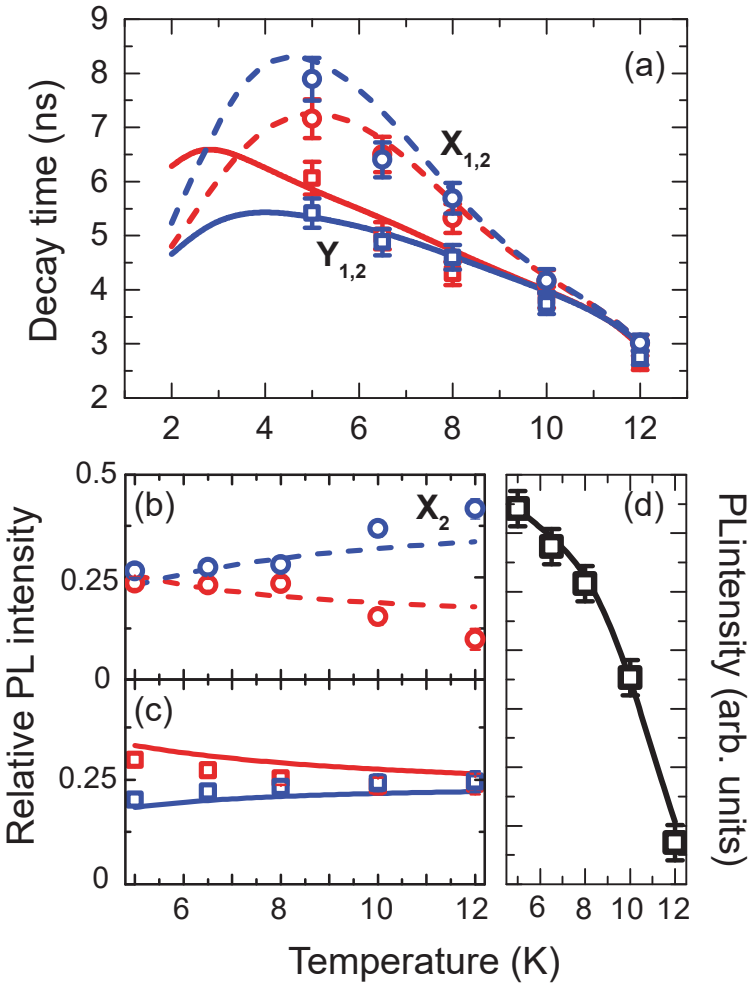

Figure 5.6 Panel (a) compares the temperature dependence of experimental and calculated TRPL decay times. Panels (b) and (c) shows the relative photoluminescence intensities of $X_{1,2}$ and $Y_{1,2}$, respectively (error bars are too small to be visible). Panel (d) shows the total photoluminescence intensity. Data points and curves represent experimental and calculated values, respectively.

Exciton capture

The capture rate $\Gamma_0^{(\mathrm{capt})}$ represents the rate at which a given state is populated by an exciton. The rate at which a dyad binds an exciton in any of the eight excitonic states is eight times superior, leading to a capture time of 2.5 ns. This capture time is long compare to that of quantum dots, which typically occurs on a timescale of hundred picoseconds. Although the exciton formation mechanism is not yet well understood, the localized and unipolar nature of the isoelectronic potential could indeed result in capture times significantly different from that of quantum dots.

In conditions where the PL decay rate of photo-generated carriers in the surrounding bulk or quantum well is faster than the capture rate, non-resonant optical pumping becomes less efficient and the PL yield is reduced. It also implies that the spin is lost through several bulk relaxation mechanisms before exciton capture. A better understanding of the capture mechanism and the identification of the limiting process appears necessary for a deeper analysis. Nonetheless, resonant excitation can be used to generate excitons and spin-polarized excitons through a relatively high dipole moment and convenient optical selection rules.

from\to	$\|Z_2\rangle$	$\|X_2\rangle$	$\|Y_2\rangle$	$\|D_2\rangle$	$\|Y_1\rangle$	$\|X_1\rangle$	$\|D_1\rangle$	$\|Z_1\rangle$	Rad. rate	Non rad. rate
$\|Z_2\rangle$	-	0.20 0.45	0.0063 0.012	0	4.7×10^{-4} 8.2×10^{-4}	2.3×10^{-4} 3.6×10^{-4}	0	*0.097* *0.15*	5.1	0.0028 1.6
$\|X_2\rangle$	0.16 0.41	-	0	0.0091 0.018	0	*14.0* *24.4*	1.3×10^{-4} 2.1×10^{-4}	2.1×10^{-4} 3.2×10^{-4}	3.7	0.0020 1.4
$\|Y_2\rangle$	0.0028 0.0087	0	-	0.66 1.5	*29.5* *58.4*	0	6.4×10^{-4} 0.0011	4.7×10^{-4} 8.2×10^{-4}	2.6	0.0014 1.2
$\|D_2\rangle$	0	0.0044 0.013	0.57 1.4	-	0.035 0.077	0.0011 0.0021	*0.43* *0.77*	0	0	0.0012 1.2
$\|Y_1\rangle$	1.3×10^{-4} 4.9×10^{-4}	0	*14.4* *43.3*	0.026 0.068	-	0	0.0054 0.011	0.057 0.12	2.6	7.0×10^{-4} 0.91
$\|X_1\rangle$	3.9×10^{-5} 1.7×10^{-4}	*3.9* *14.4*	0	4.9×10^{-4} 0.0015	0	-	0.089 0.20	0.095 0.21	1.5	5.7×10^{-4} 0.83
$\|D_1\rangle$	0	2.1×10^{-5} 9.6×10^{-5}	1.8×10^{-4} 6.6×10^{-4}	*0.14* *0.48*	0.0024 0.0074	0.065 0.17	-	0	0	3.9×10^{-4} 0.71
$\|Z_1\rangle$	*0.013* *0.065*	3.3×10^{-5} 1.5×10^{-4}	1.3×10^{-4} 4.9×10^{-4}	0	0.04 0.11	0.07 0.18	0	-	0.062	3.8×10^{-4} 0.70

Table 5.4 Exciton transfer rates (in ns^{-1}). All temperature dependent rates are given at 5 (upper entry) and 12 K (lower entry). Transfers resulting from the coupling of light- and heavy-holes through LA phonons are shown in italic. All other inter-level rates results from the hyperfine interaction.

Spontaneous emission

The rate of spontaneous emission rate $\Gamma_0^{(\mathrm{rad})}$ multiplied by the dipole moment of a given state results in the radiative rates listed in Table 5.4. The radiative recombination lifetimes associated to bright states range from 200 to 670 ps. These values are in good agreement with Rabi oscillations measurements that revealed radiative lifetimes on the order of 500 ps.[74]

For z-polarized transitions, the rate is very high (5 ns^{-1}) for Z_2 and very low (0.06 ns^{-1}) for Z_1. This is attributed to the fact that, as presented in Table 5.1, a pure heavy-hole state has a vanishing dipole moment along the z-axis. Therefore, Z_1 with its dominant heavy-hole composition is associated to a very low spontaneous emission rate.

Non-radiative emission

Fig. 5.3(b) indicates that photoluminescence quenching is well represented by a single Arrhenius equation ($I(0)/I(T)-1 = A\exp[-E_a/(k_BT)]$, where $I(0)$ is the extrapolated intensity at $T = 0$ and E_a is the activation energy) with $E_a = 5.1 \pm 0.1$ meV. However, this simple model is not strictly accurate as it supposes that all excitonic states share the same energy. The exciton dynamics model yields the temperature dependent total intensity shown in 5.6(d). The activation energy ranges from 4.7 meV for Z_2 (value shown in Table 5.3) to 5.6 meV for Z_1. The average value of 5.2 meV is similar to that obtained from the simple Arrhenius fit, which indicates that the exciton population tends to be uniformly distributed over all states as temperature increases.

The rather large value of $\Gamma_0^{(\mathrm{nr})}$ leads to a significant variation of the non-radiative emission rate for different excitonic states (see Table 5.4). At 5 K, the non-radiative lifetime ranges from 0.4 μs (Z_2) to 2.6 μs (Z_1), while at 12 K it ranges from 0.6 ns to 1.4 ns only. Over 12 K, the rate of non-radiative emission overcomes the rate of spontaneous emission, and the photoluminescence signal completely disappears.

Taking into account the binding mechanism of excitons to isoelectronic impurities [148], quenching can be either associated to 1) the escape of the hole leaving the electron bound to the nitrogen dyad, 2) the escape of the whole exciton (the free exciton energy is 1.5141 meV), or 3) the escape of the electron and hole as uncorrelated particles (the free electron and hole energy is 1.519 eV). For nitrogen dyads in GaP, it has been demonstrated [148, 165] that the dominant mechanism depends on the binding energy of the nitrogen pair configuration: the first mechanism dominates for the deepest levels, and the second and third mechanisms dominate for shallower levels. For excitons bound to the nitrogen dyad emitting at 1.5078 meV in GaAs, PL experiments under hydrostatic pressure have suggested that hole escape

can be clearly identified as the dominant mechanism only if the optical binding energy clearly exceeds the thermal activation energy[102]. In the case at hand, the binding energy of 6.3 meV is only slightly higher than the activation energy 5.2 meV and our analysis cannot discriminate between both escape mechanisms.

Inter-level transfers

Acoustic phonon induced transfers Longitudinal acoustic phonons provide the impulse and energy to drive exciton transfers between exciton states of identical polarization. As seen from Table 5.4, these transfers considerably exceeds those of exciton capture, radiative and non-radiative emission, and hyperfine mediated transfers at 12 K. Therefore, after being populated, an exciton state reaches thermodynamic equilibrium with its counterpart of similar polarization before other types of transfer occur. As a result, identical decay times for similarly polarized transitions are observed. At 5 K, phonon-induced transfer rates are comparable to radiative rates. Populations of similarly polarized states do not reach complete equilibrium and a slight difference in photoluminescence decay times appears (see Fig. 5.6a).

Hyperfine interaction is a second order process that allows transfer between dark or z-polarized states to x- and y- polarized. Transfer rates are significantly lower than spontaneous emission rates of most optically active states and phonon induced transfer rates. As can be seen from the data of Table 5.4, the dominant hyperfine transfers from X or Y states are to the closest Z or D states, and vice versa. The relatively slow transfers from D to bright states explains the long PL decay time observed.

Depending on the initial state of the exciton, different processes leading to radiative decay predominates. Directly populated $X_{1,2}$ and $Y_{1,2}$ states most likely recombine radiatively (or non-radiatively if thermal energy is sufficient) before transferring to D or Z states. Similarly, Z_2 likely recombines radiatively before transfers to X or Y state occurs. In contrast, the weak dipole moment of Z_1 allows for exciton transfer prior to radiative recombination. According to Table 5.4, a fast acoustic phonon-mediated transfer to Z_2 occurs, where radiative recombination then takes place. Although these sub-nanosecond decay rates influence the PL dynamics, they are not directly observed as two slower processes mask their presence as described next.

The PL decay time observed for Y transitions corresponds to the sum of several characteristic times associated with 1) the capture of an exciton in either dark state $D_{1,2}$, 2) the fast phonon-mediated transfer between D_1 and D_2, 3) the dominant hyperfine transfer at 5 K is then to Y_2, 4) phonon-mediated transfer efficiently mixes the population of Y_1 and Y_2 and 5) radiative emission occurs from either one of these two states. Therefore, the PL decay

time of Y-states is dominated by the slowest processes, which in this case are the capture time and the hyperfine transfer. The PL decay time for X transitions can be explained in a similar fashion. In this case however, phonon-mediated transfer from $D_{1,2}$ to $X_{1,2}$ is slower because of the larger energy splitting separating these states, explaining the longer decay time observed in Figure 5.6.

In quantum dots, experimental relaxation times at low temperature ($T \leq 10$ K) are typically in the range of 10 to 20 ns. [152, 186]. Assuming that hyperfine induced relaxation dominates in this temperature regime, scaling down the number of interacting nuclei to match that of an IC bound electron should lead to much larger Overhauser field fluctuations [178] and significantly shorter relaxation times. However, this does not appear to be the case. For X_1 and Y_1, hyperfine relaxation times are respectively 15 and 25 ns, at 5 K. Because of D_2 and Z_2 positioned nearby, the relaxation times of X_2 and Y_2 are somewhat shorter, 5.0 and 1.8 ns. Although hyperfine interaction might possibly be enhanced by the smaller number of interacting nuclei, it appears that it does not significantly affect the exciton dynamics and that spin relaxation times remain comparable to those observed from quantum dots.

Temperature evolution of the decay time. At low temperatures ($T < 2$ K), thermally activated processes are quenched and dark excitons are trapped for a timescale significantly larger than the laser repetition rate. The PL decay time is therefore determined solely by the capture of bright excitons and their subsequent radiative recombination. As temperature increases, slow hyperfine transfers from long-lived D states to bright states are activated, leading to an increase of the observed PL decay times. The maximum decay time occurs at 3.2 K for Y transitions and at 4.7 K for X transitions. This difference is again explained by the larger energy separating X states from D states. In this intermediate range of temperatures ($2 - 5$ K), inter-level transfers mediated by LA phonons are too slow to bring the exciton populations to thermodynamic equilibrium and dissimilar decay times are observed for transitions with similar polarizations. At higher temperatures, decay times are dominated by the capture of dark excitons and their hyperfine transfer to bright states. Over 10 K, decay times decrease faster, because non-radiative recombination starts to overcome every other mechanism.

Temperature evolution of relative PL intensities. Intensities are proportional to integrated occupation probabilities and radiative decay rates. In the limit of relative high temperature ($T \geq 12$ K), thermal energy is sufficient to equalize occupation probabilities of all states. Relative intensities are then proportional to radiative decay rates. As temperature is reduced, occupation probabilities are higher for lower energy states and the relative intensity of X_1 and Y_1 increase at the expense of X_2 and Y_2.

5.7 Conclusion

We have presented an extensive study of the recombination dynamics of excitons bound to nitrogen dyads in GaAs, which present a rich and complex behavior depending sensitively on temperature, on symmetry representation, and on the light- and heavy-hole content of the exciton states involved. Through a simulation of the experimental data using a comprehensive model, we were able to identify the nature of the mechanisms governing the recombination dynamics and extract quantitative informations on these processes. We have identified that exciton capture and inter-level transfers mediated by the hyperfine interaction are slow processes responsible for the slow and anisotropic decay times experimentally observed. Furthermore, we have demonstrated that deformations induced by LA phonons couples heavy- and light-holes. This phenomenon is relatively unique to systems with near degenerate light- and heavy-hole states and leads to efficient transfers between states of similar symmetry representation. We also extracted numerical values for the radiative and non-radiative emission rates, which agree with previously reported values.

These findings significantly enhance our understanding of the dynamics of excitons bound to ICs and suggest that they are interesting candidates for the realization of electron qubits. Indeed, the electron spin-flip mediated by the hyperfine interaction is not significantly enhanced and remains comparable to that of quantum dots. Interestingly, much longer relaxation times should be obtained from ICs in a host with fewer nuclear spins, like Si or II-VI semiconductors.

CHAPTER 6 ARTICLE 3 - HIGH-FIDELITY AND ULTRAFAST INITIALIZATION OF A HOLE-SPIN BOUND TO A TE ISOELECTRONIC CENTER IN ZNSE

Authors:

Philippe St-Jean, Gabriel Éthier-Majcher, Régis André, and Sébastien Francoeur

This work has been accepted for publication in *Physical Review Letters*

6.1 Abstract

We demonstrate the optical initialization of a hole-spin qubit bound to an isoelectronic center (IC) formed by a pair of Te impurities in ZnSe, an impurity/host system providing high optical homogeneity, large electric dipole moments, and long coherence times. The initialization scheme is based on the spin-preserving tunneling of a resonantly excited donor-bound exciton to a positively charged Te IC, thus forming a positive trion. The radiative decay of the trion within less than 50 ps leaves a heavy-hole in a well-defined polarization-controlled spin state. The initialization fidelity exceeds 98.5 % for an initialization time of less than 150 ps.

6.2 Introduction

Interfacing long-lived solid-state qubits with optical fields is the cornerstone of long-distance transmission of information inside quantum networks[20]. Optically addressable hole-spins bound to semiconductor nanostructures are promising candidates for building such quantum interfaces[62, 63, 187, 188]. Indeed, their energy splitting with trion states typically resides within the optical or near-infrared region of the electromagnetic spectrum, allowing for an efficient mapping of their quantum states onto photon polarization states that can be transmitted through optical networks. In addition, the coherence time of hole-spins is usually an order of magnitude longer than that of electrons, as p-type wave-functions mitigate the hyperfine interaction with nuclear spins [134, 140].

However, the scalability of quantum networks using optically addressable spins is compromised by the challenging task of finding an emitter that provides both a strong electric dipole moment and a high optical homogeneity. The first allows rapid and high-fidelity optical initialization, control, and single-shot read-out of quantum states. The second facilitates

scalabitily by alleviating implementation complexity and providing easier means to interface qubits together, to a cavity, and to an external driving field. On the one hand, systems exhibiting strong electric dipole moments, such as charges confined to epitaxial quantum dots, usually suffer from important inhomogeneous broadening. On the other hand however, highly homogeneous systems, such as impurity-bound charges (e.g. defects in diamond and SiC), usually exhibit electric dipole moments at least one order of magnitude weaker than semiconductor nanostructures[70, 189]. It is in this context that impurity-bound excitonic complexes in various semiconductor hosts are actively investigated [72, 73].

Lesser known in the context of quantum information, isoelectronic centers (ICs) in semiconductors provide both key advantages. Formed from one or few isoelectronic impurities, ICs provide the exceptionally high optical homogeneity of atomic-size systems with an inhomogeneous broadening determined by the quality of the host crystal. ICs bind single electrons or holes, and multiple excitonic complexes like excitons, trions, and biexcitons [108] with electric dipole moments as strong as in quantum dots[74]. Although several IC systems have been studied over the past decades,[93, 96, 100, 104, 117, 190] pairs of Te atoms (dyads) in ZnSe offer unique advantages for implementing optically addressable spin qubits. Most isotopes of Zn, Se, and Te have vanishing nuclear spins, thereby favoring long spin relaxation and coherence times. Te dyads primarily bind holes, which further reduces hyperfine interaction with nuclear spins, and positive trions that can be used, through their optical selection rules[108], as intermediate states to initialize a hole-spin in a well-defined state. Contrary to single-atom ICs and dopants, lower dyad concentrations are readily achieved eliminating the need for sub-micron patterning, which facilitate their integration in nanophotonic devices such as optical cavities and waveguides.

In this letter, we demonstrate fast on-demand optical initialization of a hole-spin bound to an IC formed by a pair of Te atoms (dyad) inside a ZnSe host. In doing so, we also demonstrate a novel initialization scheme, proper to IC systems, based on the efficient tunneling of an exciton from a resonantly excited donor-bound state to a single hole bound to an IC. The rapid radiative decay of the trion leaves a single hole bound to the dyad in a well-defined spin state, with a fidelity given by the degree of polarization of the emission. Under favorable excitation conditions, this fidelity exceeds 98.5 %.

6.3 Sample and experimental method

The samples investigated were grown by molecular beam epitaxy on a GaAs-(100) substrate and consists of a single Te-doped plane at the center of a 80 nm-thick ZnSe layer. The estimated density of Te atoms is 2500 μm^{-2}, leading to a dyad density of 4 μm^{-2}. Micro-

photoluminescence measurements were performed in a 1 μm^2-resolution confocal microscope at $T = 4\ K$. Excitation was provided by a frequency-doubled tunable 1-ps Ti-sapphire laser and emission was analyzed with a spectrometer coupled to an avalanche photodiode providing a spectral resolution of 60 μeV and a temporal resolution of 80 ps. Time-integrated (CW) measurements were performed with a 405 nm laser diode and a CCD camera. The polarization of the excitation and the detection were both controlled with a $\lambda/4$ wave-plate and a polarizer.

Fig. 6.1 (a) presents a CW micro-photoluminescence spectrum measured at 4K. The 5 meV wide emission observed slightly above 2800 meV is associated to the radiative recombination of neutral donor bound excitons (D-X_0)[116]. The chemical identity of these donors have not been conclusively identified, but may result from aluminium atoms on zinc sites. The emission from Te dyads is found between 2710 to 2790 meV. Emission over this wide energy range is attributed to the existence of several Te dyad configurations with different interatomic separations. This is similar to the well-known emission observed from N dyads in GaP[96] or GaAs [102, 104], where the exciton binding energy varies over a range of about 150 meV with N separation. As this interatomic separation is rigidly set by the anionic sublattice, the emission energy varies in large discrete steps. The inhomogeneous broadening associated with a given dyad configuration is then only limited by its environment. Polarization studies of the exciton emission revealed that most Te dyads in this δ-doped layer have a C_{2v} symmetry with impurities aligned along $< 110 >$[108, 117]. Due to the compressive strain created by the GaAs substrate on the ZnSe layer, light-holes are pushed 12 meV towards higher energy and only heavy-hole excitonic complexes are observed.

Te is a pseudo-donor that can trap an itinerant hole in a short-range potential[80, 86], which can then trap through its Coulomb field an electron to form an exciton or an exciton to form a positive trion. The spectrum shown in Fig. 6.1(a) presents three Te dyads binding an exciton (X_0), a positive trion (X^+) and a biexciton (XX_0). Two key results suggest that trions are positively charged: their binding energy is positive with respect to the neutral exciton and their diamagnetic shift is only slightly superior to that of the exciton[108]. Had the trion been negatively charged, the binding energy would likely have been negative due to the hole-attractive potential of Te and the diamagnetic shift would have been significantly reduced or even negative[126], as the final state would be that of a free or very weakly bound electron. As will be discussed later, the polarization memory observed in this work and the high efficiency of the spin initialization process confirms that the extra charge is positive. From the reminder of this work, we describe and analyze the emission from positively charged trions (X^+) as the one shown in 6.1 (d) and (e).

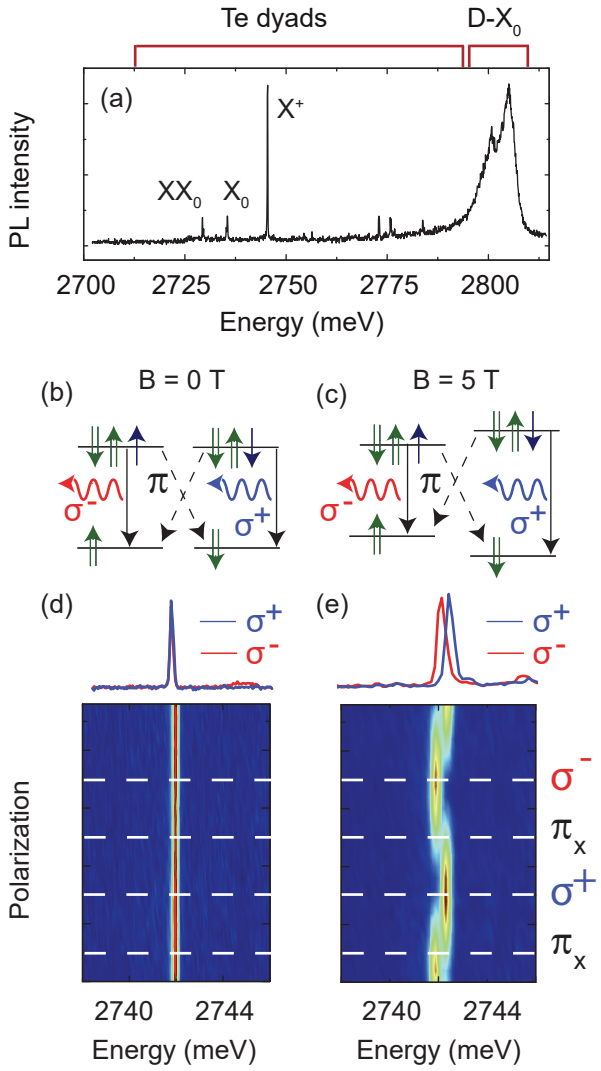

Figure 6.1 (a) Time-integrated micro-photoluminescence spectrum of the sample studied in this work. This spectrum reveals the presence of a three distinct Te dyads preferentially binding neutral excitons (X_0), bi-exciton (XX_0), and positive trions (X^+). (b) and (c) Schematic diagrams of the selection rules associated to trion emission at $B = 0$ and 5 T in a Faraday configuration. σ and π represent circularly and linearly polarized transitions. (d) and (e) Trion photoluminescence intensity as a function of the excitation energy and circular polarization at these magnetic field values.

Optical initialization requires the strong optical selection rules depicted by the strait arrows in Fig. 6.1 (b)-(c): the circularly polarized emission, σ^+ or σ^-, of heavy-hole trions (X^+) initializes the hole in spin state $J = -3/2$ or $J = +3/2$, respectively. However, this process is efficient only if these hole states are exempt from any admixture from the light-hole states, since mixing add two linearly polarized (π) emission channels (dashed lines in Panels (b)-(c)) compromising the fidelity of this optical initialization scheme. Two key results indicate a low valence band mixing despite their energy separation of only 12 meV. First, luminescence under a magnetic field in Faraday configuration does not reveal the presence of additional linear polarized transitions (Fig. 6.1 (e)). Second, an analysis of the polarization-resolved PL intensity of exciton states (see Supplementary Information), which present a more complex fine structure than trions due to the non-vanishing exchange interaction, with a model similar to those developed in Ref. [125, 185], give an LH admixture of 0.6 %. This LH-HH mixing is lower than those typically observed in quantum dots[185], due to lower symmetry-breaking in-plane anisotropic strain fields, and appears to be another distinctive feature of ICs [43, 125]. We next discuss the trion emission with the assumption that the LH-HH mixing has negligible effects.

6.4 Initialization of a hole spin

As shown Fig. 6.2(e), the degree of polarization of the trion emission depends sensitively on the energy of the circularly polarized excitation. Two dyads exhibiting very similar behaviors are presented: Dyad 1 corresponds to the one shown in Fig.6.1, and Dyad 2 is another dyad of C_{2v} symmetry emitting at a slightly higher energy (2.765 e V). Panels (a) to (d) show the time-dependence of the luminescence of Dyad 1 under co-polarized (σ^+/σ^+ or σ^-/σ^-) and cross-polarized (σ^+/σ^- or σ^-/σ^+) excitation and detection for the three excitation energies indicated in panel (e). The degree of polarization is discussed next, starting from high energy excitation.

For an excitation energy ($\sim$250 meV) above the gap, the trion photoluminescence exhibits a small but non-zero degree of polarization (15 %) indicated by the horizontal dashed line. As the excitation energy decreases, the degree of polarization slowly increases and at 2885 meV (65 meV above the gap), the degree of polarization reaches 30 %. Panels (c) and (d) from which the degree of polarization was calculated show that both σ^+ and σ^- excitations lead as expected to identical degrees of polarization and decay times. At these energies higher than the LH bands but lower than the split-off bands, spin-up and spin-down electrons are generated in a 1:3 ratio (3:1) under a σ^+ (σ^-) excitation[119], which limits the degree of polarization to a theoretical maximum of 50 %. The lower polarization observed results from

electron spin randomization in the thermalization, diffusion, and capture processes.

Decreasing the excitation energy such that only the HH bands are excited significantly increases the degree of polarization: from 30 % at the LH bands to more than 80 % at the HH band (Panel (b)). Although exciting below the LH bands is clearly favorable, exciting resonantly at the HH extremum lead to an optimal polarization as k-dependent spin-admixture and spin-relaxation processes are minimized. At this band edge, σ^- (σ^+) photons now only generates spin-up (-down) electrons in the conduction band. The reduced polarization observed implies that some electron spin relaxation processes remain effective. Nonetheless, this very strong polarized emission provides conclusive evidence that trions bound to Te dyads carry a net positive charge. Spin-orbit interaction randomizes hole-spins on a picosecond time scales [191], such that negative trions, two electrons in a spin-singlet state and a heavy-hole spin state solely determining the emission polarization, would not exhibit any polarization memory.

For an excitation energy below the HH band gap, the optical generation of charge carriers is inhibited by the lack of absorption in the ZnSe layer. However, it is possible to recover efficient trion emission by optically pumping the donor-bound excitons band (D-X_0) shown in Fig. 6.1 (a). At an excitation energy of 2.805 eV, the degree of polarization measured from several dyads is greater than 98.5 %, a figure which is limited by the noise associated to the measurement. This high polarization memory results from three processes efficiently preserving the spin of the electron: resonant excitation of donor-bound spin-polarized excitons, exciton tunneling to Te dyads, and trion emission.

Resonant excitation of bound excitons suppresses most spin-orbit related relaxation processes occurring at the HH band edge. Bound electrons have been shown to exhibit long relaxation ($T_1 \sim 1.6\mu$s [192]) and dephasing ($T_2^* > 30$ ns [193]). For the time during which they are bound to the donor, the exciton spin is preserved because, in contrast to quantum dots, donors exhibit a high symmetry (T_d) effectively protecting them from exchange-induced precession mechanisms. The efficient recovery of trion emission indicates that donor-bound excitons rapidly tunnel to nearby Te dyads before their radiative recombination lifetime estimated at > 200 ps [193]. Phonon-assisted tunneling of charges from donors to ICs have been demonstrated in various IC systems [124, 165, 194], and is expected to be very efficient in ZnSe due to the relatively strong electron-phonon coupling. Our results demonstrate for the first time that this tunneling efficiently preserves the electron spins. Finally, during the short trion lifetime before radiative recombination, the electron spin does not experience significant relaxation and, as discussed above, the HH-LH mixing has a negligible effect of emission selection rules. Following this polarized emission, the hole is bound to the IC in a spin state

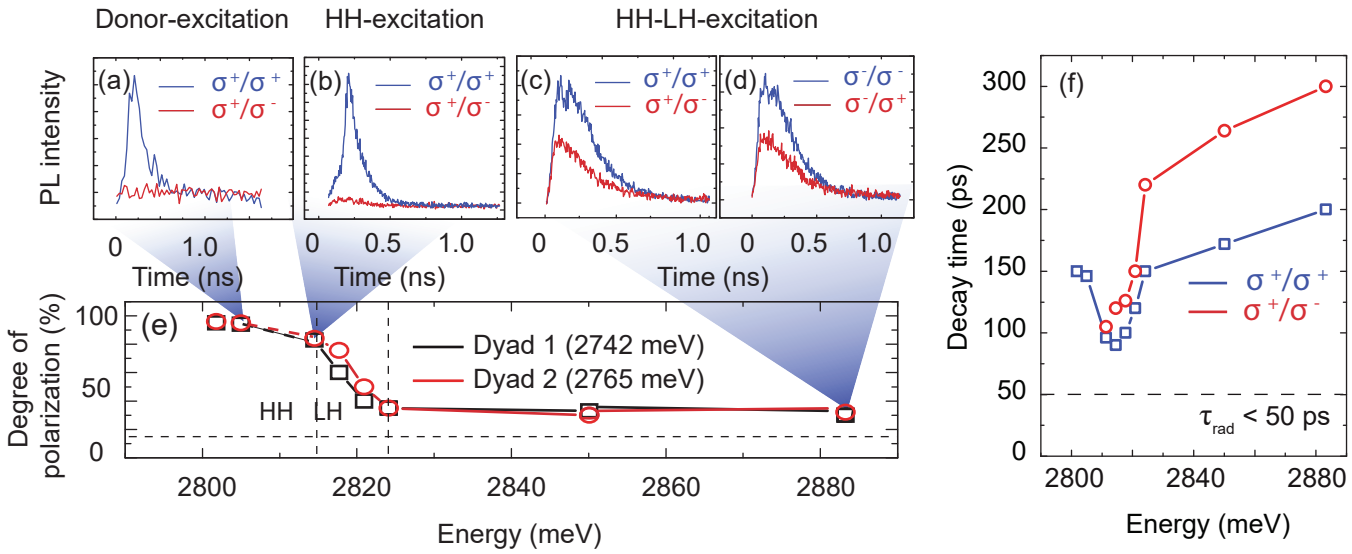

Figure 6.2 Time-resolved photoluminescence of trions bound to dyad 1 presented in panel (a) of Fig. 6.2 for excitations tuned to the D-X^0 band (a), to the HH band edge (b), and far above the LH band edge but below the spin-orbit band edge (c)-(d). The blue (red) curves show the emission intensity under co-polarized (cross-polarized) circular excitation and detection. (e) The horizontal line indicates the degree of polarization of the emission for an excitation energy 250 meV above the ZnSe band gap. (f) Decay times of trion emission for co- (blue squares) and cross-polarized (red circles) configurations as a function of the excitation energy for dyad 1. The dashed line indicates the upper bound for the radiative decay time of trion states (< 50 ps)

given by the polarization of the emission as indicated in Fig. 6.1 (a). In contrast, to other reported spin initialization schemes, such as coherent population trapping [195, 196], ionization of excitons [197, 198] and optical pumping [61, 72, 199], our scheme does not require resonant excitations of trion states, special sample structure, or external magnetic fields, but nonetheless achieves near-unity fidelity.

6.4.1 Decay time of trions luminescence

Through the decay time of the trion photoluminescence, we demonstrate that this high-fidelity spin-initialization can be achieved on a picosecond timescale. Figure 6.2 (f) indicates the decay time of trion emission as a function of excitation energy and polarization configuration. Decay times are obtained from mono-exponential fits of the experimental decay curves such as those presented in Fig. 6.2 (a)-(d). For all excitation energies, the decay times are one order of magnitude lower than that of excitons[117, 125], which is explained by the absence of dark states influencing the dynamics. Nonetheless, these decay times are significantly longer than the spontaneous emission time estimated from the spectral linewidth or Rabi oscillations measurements, which both indicated a spontaneous lifetime of less than 50 ps (indicated with the dashed line in Fig. 6.2 (f)). The observed decay time is therefore dominated by processes occurring prior to radiative emission.

At an excitation energy of 2880 meV, trion decay times are respectively 200 and 300 ps for co- and cross-polarized configurations. This significant difference is explained by the coexistence of two factors: 1) different initial electron spin populations (spins are generated in 3:1 ratio), and 2) the presence of spin-flip mechanisms prior to trion formation on the Te dyad. A balance population model taking into account these two factors reveal a capture time (all processes prior to trion formation) of 180 ps and a spin-flip time of 450 ps. This dynamic is strikingly different for trions bound to N dyads in GaAs, where the spin-flip rate dominates the capture time, yielding identical decay times irrespective of the polarization configuration. From 2880 to 2825 meV, decay time decreases due to lower excess energy and momentum, and spin-flip time increases as indicated by the higher polarization memory shown in Fig. 6.2.

Below the light-hole band gap, both decay times abruptly shorten. Although there is less energy and momentum to shed, it also becomes increasingly favorable to form excitons instead of electron-hole pairs. Approaching the heavy-hole gap, exciton formation dominates and a capture time of 92 ps is recorded. This regime of accelerated capture suggests that the most efficient trion formation mechanism is through whole exciton capture. This mechanism is probably even faster than the value quoted due to the limited time-resolution of the detec-

tion system, demonstrating that both the capture time and the spontaneous emission lifetime are indeed quite fast. At the heavy-hole gap edge, decay times for both polarization configurations are similar, since the time associated to spin-flip events is now much longer than the capture time. Finally, the decay time of the trion luminescence for resonant excitation of the donor bound exciton (D-X^0) is 150 ps. It is principally determined by exciton tunneling time from the neutral donor to the Te dyad, which is similar for every dyads measured due to the relatively high donor concentration. In contrast to heavy-hole band edge excitation, exciton capture is slower, but it better protects the electron-spin as demonstrated earlier.

These initialization times are several orders of magnitude faster than optical pumping schemes with an external magnetic field in Faraday configuration [199] (μs-timescale and fidelities of 99.5 %), and one order of magnitude faster than optical pumping schemes in Voigt configuration [200, 201] (ns-timescale and fidelities of 98.9 %). This speed-up allows for the initialization on timescales much shorter than the expected coherence time of hole-spins in ZnSe. In fact, this initialization time is comparable to those obtained through field induced exciton dissociation. This last approach however requires an adapted sample structure for electron ionization, a preselection of quantum dots with low fine-structure splitting, and an elaborate strategy to suppress exchange-induced spin precessions prior to ionization. [198]

6.5 Conclusion

In summary, we have demonstrated picosecond optical initialization of a hole-spin bound to a Te IC in ZnSe with sufficiently high fidelity ($F > 98.5$ %) and low operation time ($T < 150$ ps) for implementing error correction protocols[202]. The efficiency of the initialization scheme used, based on the rapid spin-preserving tunneling of excitons from donor-bound states to Te dyads occupied by a single heavy-hole, arise from the long relaxation time of donor-bound excitons, the very low admixture of light-hole states, and the very short radiative lifetime of IC-bound trions. The next step would be to evaluate the hole spin relaxation and coherence time, and to demonstrate complete optical control. Due to the moderate light- and heavy-hole splitting and concomitant low light- and heavy-hole mixing, LH states provide the appropriate Λ level structure necessary for coherent control and HH states provide robust recycling transitions for single-shot readout [43].

CHAPTER 7 GENERAL DISCUSSION

The articles that were presented in this thesis follow a progression from the study of exciton qubits bound to ICs toward that of spin qubits. More precisely, the first two articles investigated the dynamics of excitons bound to ICs and allowed the identification of the important mechanisms involved during their recombination, and the last article demonstrates the initialization of a hole-spin qubit. In light of these results, I present hereafter a brief discussion to summarize and put in perspectives the major contributions of these works to the field of ICs and, more generally, to the field of optically addressable qubits.

7.1 Dynamics of excitons bound to N ICs in GaP - Article 1

The first article of this thesis presents a study of the dynamics of excitons bound to N ICs in GaP that combines time-resolved PL measurements with a complete balance of populations model describing the temporal evolution of exciton occupation probabilities for every state forming the fine structure. This complete model has allowed to confirm the reexaminations of the HTL model of exciton capture that were previously reported (particularly in Ref. [80, 132, 148]); this observation of different capture mechanisms indicates as well that non-radiative recombination is dominated by different mechanisms, which were precisely identified. Furthermore, it has allowed as well to investigate the mechanisms underlying exciton inter-level transfers and radiative recombination, both of which had never been studied.

7.1.1 Reexamination of exciton capture and non-radiative recombination

As mentioned in Chapter 3, previous theoretical [83] and experimental [132, 148] works have determined that the HTL model for exciton capture (describing the sequential binding of a primary charge by the IC short-range potential, and then of a secondary charge by Coulomb interaction) does not hold for all ICs in GaP, but only for deeper centers ($NN_i, i \leq 3$). Shallower centers ($NN_i, i \geq 6$) directly bind excitons either through the capture of free excitons (by the crystal deformation induced by the IC [83]) or through their thermally-activated tunneling from single N-bound state [132]. For ICs presenting intermediate exciton binding energies ($NN_{4,5}$), the nature of the mechanisms involved was still unclear and debated.

The argument underlying this reexamination arises from the claim that the short-range binding potential of shallow ICs is too weak to bind single charges [148], and can thus only bind free excitons directly. Similarly, this weak short-range potential should as well affect the

mechanisms involved in exciton non-radiative recombination, because the unbinding of the charges forming the exciton should necessarily lead to the escape of both the hole and the electron; in comparison, non-radiative processes for deeper centers are expected to be dominated, at low enough temperatures, by the escape of the weaker-bound hole only.

Two important results of Article 1 agree with these reexaminations of exciton capture and non-radiative recombination: the dominance of tunneling in the capture of excitons by NN_6 at high temperatures, and the extracted activation energies of non-radiative processes for the different ICs.

1- Apparition of a dominant tunneling effect at high temperatures

The plateau observed in the PL decay times of NN_6 clearly demonstrates that exciton tunneling, for this configuration, is an important and efficient binding mechanism, presenting characteristic tunneling times as low as 400 ps at $T \geq 45\ K$. For deeper dyads, however, higher temperatures would be required for exciton tunneling to become the dominant capture mechanism ($T > 60\ K$), and it is expected, at these temperatures, that non-radiative recombination of excitons dominates their radiative decay. This is a very important observation, because the scheme developed in Article 3 for initializing a hole-spin takes profit of this efficient tunneling to bind a trion in a well-defined spin state.

2- Activation energies of non-radiative processes

Previous experimental investigations of the non-radiative mechanisms [84, 148] were based on the evolution of PL intensity with temperature, as thermally-activated PL quenching allows estimating the activation energy of non-radiative processes and therefore identifying their nature. The most important element that these previous analyses were lacking is the influence of inter-level transfers, because these thermally-activated effects should as well affect the PL intensities. Our findings, based on balance of populations models involving all inter-level transfers, provide a more precise identification of the mechanisms involved in non-radiative recombination, which are summarized in Table 7.1 together with previous assignments proposed in Ref. [84] and [148].

According to these results, non-radiative processes are dominated by hole escape for NN_1, NN_3 and NN_4, because the extracted activation energies (E_a = 44.2, 41.5 and 38.2 meV, respectively) are comparable to the hole binding energy previously reported ($E_{\mathrm{b}}^{(h^+)} \sim 40$ meV [148]). The hole binding energy is not expected to vary significantly with the IC configuration, because its Bohr radius is much larger than the size of the electron wave-function; therefore,

the electron-hole Coulomb binding is not affected, in first approximation, by the electron localization. A slight increase of the activation energy between NN_1 and NN_4 is however observed due to the small variation of the electron localization. It is important to notice that at higher temperatures than those studied ($T > 60\ K$), the escape of both the electron and the hole might start to dominate, but this regime was not observed here, as only one activation energy could be extracted from evolution of PL intensity with temperature.

These results clarify the nature of the non-radiative mechanisms associated to NN_4 which was attributed in Ref. [148] and [84] to the hole and exciton escape, respectively. They also demonstrate that NN_1, NN_3 and NN_4 can bind a single electron, and that exciton capture is therefore expected to be dominated by the HTL sequential model. This could open the way to bind a single electron to either of these configurations, e.g. by applying a sufficiently strong electric field to break a bound exciton, in order to form a spin or charge qubit, or to implement a classical bit on an atomic-size physical support.

The mechanism involved in non-radiative recombination of excitons bound to NN_6 and to single N, was determined to be the escape of the whole exciton, as the activation energies (E_a = 21.3 and 13.9 meV, respectively) are significantly weaker than hole binding energy, confirming results from previous works. Adding these activation energies to the spectral position of the associated IC lead to a final state located 10-15 meV below the band gap, indicating that the final state of the non-radiative process corresponds to a free exciton.

Table 7.1 Non-radiative recombination mechanisms associated to single N and NN_i ICs (hole or exciton escape) determined in this work as well as in previous works presented in Ref. [84, 148]. The activation energies extracted for these mechanisms (E_a) are presented as well as the emission energy (E_i).

ICs	E_i (eV)	E_a (meV)	Non-radiative mechanisms		
			This work	Ref. [148]	Ref. [84]
A-line	2.3171	13.9	Exciton	Exciton	Exciton
NN_6	2.3035	21.3	Exciton	Exciton	Exciton
NN_4	2.2891	38.2	Hole	Hole	Exciton
NN_3	2.2645	41.5	Hole	Hole	Hole
NN_1	2.1850	44.2	Hole	Hole	Hole

7.1.2 Evaluation of exciton radiative decay and inter-level transfers

Although exciton radiative decay and inter-level transfers had been discussed in previous works [96], quantitative information on the rate of these processes was still lacking. The decay and transfer rates extracted in this work therefore correspond to the first precise estimation of the strengths of these mechanisms.

In the context of optically addressable qubits, the most important aspect regarding the rates of radiative decay and inter-level transfers does not regard their absolute value, but rather their ratio: for shallower centers (NN_6 and the A-line), the radiative decay rate is at least an order of magnitude slower than exciton transfer; for deeper centes ($NN_{1,3,4}$), it is at least three orders of magnitude slower. This is very problematic as the exciton spin states flip many times before its spontaneous emission, which is contrary to the requirement of a long coherence time relatively to the spontaneous emission time.

In regard of this, it clearly appears that ICs presenting stronger optical coupling and weaker inter-level transfers are highly desirable (with the caveat that optical spontaneous emission will lead lower gate fidelities). This has therefore triggered our following investigations of N dyads in GaAs (a direct band gap semiconductor host that exhibits faster spontaneous emission [106]), and of Te dyads in ZnSe (a direct band gap semiconductor where inter-level transfers are expected to be strongly mitigated due to the low concentration of nuclear spins [117]).

7.2 Dynamics of excitons bound to N ICs in GaAs - Article 2

The second article presented in this thesis studies the dynamics of excitons bound to N dyads in GaAs. As mentioned above, the most important advantage of this IC system, in comparison to N in GaP, is the strong oscillator strength of bound excitons [106], allowing for a more efficient optical control. In the following, I discuss several results of this article, mostly focusing on how they affect the potential of N dyads for building optically addressable qubits, and how they compare with exciton qubits confined in QDs.

7.2.1 Exciton fine structure

The analysis of the exciton fine structure realized in Article 2 exceeded that presented in previous works [90, 91], and has thus led to a more precise identification of the energy splittings and LH-HH mixing of every exciton eigenstates. Accurate determination of angular and spin composition of every state forming the fine structure is a crucial step toward efficient

coherent manipulation of exciton qubits as it furnishes quantitative information on their coupling with optical fields as well as with other excitonic states.

For ICs the calculated LH-HH mixing ratio typically ranges around ~ 10 %, and does not vary significantly from one center to the other (all N ICs investigated exhibited comparable mixing). In comparison, recent calculations of the LH-HH mixing in InAs QDs have revealed that the average ratio is ~ 15 % but could exhibit strong variations from one dot to another, being possibly as high as ~ 50 % [185]. This non-negligible and highly inhomogeneous mixing, despite the important splitting between HH and LH states, is attributed to the presence of anisotropic strain fields that are very hard to control during the growth of the dots. Since the polarization of the emission strongly depends on valence band mixing, this inhomogeneous variation from one dot to the other represents an important threat to the scalability of QDs. The atomic nature of ICs, on the other hand, insures that these crystal-field deformations are much less important leading to a higher homogeneity of the LH-HH mixing.

7.2.2 Radiative recombination vs. inter-level transfers

I pointed out that the most interesting aspect of N ICs in GaAs is their stronger coupling to optical fields compared to GaP. Prior determination of the exciton electric dipole moment through optically driven Rabi oscillations has indeed revealed spontaneous emission times on the order of 500 ps [74], which is 2 orders of magnitude faster than for excitons bound to N ICs in GaP [101]. In the second article, these values were confirmed for every state of the fine structure (ranging from 200 to 700 ps), except for dark states, confirming that exciton qubits bound to ICs can be optically addressed on a timescale comparable to those confined in QDs. It is also an order of magnitude faster than typical values reported for NV centers in diamond, for which the radiative decay time is ~ 10 ns [69].

Although spontaneous emission is a fundamentally important aspect of optically addressable qubits, it is necessary to compare the efficiency of optical coupling with that of inter-level transfers. Two important mechanisms underlying inter-level transfers were clearly identified: LA phonon interaction coupling HH and LH states belonging to the same symmetry representation, and hyperfine interaction coupling bright and dark states together.

1- LA phonon induced transfers

Contrary to epitaxial QDs where light- and heavy-hole exciton states are separated by several tens of meV [65], their near-degeneracy in IC systems leads to very effective phonon-mediated transfers between LH and HH states belonging to the same symmetry representation ($\psi_1 \leftrightarrow \psi_5, \psi_2 \leftrightarrow \psi_6, \psi_3 \leftrightarrow \psi_7, \psi_4 \leftrightarrow \psi_8$). These very rapid transfers (ranging from 30 ps

to 10 ns as the energy splitting changes from 300 to 850 μeV) are not observed in QDs and are very detrimental to the coherence of exciton qubits.

Their effect could however be mitigated by applying a biaxial strain, e.g. by growing the GaAs host on a substrate presenting a slight lattice mismatch such as $In_{1-x}Ga_xAs$. Consequently, the biaxial strain field would lift the degeneracy between LH and HH states, thus rapidly quenching these transfers, similarly as for epitaxial QDs or for the ZnSe sample used in the last article.

2- Hyperfine interaction

As mentioned in Chapter 3, hyperfine interaction is the most important mechanism leading to qubit decoherence in semiconductor QDs [135]. The results presented in this work indicate that hyperfine interaction is as well one of the main mechanisms responsible for exciton spin flip in IC systems. The inter-level transfer rates associated to this mechanism ranges between 2 and 20 ns depending on the splitting between states involved and the composition of the wave-functions; in InAs QDs, hyperfine mediated spin flips were estimated to be as well on the order of 10-20 ns [152, 186].

Similarly as for QDs, hyperfine interaction in IC systems therefore represents a significant hurdle for realizing long coherence qubits. The most promising avenues for mitigating its effect on exciton coherence are identical as for QDs: using hole-spin qubits rather than exciton or electron-spin qubits [134], and building spin free semiconductor hosts. These considerations triggered the work presented in the last article describing the initialization of a hole-spin in a ZnSe host.

7.3 Article 3- Hole-spin initialization schemes

The last article presented in this thesis demonstrates ultrafast $T \leq 150$ ps and high-fidelity ($F \geq 98.5$ %) initialization of a hole-spin bound to a Te dyad in ZnSe. This is the first demonstration of qubit initialization for a hole-spin bound to an impurity as previous demonstrations were realized either with electrons or in QDs [61–63]. Furthermore, one key aspect of this work is the demonstration of a novel initialization scheme based on the spin-conserving tunneling of excitons from resonantly excited donor-bound states to a Te dyad with a bound hole, thus forming a positive trion; the radiative decay of the trion leads to a hole-spin initialized in a well-defined state. The significant advantage of this scheme compared to those reported in QDs, is that it does not require a magnetic field, a resonant excitation of the trion, or the nanofabrication of electrical contacts, but provides nonetheless near-unity fidelities and very rapid initialization times. In the following, I briefly overview the schemes that

were used for initializing hole-spin in semiconductor QDs in order to discuss quantitatively the advantage of the scheme elaborated in this last article.

7.3.1 Optical pumping of a hole-spin

Historically, the first demonstrations of optical initialization of both single electron [199] and hole-spin [61] confined in a QD were realized through optical pumping schemes. However, as summarized in Ref. [127], there are significant differences between the experimental details concerning the optical pumping of electron and hole-spin, but we shall only focus here on the details related to hole-spin initialization. Two configurations of magnetic fields can be used to initialize a hole-spin: (1) no magnetic field, and (2) magnetic field in Voigt configuration; both present different advantages and disadvantages, which we describe hereafter.

No magnetic field

In the absence of HH-LH mixing, the optical selection rules of positive trions are restricted to only two uncoupled transitions, as depicted in Fig. 7.1 (a): $|\Uparrow\Downarrow,\uparrow\rangle$ and $|\Uparrow\Downarrow,\downarrow\rangle$ trion states are coupled to $|\Uparrow\rangle$ and $|\Downarrow\rangle$ hole-spin state, respectively; conservation of angular momentum imposes that these transitions be circularly polarized σ^- and σ^+, respectively. Consequently, under a resonant circularly polarized driving field, only one state is optically active while the other is inactive.

Optical pumping of a hole-spin takes profit of these strict optical selection rules to initialize the hole in the optically inactive state, according to the following picture. Before the initialization, the hole can be found in either spin state with a 50 % probability. Following the application of a resonant driving field, if the hole-spin is in the optically active state it will be excited to the corresponding trion state. Then, the excited trion can either radiatively decay back to the initial hole-spin state or transfer to the other trion state, due to the non-negligible hyperfine interaction between the electron and nuclei spins (γ_{hf}), where it can radiatively decay in the inactive hole-spin state. The driving field continuously re-pump the hole in the trion state until it relaxes in the inactive state, and the probability to find the hole-spin initialized in this latter state thus increases monotonically with time. Due to the much stronger relaxation time of trions (typically $\gamma_{hf} \sim 1$ ns [61]) in comparison to that of the hole (typically > 100 μs [61, 203]), the relaxation of the hole-spin during the initialization is a negligible effect.

Using this scheme, initialization fidelities up to 99 % were demonstrated [61] for initialization times exceeding 100 ns [203]. The disadvantages of this technique are that (1) it is not

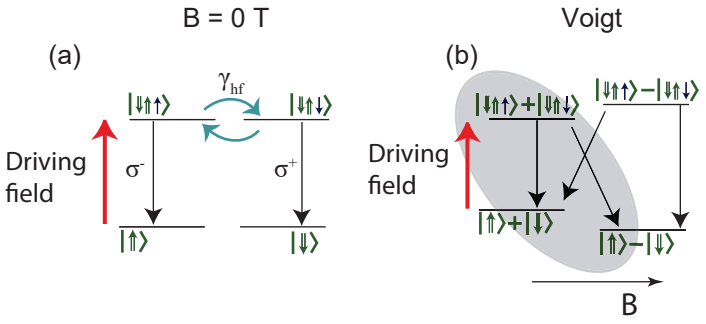

Figure 7.1 (a) The optical pumping schemes require a Λ system where the spin states are split and are connected to an excited state, here a trion state. (b) In Faraday configuration, the Λ system is provided by the HH-LH mixing that opens the cross transitions (dashed lines) radiative channels. (c) In Voigt configuration, the Λ system is provided by the in-plane magnetic field that mixes the spin-up and -down state.

compatible with previously reported scheme of optical control of a hole-spin based requiring Λ level structures, rather than uncoupled transitions [53], (2) the efficiency of the initialization relies on a strong hyperfine interaction, which in turn is detrimental to the coherence time of the hole-spin, and (3) the initialization time is very long in comparison to trion spontaneous emission time (typically ranging between 0.5 and 1 ns).

Voigt configuration

Optical pumping in Voigt configuration was developed initially for electron spin in QDs [200, 201], but can be identically used for hole-spins [62, 204], where it allows to circumvent the disadvantages of the previous configuration. According to the electron and hole Hamiltonians developed in Chapter 2, a magnetic field in Voigt configuration (perpendicularly to the optical axis) strongly mixes the spin states, leading to four non-degenerate transitions with rapid radiative decays ($T \sim 0.5 - 1\ ns$) (see Fig. 7.1 (b)).

These four transitions form two Λ level structure between two hole-spin states and the trion states, either of which can be used to initialized the hole-spin (e.g. that define by the gray area in Fig. 7.1 (b)). The initialization scheme is very similar to that without magnetic field, as a resonant driving field couples one spin state to one trion state, leaving the other spin state optically inactive due to the energy mismatch induced by the Zeeman splitting (here again, this inactive state corresponds to the initialized state). The radiative decay of the trion can lead to either spin state with similar probabilities; the optically active hole-spin state is re-pumped until the trion decays in the inactive state.

The much more efficient path for populating the optically inactive hole-spin state (which does not require hyperfine interaction) leads to initialization times that can be lowered by two orders of magnitude, reaching the ns timescale ([62]). The cost of this speed-up is that both spin states are now coupled to the trion states with the same strength; it is therefore possible for the initialized spin to be pumped back to the optically active state if the Zeeman splitting is not strong enough. The fidelities achieved are therefore lower than for the previous scheme, and requires strong magnetic fields in order to achieve near-unity fidelity. For hole-spins, a fidelity of 91 % was demonstrated at 6 T [204], but fidelities of 98 % at 1 T were demonstrated for electron spins [201]. Furthermore, Voigt Configuration brings important complications to the single-shot read-out of the quantum state, which typically requires uncoupled spin states to drive cycling transitions [53].

7.3.2 Coherent population trapping

Optical pumping schemes with a single pumping field only allow to initialize a spin in a well-defined state, either up or down, but no coherent superposition of these two states can be formed. Initializing a spin-state in an arbitrary superposition of states can be realized using coherent population trapping, which was demonstrated for electon spins ([195, 205, 206]) and hole-spins [196].

Coherent population trapping is very similar to optical pumping in the Voigt configuration, except that a second pumping field resonant with the second transition of the Λ system is added. The role of this second field is to insure that both spin states are coherently coupled together. If the power of the second field is set to zero, we have an architecture identical to the Voigt optical pumping scheme, and the hole is initialized in a well-defined spin state; if the first field is removed but the second is on, the hole is initialized in the other spin state, again similarly to the Voigt optical pumping scheme; if the two fields are present simultaneously, the hole will be initialized in a superposition of the two spin states, with a up-to-down proportion determined by the ratio between the Rabi pulse area (proportional to the amplitude and duration of the pulse [207]) of both driving fields.

Determining the fidelity of the superposition is however very challenging as the quantum state needs to be compared with a numerical simulation that describes the temporal evolution of the coherent superposition (e.g. by solving the set of optical Bloch equations describing the system [201, 206]). For NV centers, the fidelity was demonstrated to saturates around 80 % [206] for initialization time superior to 100 ns.

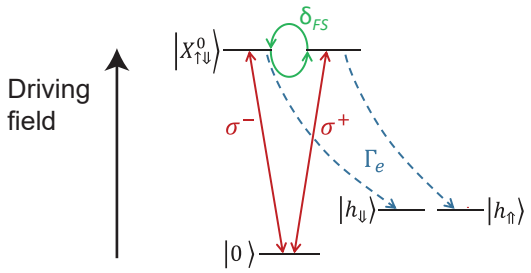

Figure 7.2 Ionization of an exciton leads to the initialization a hole in a well-defined spin state. This scheme is however limited by the exchange interaction between the electron and hole forming the exciton, as the driving field leads to an exciton in a superposition state rather than a well-defined state. ([198])

7.3.3 Ionization of excitons

The last scheme of initialization is based on the ionization of an exciton by an electric field which leaves a single hole initialized in a well-defined spin state. As illustrate in Fig. 7.2, this scheme can be separated in two steps: (1) a circularly polarized driving field excites either a $J = 1$ or $J = -1$ exciton, and (2) an electric field breaks this exciton, moving the electron outside the dot. This leaves a single hole initialized in the state defined by the polarization of the driving field in step (1).

This scheme offers very rapid initialization times (~ 100 ps), but the fidelity of the initialization can be strongly compromised by the exchange interaction. Depending on the symmetry of the QD, electron-hole exchange interaction can mix the $J = \pm 1$ exciton states to form linearly polarized X and Y states, and lift their degeneracy by several hundreds of μeV [122]. For degenerate exciton states, the fidelity of the initialization can be as high as 99.5 %, but for a 30 μeV splitting the fidelity decreases down to 60 % [198]. This is attributed to the fact that the circularly polarized pump laser excites a superposition of X and Y eigenstates that precesses at a frequency proportional to the fine structure splitting ($\omega = \Delta E/\hbar$). Therefore, the angular momentum of the pump photons is lost within the radiative lifetime of excitons, weakening the fidelity of the initialization.

Achieving high-fidelity initialization through ionization of excitons requires to mitigate the exchange interaction. This can be achieved either by controlling the growth of the underlying nanostructure in order to raise its symmetry, or by driving a second optical field, slightly detuned from one of the exciton transition, in order to push it to the same energy as the other, through the AC Stark effect (ASE) [198, 208].

The important disadvantages of this scheme is therefore the complexity of its implementation,

because it requires (1) the realization of electrical contacts for ionizing the electron, (2) a high-power (typically $\sim$ 100 W/cm^2, [198]), laser to realize the AC Stark shift, and (3) controlling the growth of the QD to minimize the exchange interaction.

7.3.4 Summary of the different initialization schemes

In Table 7.2, I present a brief summary of the initialization times and fidelities for these three schemes, as well as that developed in the last article of this thesis. I present also a checklist of the different requirements necessary for each scheme: magnetic field, resonant pumping fields, and electrical contacts.

Table 7.2 Summary of the different hole-spin initialization scheme used in Qds as well as that used in the last article. All values are extracted for epitaxial QDs, except coherent population trapping determined from NV centers in diamond. The references from which were taken the values are presented in the first column.

Schemes	Initialization time	Fidelity	Magnetic field	Resonant pumps	Electrical contacts
Optical pumping (B = 0 T) [61, 203]	100 ns	99%	No	Yes	No
Optical pumping (Voigt) [62, 204]	$1-10$ ns	91 % %	Yes	Yes	No
Coherent population trapping [206]	100 ns (NV)	90 %	Yes	Yes	No
Exciton ionization [198]	100 ps	60-99 %	No	Yes (pump + ASE)	Yes
This work (tunneling)	150 ps	98.5 %	No	No	No

CHAPTER 8 CONCLUSION AND RECOMMENDATIONS

The work presented in this thesis studied the dynamics of excitonic complexes bound to isoelectronic centers in semiconductors in order to evaluate their potential for building optically addressable qubits. As presented in Section 1.1 the technological interest of realizing optically addressable qubits is (1) to entangle remote quantum computers or memories inside a *quantum network*, and (2) to build *quantum repeaters* to prevent the loss of photon coherence in long distance transmission channel.

8.1 Requirements for building optically addressable qubits

In section 1.2, I presented three particular requirements necessary for building optically addressable qubits that were evaluated in this thesis for all three IC systems (N in GaP and GaAs and Te in ZnSe).

1. **Optical coupling requirement** - The first requirement can be separated in two aspects. Firstly, it is necessary that the quantum state of the qubit be coupled to optical fields (either in the visible or near-infrared regions of the electromagnetic spectrum), in order to couple with photons that can be transmitted with low loss through optical fibers. Secondly, it is necessary that the light-matter coupling of the qubit be strong enough to allow for efficient transfer of a quantum state from matter to photons, and vice-versa.

2. **Scalability requirement** - It is required that the qubit can be replicated in identical copies, so that increasing the number of qubits inside a network does not require a fundamental reengineering of the platform. For optically addressable qubits, the most important aspect of scalability regards the ability to build qubits with identical energy splittings, so that any added qubit can be easily entangled with the previous qubits.

3. **Coherence requirement** - Finally, the platform used for implementing the optically addressable qubits is required to preserve the coherence of quantum states over a period of time long enough to (1) transfer quantum information from matter to photon states; (2) transmit the photons to an adjacent node of the quantum network; and (3) reconvert quantum information to a matter state. Steps (1) and (3) are closely related to the optical coupling requirement as the efficiency of these transfers influences the time over which the coherence needs to be preserved.

The important problematic that this work was addressing is the very challenging task of finding a qubit platform that respects altogether these three classes of requirements. The two most promising implementations of optically addressable solid-state qubits previously studied, self-assembled QDs and NV centers in diamond, both lack one or the other of these requirements. Self-assembled QDs offer excellent coupling with optical fields, and their coherence can be enhanced up to 100 ns by using hole-spin qubits [134]; their scalability is however strongly limited due to the very challenging task of growing homogeneous ensembles of dots. Impressive long-distance entanglement has been realized with NV centers in diamond, thanks to their very long coherence time reaching milliseconds at room temperature [209], but their radiative recombination is however typically an order of magnitude weaker than QDs [69, 70] and strongly coupled to phonon emission; furthermore, their diamond host is very difficult to integrate inside optical cavities or other semiconductor heterostructures.

In the following I will describe, in light of the results obtained in this thesis, to what extent exciton and spin qubits bound to ICs fulfill these different requirements.

8.1.1 Exciton qubits bound to N ICs in GaP

Optical coupling requirement

The optical coupling of excitons, described by the rate of spontaneous emission, for all configurations of N ICs in GaP, is at least two order of magnitude weaker than that of excitons confined in QDs, ranging between $\Gamma_{rad}^{-1} = 200$ and 700 ns. This low optical coupling is attributed to the indirect band gap of the semiconductor host.

Scalability requirement

The inhomogeneous broadening of N-bound excitons in GaP is less than $\sim 50\ \mu eV$ (limited by the resolution of our experimental detection setup). This high homogeneity, in comparison with self-assembled QDs, demonstrates that atomic-size defects such as ICs allows for a much more promising scalability.

Coherence requirement

The relaxation rates extracted through balance of population modeling of excitons PL decay depend significantly on the configuration of the ICs: shallower centers (A-line and NN_6) typically present relaxation rates one order of magnitude weaker than their radiative decay ($\Gamma_{ij}^{-1} \sim 10\ ns$), while those associated to deeper centers (NN_{1-4}) are at least three orders of magnitude weaker than their radiative decay ($\Gamma_{ij}^{-1} \sim 0.5\ ns$). These rapid exciton transfers, attributed to hyperfine interaction between the spin moments of nuclei and electrons, strongly compromise the potential fo N-bound excitons in GaP for building optically addressable

qubits. The exciton dephasing has not been studied in this thesis.

8.1.2 Exciton qubits bound to N dyads in GaAs

Optical coupling requirement

The spontaneous emission time of every bright state forming the fine structure of NN_1 (only this N related ICs was studied in this thesis) ranges between 200 and 700 ps. These values are of the same order than those reported in QDs and are one order of magnitude larger than NV centers. This radiative decay rate has been confirmed by resonant PL measurements [74].

Scalability requirement

The inhomogeneous broadening of excitons bound to N dyads ($\sim 100\ \mu eV$) is slightly superior in GaAs than it is in GaP, according to our PL spectra. However, this inhomogeneity is not attributed to an intrinsic difficulty to build identical N ICs (e.g. ICs presenting similar deformation crystal-fields), and could easily be mitigated by improving the growth of the GaAs host. The optical homogeneity is however still orders of magnitudes superior than that of QDs and comparable to that of NV centers.

Coherence requirement

Two important mechanisms were identified for exciton relaxation: hyperfine interaction and LA phonon mediated transfers between HH and LH exciton states. The latter mechanism strongly dominates, leading to rates of relaxation typically one order of magnitude faster than the radiative decay. This mechanisms is not observed in epitaxial QDs du to the important splitting between HH and LH states ($\sim 50\ meV$); therefore, lifting the HH-LH near-degeneracy (e.g. with a bi-axial strain) could allow for strongly improving the relaxation rate of excitons. On the other hand, the rate of relaxation mediated by hyperfine interaction is comparable to that observed in QDs (typically ~ 10 ns). In a work realized in parallel to that reported in this thesis, it was establish that the dephasing time (T_2^*) of excitons bound to N dyads in GaAs corresponds to ~ 115 ps [74].

8.1.3 Spin qubits bound to Te dyads in ZnSe

Optical coupling requirement

The spontaneous emission of trions bound to Te dyads in ZnSe is estimated to be faster than 50 ps, as our determination was limited by the temporal resolution of our detector. This is one of the key aspect that has allowed to achieve initialization with near-unity fidelities, as

no spin-flip are expected on such short timescales. It would however be very interesting to evaluate exactly the rate of radiative decay; preliminary works on the exciton have revealed, using resonantly driven Rabi oscillations similar as in Ref. [74], that the lifetime of excitons bound to Te dyads might be as low as 10 ps.

Scalability requirement

The inhomogeneous broadening of Te dyads is more important than both previous systems, but is hard to estimate because the emission from different dyad configurations overlap. The inhomogeneity is attributed to the presence of defects in the host and could be mitigated by improving the growth techniques; highly homogeneous emission characteristic of atomic-size defects is expected for high quality ZnSe hosts.

Coherence requirement

Although decoherence mechanisms were not studied in this work, they are expected to be less important than in previous systems, because (1) contrary to excitons, coherence of spin states is not limited by their radiative decay, (2) most isotopes of Zn, Se, and Te present vanishing nuclear spins, and (3) hyperfine interaction is strongly quenched for hole-spins. It would be however very interesting, in future works to evaluate precisely the rate of relaxation and dephasing associated to these hole-spin qubits, to establish a basis of comparison with QDs and nV centers.

8.1.4 Summary of the different qubits performances

A summary of the physical properties describing each of these requirements, radiative lifetime for optical coupling, inhomogeneous broadening for scalability, and relaxation and dephasing (not measured in this thesis) times for coherence (T_1 and T_2^*, respectively), is presented in Table 8.1 for all ICs studied in this work; exciton and spin qubits in QDs and spin qubits bound to NV centers are also presented to offer a basis of comparison.

8.2 Outlook

Although significant advances were realized for understanding the dynamics of exciton qubits bound to ICs, it appears in light of this work that the most promising IC system for realizing optically addressable qubits are hole-spins bound to Te dyads. Firstly, the coherence time of spin qubits is not limited by their spontaneous emission; furthermore, hole-spin in a nuclear spin-free semiconductor host should lead to long coherence and relaxation times. Consequently, the following steps of the work presented in this thesis consist, in my opinion,

Table 8.1 Summary of the different systems considered for hosting optically addressable qubits in this thesis and in most studied platforms in the literature (self-assembled quantum dots and NV centers). * indicates values taken at room temperature, N/A indicates a value that is still lacking.

System	Type of qubit	Radiative time (ns)	Inhomogeneous broad. (meV)	Relaxation time T_1 (ns)	Dephasing time T_2^* (ns)
N in GaP	Exciton	100-500	< 0.05	0.5	N/A
N in GaAs	Exciton	0.2-0.7	~ 0.1	< 0.5 (LA) ~ 10 ns (hyp.)	0.1 [74]
Te ZnSe	Hole-spin	< 0.05	~ 1	N/A	N/A
InAs QDs	Exciton	0.5-1.0 [57]	~ 50 [65]	20 [152]	0.04 [57]
InAs QDs	Spin (e^-) (h)	0.5-1.0 [58]	~ 50 [65]	20 [152] >1e5 [61]	10 [59] 100 [134]
NV centers	Spin	10 ns [69]	~ 0.1 [66]	$\sim$ ms*[209]	$\sim$ ms* [66]

to further evaluate the potential of these hole-spin qubits. The most important aspects regarding this task are the following.

1- Evaluating the rates of radiative decay, relaxation and dephasing

The initialization of hole-spins that was demonstrated in this thesis presents very interesting fidelity and initialization time. Significant informations are however still lacking to clearly evaluate the potential of this system for building efficient optically addressable qubits, and further efforts should be devoted to identify the rates of radiative decay, relaxation and dephasing.

Investigations of these important characteristics have been initiated recently. Firstly, clear identification of radiative decay rate are expected to be determined through resonantly driven Rabi oscillations between the hole and trion states, similarly to that of Ref. [74]. Secondly, the rate of hole-spin relaxation could be evaluated through pump-probe measurements, where the pump initializes the spin and the probe (controlled with an adjustable delay line) reads-out its state after a precise time delay, such as in Ref. [61]. Relaxation could also be evaluated through the rate of nuclear polarization induced by the hyperfine interaction, as in Ref. [134, 210]. Finally, dephasing rates could be evaluated by measuring the visibility of the quantum interference in a coherence population trapping experiment, similarly as was

realized for a hole-spin confined in a QD (Ref. [196]). It could as well be evaluated through time-resolved pump-probe Kerr rotation in ensemble measurements, as in Ref. [193].

2- Optical control and single-shot readout of the spin state

The next important step toward the realization of IC-based optically addressable qubits is to demonstrate coherent control and single-shot readout of the spin state. Although single-shot readout could be realized without important complications by resonantly scattering light on either of the uncoupled trion transitions (see Ref. [53]), the realization of optical control appears challenging. Indeed previous schemes used for optically controlling spin qubits in QDs require a Λ level configuration [53], e.g. using a magnetic field in Voigt configuration, which is not compatible with the uncoupled trion transitions required for the single-shot readout. However, due to the strong similarity between ICs and QDs, the recent efforts devoted to allow control and read-out of spin qubits in QDs under the same magnetic field configuration [211–215] could be applied to spin qubits bound to ICs.

REFERENCES

[1] J. P. Dowling and G. J. Milburn, "Quantum technology: the second quantum revolution." *Philosophical transactions. Series A, Mathematical, physical, and engineering sciences*, vol. 361, no. 1809, pp. 1655–74, aug 2003. [Online]. Available: http://www.ncbi.nlm.nih.gov/pubmed/12952679

[2] R. P. Feynman, "Simulating physics with computers," *International Journal of Theoretical Physics*, vol. 21, no. 6-7, pp. 467–488, jun 1982. [Online]. Available: http://link.springer.com/10.1007/BF02650179

[3] D. Deutsch, "Quantum Theory, the Church-Turing Principle and the Universal Quantum Computer," *Proceedings of the Royal Society A: Mathematical, Physical and Engineering Sciences*, vol. 400, no. 1818, pp. 97–117, jul 1985. [Online]. Available: http://rspa.royalsocietypublishing.org/cgi/doi/10.1098/rspa.1985.0070

[4] C. H. Bennett and G. Brassard, "Quantum cryptography : Public key distribution and coin tossing," *International Conference on Computer System and Signal Processing, IEEE, 1984*, pp. 175–179, 1984.

[5] A. K. Ekert, "Quantum cryptography based on Bell's theorem," *Physical Review Letters*, vol. 67, no. 6, pp. 661–663, aug 1991. [Online]. Available: http://link.aps.org/doi/10.1103/PhysRevLett.67.661

[6] C. H. Bennett, G. Brassard, and N. D. Mermin, "Quantum cryptography without Bell's theorem," *Physical Review Letters*, vol. 68, no. 5, pp. 557–559, feb 1992. [Online]. Available: http://link.aps.org/doi/10.1103/PhysRevLett.68.557

[7] P. Shor, "Algorithms for quantum computation: discrete logarithms and factoring," in *Proceedings 35th Annual Symposium on Foundations of Computer Science*. IEEE Comput. Soc. Press, 1994, pp. 124–134. [Online]. Available: http://ieeexplore.ieee.org/lpdocs/epic03/wrapper.htm?arnumber=365700

[8] L. K. Grover, "From Schrodinger's equation to the quantum search algorithm," *American Journal of Physics*, vol. 69, no. 7, p. 769, 2001. [Online]. Available: http://link.aip.org/link/AJPIAS/v69/i7/p769/s1{&}Agg=doi

[9] R. Ursin, F. Tiefenbacher, T. Schmitt-Manderbach, H. Weier, T. Scheidl, M. Lindenthal, B. Blauensteiner, T. Jennewein, J. Perdigues, P. Trojek,

B. Ömer, M. Fürst, M. Meyenburg, J. Rarity, Z. Sodnik, C. Barbieri, H. Weinfurter, and A. Zeilinger, "Entanglement-based quantum communication," *Nature Physics*, vol. 3, no. 7, pp. 481–486, jul 2007. [Online]. Available: http://www.nature.com/doifinder/10.1038/nphys629

[10] H. Takesue, S. W. Nam, Q. Zhang, R. H. Hadfield, T. Honjo, K. Tamaki, and Y. Yamamoto, "Quantum key distribution over a 40-dB channel loss using superconducting single-photon detectors," *Nature Photonics*, vol. 1, no. 6, pp. 343–348, jun 2007. [Online]. Available: http://www.nature.com/doifinder/10.1038/nphoton.2007.75

[11] M. Sasaki, M. Fujiwara, H. Ishizuka, W. Klaus, K. Wakui, M. Takeoka, S. Miki, T. Yamashita, Z. Wang, A. Tanaka, K. Yoshino, Y. Nambu, S. Takahashi, A. Tajima, A. Tomita, T. Domeki, T. Hasegawa, Y. Sakai, H. Kobayashi, T. Asai, K. Shimizu, T. Tokura, T. Tsurumaru, M. Matsui, T. Honjo, K. Tamaki, H. Takesue, Y. Tokura, J. F. Dynes, A. R. Dixon, A. W. Sharpe, Z. L. Yuan, A. J. Shields, S. Uchikoga, M. Legré, S. Robyr, P. Trinkler, L. Monat, J.-B. Page, G. Ribordy, A. Poppe, A. Allacher, O. Maurhart, T. Länger, M. Peev, and A. Zeilinger, "Field test of quantum key distribution in the Tokyo QKD Network," *Optics Express*, vol. 19, no. 11, p. 10387, may 2011. [Online]. Available: https://www.osapublishing.org/oe/abstract.cfm?uri=oe-19-11-10387

[12] D. Stucki, M. Legré, F. Buntschu, B. Clausen, N. Felber, N. Gisin, L. Henzen, P. Junod, G. Litzistorf, P. Monbaron, L. Monat, J.-B. Page, D. Perroud, G. Ribordy, A. Rochas, S. Robyr, J. Tavares, R. Thew, P. Trinkler, S. Ventura, R. Voirol, N. Walenta, and H. Zbinden, "Long-term performance of the SwissQuantum quantum key distribution network in a field environment," *New Journal of Physics*, vol. 13, no. 12, p. 123001, dec 2011. [Online]. Available: http://stacks.iop.org/1367-2630/13/i=12/a=123001?key=crossref.a235003f0675cccfadb4b93b7ed7e72b

[13] I. L. Chuang, N. Gershenfeld, and M. Kubinec, "Experimental Implementation of Fast Quantum Searching," *Physical Review Letters*, vol. 80, no. 15, pp. 3408–3411, apr 1998. [Online]. Available: http://link.aps.org/doi/10.1103/PhysRevLett.80.3408

[14] L. M. K. Vandersypen, M. Steffen, G. Breyta, C. S. Yannoni, M. H. Sherwood, and I. L. Chuang, "Experimental realization of Shor's quantum factoring algorithm using nuclear magnetic resonance," *Nature*, vol. 414, no. 6866, pp. 883–887, dec 2001. [Online]. Available: http://www.nature.com/doifinder/10.1038/414883a

[15] E. Martín-López, A. Laing, T. Lawson, R. Alvarez, X.-Q. Zhou, and J. L. O'Brien, "Experimental realization of Shor's quantum factoring algorithm using qubit recycling," *Nature Photonics*, vol. 6, no. 11, pp. 773–776, oct 2012. [Online]. Available: http://www.nature.com/doifinder/10.1038/nphoton.2012.259

[16] I. Georgescu, S. Ashhab, and F. Nori, "Quantum simulation," *Reviews of Modern Physics*, vol. 86, no. 1, pp. 153–185, mar 2014. [Online]. Available: http://link.aps.org/doi/10.1103/RevModPhys.86.153

[17] E. A. Martinez, C. A. Muschik, P. Schindler, D. Nigg, A. Erhard, M. Heyl, P. Hauke, M. Dalmonte, T. Monz, P. Zoller, and R. Blatt, "Real-time dynamics of lattice gauge theories with a few-qubit quantum computer," *Nature*, vol. 534, no. 7608, p. 516, 2016.

[18] M. Zhong, M. P. Hedges, R. L. Ahlefeldt, J. G. Bartholomew, S. E. Beavan, S. M. Wittig, J. J. Longdell, and M. J. Sellars, "Optically addressable nuclear spins in a solid with a six-hour coherence time," *Nature*, vol. 517, no. 7533, pp. 177–180, jan 2015. [Online]. Available: http://www.nature.com/doifinder/10.1038/nature14025

[19] K. Saeedi, S. Simmons, J. Z. Salvail, P. Dluhy, H. Riemann, N. V. Abrosimov, P. Becker, H.-J. Pohl, J. J. L. Morton, and M. L. W. Thewalt, "Room-temperature quantum bit storage exceeding 39 minutes using ionized donors in silicon-28." *Science (New York, N.Y.)*, vol. 342, no. 6160, pp. 830–3, nov 2013. [Online]. Available: http://www.ncbi.nlm.nih.gov/pubmed/24233718

[20] H. J. Kimble, "The quantum internet." *Nature*, vol. 453, no. 7198, pp. 1023–30, jun 2008. [Online]. Available: http://dx.doi.org/10.1038/nature07127

[21] A. Reiserer and G. Rempe, "Cavity-based quantum networks with single atoms and optical photons," *Reviews of Modern Physics*, vol. 87, no. 4, pp. 1379–1418, dec 2015. [Online]. Available: http://link.aps.org/doi/10.1103/RevModPhys.87.1379

[22] S. Ritter, C. Nölleke, C. Hahn, A. Reiserer, A. Neuzner, M. Uphoff, M. Mücke, E. Figueroa, J. Bochmann, and G. Rempe, "An elementary quantum network of single atoms in optical cavities," *Nature*, vol. 484, no. 7393, pp. 195–200, apr 2012. [Online]. Available: http://www.nature.com/doifinder/10.1038/nature11023

[23] T. E. Northup and R. Blatt, "Quantum information transfer using photons," *Nature Photonics*, vol. 8, no. 5, pp. 356–363, apr 2014. [Online]. Available: http://www.nature.com/doifinder/10.1038/nphoton.2014.53

[24] N. Gisin, G. Ribordy, W. Tittel, and H. Zbinden, "Quantum cryptography," *Reviews of Modern Physics*, vol. 74, no. 1, pp. 145–195, mar 2002. [Online]. Available: http://link.aps.org/doi/10.1103/RevModPhys.74.145

[25] B. Hensen, H. Bernien, A. E. Dréau, A. Reiserer, N. Kalb, M. S. Blok, J. Ruitenberg, R. F. L. Vermeulen, R. N. Schouten, C. Abellán, W. Amaya, V. Pruneri, M. W. Mitchell, M. Markham, D. J. Twitchen, D. Elkouss, S. Wehner, T. H. Taminiau, and R. Hanson, "Loophole-free Bell inequality violation using electron spins separated by 1.3 kilometres," *Nature*, vol. 526, no. 7575, pp. 682–686, oct 2015. [Online]. Available: http://www.nature.com/doifinder/10.1038/nature15759

[26] N. Gisin and R. Thew, "Quantum communication," *Nature Photonics*, vol. 1, no. 3, pp. 165–171, mar 2007. [Online]. Available: http://www.nature.com/doifinder/10.1038/nphoton.2007.22

[27] N. Sangouard, C. Simon, H. de Riedmatten, and N. Gisin, "Quantum repeaters based on atomic ensembles and linear optics," *Reviews of Modern Physics*, vol. 83, no. 1, pp. 33–80, mar 2011. [Online]. Available: http://link.aps.org/doi/10.1103/RevModPhys.83.33

[28] C. H. Bennett, G. Brassard, C. Crépeau, R. Jozsa, A. Peres, and W. K. Wootters, "Teleporting an unknown quantum state via dual classical and Einstein-Podolsky-Rosen channels," *Physical Review Letters*, vol. 70, no. 13, pp. 1895–1899, mar 1993. [Online]. Available: http://link.aps.org/doi/10.1103/PhysRevLett.70.1895

[29] C. H. Bennett, G. Brassard, S. Popescu, B. Schumacher, J. A. Smolin, and W. K. Wootters, "Purification of Noisy Entanglement and Faithful Teleportation via Noisy Channels," *Physical Review Letters*, vol. 76, no. 5, pp. 722–725, jan 1996. [Online]. Available: http://link.aps.org/doi/10.1103/PhysRevLett.76.722

[30] S. J. Devitt, W. J. Munro, and K. Nemoto, "Quantum error correction for beginners," *Reports on Progress in Physics*, vol. 76, no. 7, p. 076001, jul 2013. [Online]. Available: http://stacks.iop.org/0034-4885/76/i=7/a=076001?key=crossref.f1cb2368d1d065d6c0ef4d24dab3372c

[31] B. M. Terhal, "Quantum error correction for quantum memories," *Reviews of Modern Physics*, vol. 87, no. 2, pp. 307–346, apr 2015. [Online]. Available: http://link.aps.org/doi/10.1103/RevModPhys.87.307

[32] L. Chirolli and G. Burkard, "Decoherence in solid-state qubits," *Advances in Physics*, vol. 57, no. 3, pp. 225–285, may 2008. [Online]. Available: http://www.tandfonline.com/doi/abs/10.1080/00018730802218067

[33] B. Lounis and M. Orrit, "Single-photon sources," *Reports on Progress in Physics*, vol. 68, no. 5, pp. 1129–1179, may 2005. [Online]. Available: http://stacks.iop.org/0034-4885/68/i=5/a=R04?key=crossref.a93d907e49621855b101f96e0a36e3d6

[34] A. Nicolas, L. Veissier, L. Giner, E. Giacobino, D. Maxein, and J. Laurat, "A quantum memory for orbital angular momentum photonic qubits," *Nature Photonics*, vol. 8, no. 3, pp. 234–238, jan 2014. [Online]. Available: http://www.nature.com/doifinder/10.1038/nphoton.2013.355

[35] P. C. Humphreys, B. J. Metcalf, J. B. Spring, M. Moore, X.-M. Jin, M. Barbieri, W. S. Kolthammer, and I. A. Walmsley, "Linear Optical Quantum Computing in a Single Spatial Mode," *Physical Review Letters*, vol. 111, no. 15, p. 150501, oct 2013. [Online]. Available: http://link.aps.org/doi/10.1103/PhysRevLett.111.150501

[36] J.-C. Boileau, R. Laflamme, M. Laforest, and C. Myers, "Robust Quantum Communication Using a Polarization-Entangled Photon Pair," *Physical Review Letters*, vol. 93, no. 22, p. 220501, nov 2004. [Online]. Available: http://link.aps.org/doi/10.1103/PhysRevLett.93.220501

[37] M. Aspelmeyer, T. Jennewein, M. Pfennigbauer, W. Leeb, and A. Zeilinger, "Long-distance quantum communication with entangled photons using satellites," *IEEE Journal of Selected Topics in Quantum Electronics*, vol. 9, no. 6, pp. 1541–1551, nov 2003. [Online]. Available: http://ieeexplore.ieee.org/lpdocs/epic03/wrapper.htm?arnumber=1263786

[38] J. Jin, E. Saglamyurek, M. l. G. Puigibert, V. Verma, F. Marsili, S. W. Nam, D. Oblak, and W. Tittel, "Telecom-Wavelength Atomic Quantum Memory in Optical Fiber for Heralded Polarization Qubits," *Physical Review Letters*, vol. 115, no. 14, p. 140501, sep 2015. [Online]. Available: http://link.aps.org/doi/10.1103/PhysRevLett.115.140501

[39] K. De Greve, L. Yu, P. L. McMahon, J. S. Pelc, C. M. Natarajan, N. Y. Kim, E. Abe, S. Maier, C. Schneider, M. Kamp, S. Höfling, R. H. Hadfield, A. Forchel, M. M. Fejer, and Y. Yamamoto, "Quantum-dot spin–photon entanglement via frequency downconversion to telecom wavelength," *Nature*, vol. 491, no. 7424, pp. 421–425, nov 2012. [Online]. Available: http://www.nature.com/doifinder/10.1038/nature11577

[40] T. D. Ladd, F. Jelezko, R. Laflamme, Y. Nakamura, C. Monroe, and J. L. O'Brien, "Quantum computers." *Nature*, vol. 464, no. 7285, pp. 45–53, mar 2010. [Online]. Available: http://dx.doi.org/10.1038/nature08812

[41] R. Hanson, L. P. Kouwenhoven, J. R. Petta, S. Tarucha, and L. M. K. Vandersypen, "Spins in few-electron quantum dots," *Reviews of Modern Physics*, vol. 79, no. 4, pp. 1217–1265, oct 2007. [Online]. Available: http://link.aps.org/doi/10.1103/RevModPhys.79.1217

[42] J. M. Elzerman, R. Hanson, L. H. Willems van Beveren, B. Witkamp, L. M. K. Vandersypen, and L. P. Kouwenhoven, "Single-shot read-out of an individual electron spin in a quantum dot," *Nature*, vol. 430, no. 6998, pp. 431–435, jul 2004. [Online]. Available: http://www.nature.com/doifinder/10.1038/nature02693

[43] G. Éthier-Majcher, P. St-Jean, and S. Francoeur, "Light- and heavy-hole trions bound to isoelectronic centers," *Physical Review B*, vol. 92, no. 15, p. 155436, oct 2015. [Online]. Available: http://journals.aps.org/prb/abstract/10.1103/PhysRevB.92.155436

[44] K. J. Vahala, "Optical microcavities," *Nature*, vol. 424, no. 6950, pp. 839–846, aug 2003. [Online]. Available: http://www.nature.com/doifinder/10.1038/nature01939

[45] A. Imamoglu, D. D. Awschalom, G. Burkard, D. P. DiVincenzo, D. Loss, M. Sherwin, and A. Small, "Quantum Information Processing Using Quantum Dot Spins and Cavity QED," *Physical Review Letters*, vol. 83, no. 20, pp. 4204–4207, nov 1999. [Online]. Available: http://journals.aps.org/prl/abstract/10.1103/PhysRevLett.83.4204

[46] J. L. O'Brien, A. Furusawa, and J. Vučković, "Photonic quantum technologies," *Nature Photonics*, vol. 3, no. 12, pp. 687–695, dec 2009. [Online]. Available: http://www.nature.com/doifinder/10.1038/nphoton.2009.229

[47] K. Singer, U. Poschinger, M. Murphy, P. Ivanov, F. Ziesel, T. Calarco, and F. Schmidt-Kaler, "Colloquium : Trapped ions as quantum bits: Essential numerical tools," *Reviews of Modern Physics*, vol. 82, no. 3, pp. 2609–2632, sep 2010. [Online]. Available: http://link.aps.org/doi/10.1103/RevModPhys.82.2609

[48] D. L. Moehring, P. Maunz, S. Olmschenk, K. C. Younge, D. N. Matsukevich, L.-M. Duan, and C. Monroe, "Entanglement of single-atom quantum bits at a distance," *Nature*, vol. 449, no. 7158, pp. 68–71, sep 2007. [Online]. Available: http://www.nature.com/doifinder/10.1038/nature06118

[49] B. B. Blinov, D. L. Moehring, L.-M. Duan, and C. Monroe, "Observation of entanglement between a single trapped atom and a single photon," *Nature*, vol. 428, no. 6979, pp. 153–157, mar 2004. [Online]. Available: http://www.nature.com/doifinder/10.1038/nature02377

[50] A. Stute, B. Casabone, P. Schindler, T. Monz, P. O. Schmidt, B. Brandstätter, T. E. Northup, and R. Blatt, "Tunable ion–photon entanglement in an optical cavity," *Nature*, vol. 485, no. 7399, pp. 482–485, may 2012. [Online]. Available: http://www.nature.com/doifinder/10.1038/nature11120

[51] C. Langer, R. Ozeri, J. Jost, J. Chiaverini, B. DeMarco, A. Ben-Kish, R. Blakestad, J. Britton, D. Hume, W. Itano, D. Leibfried, R. Reichle, T. Rosenband, T. Schaetz, P. Schmidt, and D. Wineland, "Long-Lived Qubit Memory Using Atomic Ions," *Physical Review Letters*, vol. 95, no. 6, p. 060502, aug 2005. [Online]. Available: http://link.aps.org/doi/10.1103/PhysRevLett.95.060502

[52] M. Bayer, O. Stern, P. Hawrylak, S. Fafard, and A. Forchel, "Hidden symmetries in the energy levels of excitonic artificial atoms," *Nature*, vol. 405, no. 6789, pp. 923–926, jun 2000. [Online]. Available: http://www.nature.com/doifinder/10.1038/35016020

[53] R. J. Warburton, "Single spins in self-assembled quantum dots." *Nature materials*, vol. 12, no. 6, pp. 483–93, jun 2013. [Online]. Available: http://dx.doi.org/10.1038/nmat3585

[54] D. Gammon, E. Snow, B. Shanabrook, D. Katzer, and D. Park, "Fine structure splitting in the optical spectra of single GaAs quantum dots." *Physical review letters*, vol. 76, no. 16, pp. 3005–3008, apr 1996. [Online]. Available: http://journals.aps.org/prl/abstract/10.1103/PhysRevLett.76.3005

[55] M. V. G. Dutt, J. Cheng, B. Li, X. Xu, X. Li, P. R. Berman, D. G. Steel, A. S. Bracker, D. Gammon, S. E. Economou, R.-B. Liu, and L. J. Sham, "Stimulated and Spontaneous Optical Generation of Electron Spin Coherence in Charged GaAs Quantum Dots," *Physical Review Letters*, vol. 94, no. 22, p. 227403, jun 2005. [Online]. Available: http://link.aps.org/doi/10.1103/PhysRevLett.94.227403

[56] P. Lodahl, S. Mahmoodian, and S. Stobbe, "Interfacing single photons and single quantum dots with photonic nanostructures," *Reviews of Modern Physics*, vol. 87, no. 2, pp. 347–400, may 2015. [Online]. Available: http://link.aps.org/doi/10.1103/RevModPhys.87.347

[57] N. H. Bonadeo, J. Erland, D. Gammon, D. Park, D. S. Katzer, and D. G. Steel, "Coherent optical control of the quantum state of a single quantum Dot," *Science (New York, N.Y.)*, vol. 282, no. 5393, pp. 1473–6, nov 1998. [Online]. Available: http://www.ncbi.nlm.nih.gov/pubmed/9822374

[58] D. Press, T. D. Ladd, B. Zhang, and Y. Yamamoto, "Complete quantum control of a single quantum dot spin using ultrafast optical pulses." *Nature*, vol. 456, no. 7219, pp. 218–21, nov 2008. [Online]. Available: http://dx.doi.org/10.1038/nature07530

[59] D. Press, K. De Greve, P. L. McMahon, T. D. Ladd, B. Friess, C. Schneider, M. Kamp, S. Höfling, A. Forchel, and Y. Yamamoto, "Ultrafast optical spin echo in a single quantum dot," *Nature Photonics*, vol. 4, no. 6, pp. 367–370, jun 2010. [Online]. Available: http://www.nature.com/doifinder/10.1038/nphoton.2010.83

[60] W. B. Gao, A. Imamoglu, H. Bernien, and R. Hanson, "Coherent manipulation, measurement and entanglement of individual solid-state spins using optical fields," *Nature Photonics*, vol. 9, no. 6, pp. 363–373, may 2015. [Online]. Available: http://www.nature.com/doifinder/10.1038/nphoton.2015.58

[61] B. D. Gerardot, D. Brunner, P. A. Dalgarno, P. Ohberg, S. Seidl, M. Kroner, K. Karrai, N. G. Stoltz, P. M. Petroff, and R. J. Warburton, "Optical pumping of a single hole spin in a quantum dot." *Nature*, vol. 451, no. 7177, pp. 441–4, jan 2008. [Online]. Available: http://dx.doi.org/10.1038/nature06472

[62] K. De Greve, P. L. McMahon, D. Press, T. D. Ladd, D. Bisping, C. Schneider, M. Kamp, L. Worschech, S. Höfling, A. Forchel, and Y. Yamamoto, "Ultrafast coherent control and suppressed nuclear feedback of a single quantum dot hole qubit," *Nature Physics*, vol. 7, no. 11, pp. 872–878, aug 2011. [Online]. Available: http://www.nature.com/nphys/journal/v7/n11/pdf/nphys2078.pdf

[63] T. M. Godden, J. H. Quilter, A. J. Ramsay, Y. Wu, P. Brereton, S. J. Boyle, I. J. Luxmoore, J. Puebla-Nunez, A. M. Fox, and M. S. Skolnick, "Coherent Optical Control of the Spin of a Single Hole in an InAs/GaAs Quantum Dot," *Physical Review Letters*, vol. 108, no. 1, p. 017402, jan 2012. [Online]. Available: http://link.aps.org/doi/10.1103/PhysRevLett.108.017402

[64] A. Delteil, Z. Sun, W.-b. Gao, E. Togan, S. Faelt, and A. Imamoglu, "Generation of heralded entanglement between distant hole spins," *Nature Physics*, vol. 12, no. 3, pp. 218–223, dec 2015. [Online]. Available: http://www.nature.com/doifinder/10.1038/nphys3605

[65] D. Gammon, E. S. Snow, B. V. Shanabrook, D. S. Katzer, and D. Park, "Homogeneous Linewidths in the Optical Spectrum of a Single Gallium Arsenide Quantum Dot," *Science (New York, N.Y.)*, vol. 273, no. 5271, pp. 87–90, jul 1996. [Online]. Available: http://www.ncbi.nlm.nih.gov/pubmed/8688056

[66] L. Childress and R. Hanson, "Diamond NV centers for quantum computing and quantum networks," *MRS Bulletin*, vol. 38, no. 02, pp. 134–138, feb 2013. [Online]. Available: http://www.journals.cambridge.org/abstract{_}S0883769413000201

[67] F. Jelezko and J. Wrachtrup, "Single defect centres in diamond: A review," *physica status solidi (a)*, vol. 203, no. 13, pp. 3207–3225, oct 2006. [Online]. Available: http://doi.wiley.com/10.1002/pssa.200671403

[68] I. Aharonovich, S. Castelletto, D. A. Simpson, C.-H. Su, A. D. Greentree, and S. Prawer, "Diamond-based single-photon emitters," *Reports on Progress in Physics*, vol. 74, no. 7, p. 076501, jul 2011. [Online]. Available: http://stacks.iop.org/0034-4885/74/i=7/a=076501?key=crossref.de26298a109e3a23e095d261d1e2f211

[69] E. Togan, Y. Chu, A. S. Trifonov, L. Jiang, J. Maze, L. Childress, M. V. G. Dutt, A. S. Sørensen, P. R. Hemmer, A. S. Zibrov, and M. D. Lukin, "Quantum entanglement between an optical photon and a solid-state spin qubit," *Nature*, vol. 466, no. 7307, pp. 730–734, aug 2010. [Online]. Available: http://www.nature.com/doifinder/10.1038/nature09256

[70] A. Faraon, C. Santori, Z. Huang, V. M. Acosta, and R. G. Beausoleil, "Coupling of Nitrogen-Vacancy Centers to Photonic Crystal Cavities in Monocrystalline Diamond," *Physical Review Letters*, vol. 109, no. 3, p. 033604, jul 2012. [Online]. Available: http://journals.aps.org/prl/abstract/10.1103/PhysRevLett.109.033604

[71] I. Aharonovich and M. Toth, "Optical materials: Silicon carbide goes quantum," *Nature Physics*, vol. 10, no. 2, pp. 93–94, jan 2014. [Online]. Available: http://dx.doi.org/10.1038/nphys2858

[72] D. J. Sleiter, K. Sanaka, Y. M. Kim, K. Lischka, A. Pawlis, and Y. Yamamoto, "Optical pumping of a single electron spin bound to a fluorine donor in a ZnSe nanostructure." *Nano letters*, vol. 13, no. 1, pp. 116–20, jan 2013. [Online]. Available: http://dx.doi.org/10.1021/nl303663n

[73] N. Dotti, F. Sarti, S. Bietti, A. Azarov, A. Kuznetsov, F. Biccari, A. Vinattieri, S. Sanguinetti, M. Abbarchi, and M. Gurioli, "Germanium-based quantum emitters

towards a time-reordering entanglement scheme with degenerate exciton and biexciton states," *Physical Review B*, vol. 91, no. 20, p. 205316, may 2015. [Online]. Available: http://journals.aps.org/prb/abstract/10.1103/PhysRevB.91.205316

[74] G. Éthier-Majcher, P. St-Jean, G. Boso, A. Tosi, J. F. Klem, and S. Francoeur, "Complete quantum control of exciton qubits bound to isoelectronic centres." *Nature communications*, vol. 5, p. 3980, jan 2014. [Online]. Available: http://www.nature.com/ncomms/2014/140530/ncomms4980/abs/ncomms4980.html

[75] A. Baldereschi, "Theory of isoelectronic traps," *Journal of Luminescence*, vol. 7, pp. 79–91, jan 1973. [Online]. Available: http://linkinghub.elsevier.com/retrieve/pii/0022231373900604

[76] J. Li and L.-W. Wang, "Energy levels of isoelectronic impurities by large scale LDA calculations," *Physical Review B*, vol. 67, no. 3, p. 033102, jan 2003. [Online]. Available: http://link.aps.org/doi/10.1103/PhysRevB.67.033102

[77] Y. Zhang, A. Mascarenhas, and L.-W. Wang, "Systematic approach to distinguishing a perturbed host state from an impurity state in a supercell calculation for a doped semiconductor: Using GaP:N as an example," *Physical Review B*, vol. 74, no. 4, p. 041201, jul 2006. [Online]. Available: http://link.aps.org/doi/10.1103/PhysRevB.74.041201

[78] J. J. Hopfield, D. G. Thomas, and R. T. Lynch, "Isoelectronic Donors and Acceptors," *Physical Review Letters*, vol. 17, no. 6, pp. 312–315, aug 1966. [Online]. Available: http://link.aps.org/doi/10.1103/PhysRevLett.17.312

[79] D. G. Thomas, J. J. Hopfield, and C. J. Frosch, "Isoelectronic Traps Due to Nitrogen in Gallium Phosphide," *Physical Review Letters*, vol. 15, no. 22, pp. 857–860, nov 1965. [Online]. Available: http://link.aps.org/doi/10.1103/PhysRevLett.15.857

[80] R. Faulkner and P. Dean, "Electronic structure of ground and excited states of isoelectronic traps," *Journal of Luminescence*, vol. 1-2, pp. 552–561, jan 1970. [Online]. Available: http://www.sciencedirect.com/science/article/pii/0022231370900670

[81] J. W. Allen, "Isoelectronic impurities in semiconductors: a survey of binding mechanisms," *Journal of Physics C: Solid State Physics*, vol. 4, no. 14, pp. 1936–1944, oct 1971. [Online]. Available: http://stacks.iop.org/0022-3719/4/i=14/a=008?key=crossref.b7151c22a01b2946c4fb2d9bc43442a1

[82] J. C. Phillips, "Cancelation Theorem for Isoelectronic Impurity Binding Energies," *Physical Review Letters*, vol. 22, no. 7, pp. 285–287, feb 1969. [Online]. Available: http://link.aps.org/doi/10.1103/PhysRevLett.22.285

[83] R. A. Faulkner, "Toward a Theory of Isoelectronic Impurities in Semiconductors," *Physical Review*, vol. 175, no. 3, pp. 991–1009, nov 1968. [Online]. Available: http://link.aps.org/doi/10.1103/PhysRev.175.991

[84] E. Cohen and M. D. Sturge, "Excited states of excitons bound to nitrogen pairs in GaP," *Physical Review B*, vol. 15, no. 2, pp. 1039–1051, 1977. [Online]. Available: http://prb.aps.org/abstract/PRB/v15/i2/p1039{_}1

[85] W. T. Masselink and Y.-C. Chang, "Theory of the Exciton Bound to an Isoelectronic Trap in GaP," *Physical Review Letters*, vol. 51, no. 6, pp. 509–512, aug 1983. [Online]. Available: http://link.aps.org/doi/10.1103/PhysRevLett.51.509

[86] P. R. C. Kent and A. Zunger, "Theory of electronic structure evolution in GaAsN and GaPN alloys," *Physical Review B*, vol. 64, no. 11, pp. 16–20, aug 2001. [Online]. Available: http://link.aps.org/doi/10.1103/PhysRevB.64.115208

[87] S. Marcet, C. Ouellet-Plamondon, G. Éthier-Majcher, P. Saint-Jean, R. André, J. Klem, and S. Francoeur, "Charged excitons and biexcitons bound to isoelectronic centers," *Physical Review B*, vol. 82, no. 23, pp. 1–5, dec 2010. [Online]. Available: http://link.aps.org/doi/10.1103/PhysRevB.82.235311

[88] O. Benson, C. Santori, M. Pelton, and Y. Yamamoto, "Regulated and Entangled Photons from a Single Quantum Dot," *Physical Review Letters*, vol. 84, no. 11, pp. 2513–2516, mar 2000. [Online]. Available: http://link.aps.org/doi/10.1103/PhysRevLett.84.2513

[89] N. Akopian, N. H. Lindner, E. Poem, Y. Berlatzky, J. Avron, D. Gershoni, B. D. Gerardot, and P. M. Petroff, "Entangled Photon Pairs from Semiconductor Quantum Dots," *Physical Review Letters*, vol. 96, no. 13, p. 130501, apr 2006. [Online]. Available: http://link.aps.org/doi/10.1103/PhysRevLett.96.130501

[90] C. Ouellet-Plamondon, S. Marcet, J. Klem, and S. Francoeur, "Excitonic fine structure of out-of-plane nitrogen dyads in GaAs," *Journal of Luminescence*, vol. 131, no. 11, pp. 2339–2341, nov 2011. [Online]. Available: http://www.sciencedirect.com/science/article/pii/S0022231311003097

[91] S. Francoeur and S. Marcet, "Effects of symmetry-breaking perturbations on excitonic states bound to systems of reduced symmetry," *Journal of Applied Physics*, vol. 108, no. 4, p. 043710, 2010. [Online]. Available: http://link.aip.org/link/JAPIAU/v108/i4/p043710/s1{&}Agg=doi

[92] Y. Sakuma, M. Ikezawa, M. Watanabe, and Y. Masumoto, "Isoelectronic nitrogen δ-doping in GaP and single-photon emission from individual nitrogen pairs," *Journal of Crystal Growth*, vol. 310, no. 23, pp. 4790–4794, nov 2008. [Online]. Available: http://linkinghub.elsevier.com/retrieve/pii/S0022024808007239

[93] M. Jo, T. Mano, T. Kuroda, Y. Sakuma, and K. Sakoda, "Visible single-photon emission from a nitrogen impurity center in AlAs," *Applied Physics Letters*, vol. 102, no. 6, p. 062107, 2013. [Online]. Available: http://link.aip.org/link/APPLAB/v102/i6/p062107/s1{&}Agg=doi

[94] H. Sumikura, E. Kuramochi, H. Taniyama, and M. Notomi, "Ultrafast spontaneous emission of copper-doped silicon enhanced by an optical nanocavity." *Scientific reports*, vol. 4, p. 5040, jan 2014. [Online]. Available: http://www.pubmedcentral.nih.gov/articlerender.fcgi?artid=4031467{&}tool=pmcentrez{&}rendertype=abstract

[95] G. Ethier-Majcher, P. St-Jean, A. Bergeron, A.-L. Phaneuf-L'Heureux, S. Roorda, and S. Francoeur, "Photoluminescence from single nitrogen isoelectronic centers in gallium phosphide produced by ion implantation," *Journal of Applied Physics*, vol. 114, no. 3, p. 034307, 2013. [Online]. Available: http://scitation.aip.org/content/aip/journal/jap/114/3/10.1063/1.4815883

[96] D. G. Thomas and J. J. Hopfield, "Isoelectronic traps due to nitrogen in gallium phosphide," *Physical Review*, vol. 313, no. 2, pp. 680–689, 1966. [Online]. Available: http://prola.aps.org/abstract/PR/v150/i2/p680{_}1

[97] B. Gil and J. Camassel, "Local symmetry of nitrogen pairs in GaP," *Physical Review B*, vol. 33, no. 4, pp. 2690–2700, 1986. [Online]. Available: http://prb.aps.org/abstract/PRB/v33/i4/p2690{_}1

[98] B. Gil and H. Mariette, "NN2 trap in GaP: A reexamination," *Physical Review B*, vol. 35, no. 15, pp. 7999–8004, 1987.

[99] P. R. C. Kent and A. Zunger, "Nitrogen pairs, triplets, and clusters in GaAs and GaP," *Applied Physics Letters*, vol. 79, no. 15, p. 2339, 2001. [Online]. Available: http://scitation.aip.org/content/aip/journal/apl/79/15/10.1063/1.1408275

[100] M. Ikezawa, Y. Sakuma, and Y. Masumoto, "Single Photon Emission from Individual Nitrogen Pairs in GaP," *Japanese Journal of Applied Physics*, vol. 46, pp. 871–873, 2007.

[101] M. Ikezawa, Y. Sakuma, M. Watanabe, and Y. Masumoto, "Single NN pair luminescence and single photon generation in nitrogen δ-doped GaP," *Physica Status Solidi (C)*, vol. 6, no. 1, pp. 362–365, jan 2009. [Online]. Available: http://doi.wiley.com/10.1002/pssc.200879830

[102] X. Liu, M.-E. Pistol, and L. Samuelson, "Excitons bound to nitrogen pairs in GaAs," *Physical Review B*, vol. 42, no. 12, pp. 7504–7512, oct 1990. [Online]. Available: http://link.aps.org/doi/10.1103/PhysRevB.42.7504

[103] X. Liu, M.-E. Pistol, L. Samuelson, S. Schwetlick, and W. Seifert, "Nitrogen pair luminescence in GaAs," *Applied Physics Letters*, vol. 56, no. 15, p. 1451, apr 1990. [Online]. Available: http://scitation.aip.org/content/aip/journal/apl/56/15/10.1063/1.102495

[104] S. Francoeur, J. F. Klem, and a. Mascarenhas, "Optical Spectroscopy of Single Impurity Centers in Semiconductors," *Physical Review Letters*, vol. 93, no. 6, pp. 1–4, aug 2004. [Online]. Available: http://link.aps.org/doi/10.1103/PhysRevLett.93.067403

[105] T. Kita and O. Wada, "Bound exciton states of isoelectronic centers in GaAs:N grown by an atomically controlled doping technique," *Physical Review B*, vol. 74, no. 3, p. 035213, jul 2006. [Online]. Available: http://link.aps.org/doi/10.1103/PhysRevB.74.035213

[106] M. Ikezawa, Y. Sakuma, L. Zhang, Y. Sone, T. Mori, T. Hamano, M. Watanabe, K. Sakoda, and Y. Masumoto, "Single-photon generation from a nitrogen impurity center in GaAs," *Applied Physics Letters*, vol. 100, no. 4, p. 042106, jan 2012. [Online]. Available: http://scitation.aip.org/content/aip/journal/apl/100/4/10.1063/1.3679181

[107] Q. Fu, D. Lee, A. V. Nurmikko, L. A. Kolodziejski, and R. L. Gunshor, "Isoelectronic δ doping in a ZnSe superlattice: Tellurium as an efficient hole trap," *Physical Review B*, vol. 39, no. 5, pp. 3173–3177, feb 1989. [Online]. Available: http://journals.aps.org/prb/abstract/10.1103/PhysRevB.39.3173

[108] S. Marcet, R. André, and S. Francoeur, "Excitons bound to Te isoelectronic dyads in ZnSe," *Physical Review B*, vol. 82, no. 23, pp. 1–7, dec 2010. [Online]. Available: http://link.aps.org/doi/10.1103/PhysRevB.82.235309

[109] D. Lee, A. Mysyrowicz, A. V. Nurmikko, and B. J. Fitzpatrick, "Exciton self-trapping in ZnSe-ZnTe alloys," *Physical Review Letters*, vol. 58, no. 14, pp. 1475–1478, apr 1987. [Online]. Available: http://link.aps.org/doi/10.1103/PhysRevLett.58.1475

[110] T. Yao, M. Kato, J. Davies, and H. Tanino, "Photoluminescence of excitons bound at Te isoelectronic traps in ZnSe," *Journal of Crystal Growth*, vol. 86, no. 1-4, pp. 552–557, jan 1988. [Online]. Available: http://linkinghub.elsevier.com/retrieve/pii/002202489090774F

[111] C. Lee, H. Kim, H. Park, C. Chung, and S. Chang, "Luminescence from free and self-trapped excitons in ZnSe1-x Tex," *Journal of Luminescence*, vol. 48-49, pp. 116–120, jan 1991. [Online]. Available: http://linkinghub.elsevier.com/retrieve/pii/002223139190087C

[112] I. L. Kuskovsky, C. Tian, G. F. Neumark, J. E. Spanier, I. P. Herman, W.-C. Lin, S. P. Guo, and M. C. Tamargo, "Optical properties of δ -doped ZnSe:Te grown by molecular beam epitaxy: The role of tellurium," *Physical Review B*, vol. 63, no. 15, p. 155205, mar 2001. [Online]. Available: http://link.aps.org/doi/10.1103/PhysRevB.63.155205

[113] M. Jo, Y. Hayashi, H. Kumano, and I. Suemune, "Exciton-phonon interactions observed in blue emission band in Te-delta-doped ZnSe," *Journal of Applied Physics*, vol. 104, no. 3, p. 033531, aug 2008. [Online]. Available: http://scitation.aip.org/content/aip/journal/jap/104/3/10.1063/1.2966697

[114] J. Schreiber, U. Hilpert, L. Horing, L. Worschech, B. Konig, W. Ossau, A. Waag, and G. Landwehr, "Luminescence Studies on Plastic Stress Relaxation in ZnSe/GaAs(001)," *physica status solidi (b)*, vol. 222, no. 1, pp. 169–177, nov 2000. [Online]. Available: http://doi.wiley.com/10.1002/1521-3951{%}28200011{%}29222{%}3A1{%}3C169{%}3A{%}3AAID-PSSB169{%}3E3.0.CO{%}3B2-E

[115] J. L. Merz, K. Nassau, and J. W. Shiever, "Pair Spectra and the Shallow Acceptors in ZnSe," *Physical Review B*, vol. 8, no. 4, pp. 1444–1452, aug 1973. [Online]. Available: http://link.aps.org/doi/10.1103/PhysRevB.8.1444

[116] J. L. Merz, H. Kukimoto, K. Nassau, and J. W. Shiever, "Optical Properties of Substitutional Donors in ZnSe," *Physical Review B*, vol. 6, no. 2, pp. 545–556, jul 1972. [Online]. Available: http://journals.aps.org/prb/cited-by/10.1103/PhysRevB.6.545

[117] a. Muller, P. Bianucci, C. Piermarocchi, M. Fornari, I. C. Robin, R. André, and C. K. Shih, "Time-resolved photoluminescence spectroscopy of individual Te impurity centers in ZnSe," *Physical Review B*, vol. 73, no. 8, p. 081306, feb 2006. [Online]. Available: http://link.aps.org/doi/10.1103/PhysRevB.73.081306

[118] K. Brunner, G. Abstreiter, G. Böhm, G. Tränkle, and G. Weimann, "Sharp-line photoluminescence and two-photon absorption of zero-dimensional biexcitons in a GaAs/AlGaAs structure." *Physical review letters*, vol. 73, no. 8, pp. 1138–1141, aug 1994. [Online]. Available: http://journals.aps.org/prl/abstract/10.1103/PhysRevLett.73.1138

[119] M. I. Dyakonov, *Spin Physics in Semiconductors*, springer-v ed., Berlin, 2008.

[120] K. Cho, "Unified theory of symmetry-breaking effects on excitons in cubic and wurtzite structures," *Physical Review B*, vol. 14, no. 10, pp. 4463–4482, nov 1976. [Online]. Available: http://link.aps.org/doi/10.1103/PhysRevB.14.4463

[121] B. Honerlage, R. Lévy, J. Grun, C. Klingshirn, and K. Bohnert, "The dispersion of excitons, polaritons and biexcitons in direct-gap semiconductors," *Physics Reports*, vol. 124, no. 3, pp. 161–253, jul 1985. [Online]. Available: http://linkinghub.elsevier.com/retrieve/pii/0370157385900250

[122] M. Bayer, G. Ortner, O. Stern, A. Kuther, A. A. Gorbunov, A. Forchel, P. Hawrylak, S. Fafard, K. Hinzer, T. L. Reinecke, S. N. Walck, J. P. Reithmaier, F. Klopf, and F. Schäfer, "Fine structure of neutral and charged excitons in self-assembled In(Ga)As/(Al)GaAs quantum dots," *Physical Review B*, vol. 65, no. 19, p. 195315, may 2002. [Online]. Available: http://link.aps.org/doi/10.1103/PhysRevB.65.195315

[123] J. v. W. Morgan and T. N. Morgan, "Stress Effects on Excitons Bound to Axially Symmetric Defects in Semiconductors," *Physical Review B*, vol. 1, no. 2, pp. 739–749, jan 1970. [Online]. Available: http://link.aps.org/doi/10.1103/PhysRevB.1.739

[124] P. J. Dean, J. D. Cuthbert, and R. T. Lynch, "Interimpurity Recombinations Involving the Isoelectronic Trap Bismuth in Gallium Phosphide," *Physical Review*, vol. 179, no. 3, pp. 754–763, mar 1969. [Online]. Available: http://journals.aps.org/pr/abstract/10.1103/PhysRev.179.754

[125] P. St-Jean, G. Éthier-Majcher, and S. Francoeur, "Dynamics of excitons bound to nitrogen isoelectronic centers in GaAs," *Physical Review B*, vol. 91, no. 11, p.

115201, mar 2015. [Online]. Available: http://journals.aps.org/prb/abstract/10.1103/PhysRevB.91.115201

[126] Y. J. Fu, S. D. Lin, M. F. Tsai, H. Lin, C. H. Lin, H. Y. Chou, S. J. Cheng, and W. H. Chang, "Anomalous diamagnetic shift for negative trions in single semiconductor quantum dots," *Physical Review B*, vol. 81, no. 11, p. 113307, mar 2010. [Online]. Available: http://journals.aps.org/prb/abstract/10.1103/PhysRevB.81.113307

[127] B. Urbaszek, X. Marie, T. Amand, O. Krebs, P. Voisin, P. Maletinsky, A. Högele, and A. Imamoglu, "Nuclear spin physics in quantum dots: An optical investigation," *Reviews of Modern Physics*, vol. 85, no. 1, pp. 79–133, jan 2013. [Online]. Available: http://link.aps.org/doi/10.1103/RevModPhys.85.79

[128] H. D. Wolf, K. Richter, and C. Weyrich, "On the possibility of stimulated emission in GaP:N," *Solid State Communications*, vol. 15, no. 4, pp. 725–727, 1974.

[129] I. K. Kristensen, "Temperature Dependence of Time Decay of Photoluminescence in GaP:N," *Physica Scripta*, vol. 25, no. 6A, pp. 860–862, jun 1982. [Online]. Available: http://stacks.iop.org/1402-4896/25/i=6A/a=052?key=crossref.33e2ea526aa21ae375f3dff8bf931121

[130] J. Zheng and W. M. Yen, "Luminescence decay of excitons bound to nitrogen pairs in GaP:N," *Journal of luminescence*, vol. 39, no. 5, pp. 233–237, 1988.

[131] H. Dai, M. A. Gundersen, C. W. Myles, and P. G. Snyder, "Phonon-assisted indirect recombination of bound excitons in N-doped GaP, including near-resonant processes," *Physical Review B*, vol. 37, no. 3, pp. 1205–1217, jan 1988. [Online]. Available: http://link.aps.org/doi/10.1103/PhysRevB.37.1205

[132] M. Felici, A. Polimeni, A. Miriametro, M. Capizzi, H. P. Xin, and C. W. Tu, "Free carrier and/or exciton trapping by nitrogen pairs in dilute GaP:N," *Physical Review B*, vol. 71, no. 4, p. 045209, jan 2005. [Online]. Available: http://link.aps.org/doi/10.1103/PhysRevB.71.045209

[133] O. Labeau, P. Tamarat, and B. Lounis, "Temperature Dependence of the Luminescence Lifetime of Single CdSe/ZnS Quantum Dots," *Physical Review Letters*, vol. 90, no. 25, pp. 25–28, jun 2003. [Online]. Available: http://link.aps.org/doi/10.1103/PhysRevLett.90.257404

[134] P. Fallahi, S. T. Yilmaz, and A. Imamoglu, "Measurement of a heavy-hole hyperfine interaction in InGaAs quantum dots using resonance fluorescence."

Physical review letters, vol. 105, no. 25, p. 257402, dec 2010. [Online]. Available: http://journals.aps.org/prl/abstract/10.1103/PhysRevLett.105.257402

[135] W. Coish and D. Loss, "Hyperfine interaction in a quantum dot: Non-Markovian electron spin dynamics," *Physical Review B*, vol. 70, no. 19, p. 195340, nov 2004. [Online]. Available: http://link.aps.org/doi/10.1103/PhysRevB.70.195340

[136] J. Fischer, W. A. Coish, D. V. Bulaev, and D. Loss, "Spin decoherence of a heavy hole coupled to nuclear spins in a quantum dot," *Physical Review B*, vol. 78, no. 15, p. 155329, oct 2008. [Online]. Available: http://link.aps.org/doi/10.1103/PhysRevB.78.155329

[137] I. A. Merkulov, "Electron spin relaxation by nuclei in semiconductor quantum dots," *Physical Review B*, vol. 65, no. 20, p. 205309, apr 2002. [Online]. Available: http://link.aps.org/doi/10.1103/PhysRevB.65.205309

[138] R. Hanson and D. D. Awschalom, "Coherent manipulation of single spins in semiconductors." *Nature*, vol. 453, no. 7198, pp. 1043–9, jun 2008. [Online]. Available: http://dx.doi.org/10.1038/nature07129

[139] A. M. Tyryshkin, S. Tojo, J. J. L. Morton, H. Riemann, N. V. Abrosimov, P. Becker, H.-J. Pohl, T. Schenkel, M. L. W. Thewalt, K. M. Itoh, and S. A. Lyon, "Electron spin coherence exceeding seconds in high-purity silicon." *Nature materials*, vol. 11, no. 2, pp. 143–7, feb 2012. [Online]. Available: http://dx.doi.org/10.1038/nmat3182

[140] B. Eble, C. Testelin, P. Desfonds, F. Bernardot, A. Balocchi, T. Amand, A. Miard, A. Lemaître, X. Marie, and M. Chamarro, "Hole–Nuclear Spin Interaction in Quantum Dots," *Physical Review Letters*, vol. 102, no. 14, p. 146601, apr 2009. [Online]. Available: http://link.aps.org/doi/10.1103/PhysRevLett.102.146601

[141] A. Boyer de la Giroday, N. Sköld, R. M. Stevenson, I. Farrer, D. A. Ritchie, and A. J. Shields, "Exciton-Spin Memory with a Semiconductor Quantum Dot Molecule," *Physical Review Letters*, vol. 106, no. 21, p. 216802, may 2011. [Online]. Available: http://link.aps.org/doi/10.1103/PhysRevLett.106.216802

[142] F. H. L. Koppens, C. Buizert, K. J. Tielrooij, I. T. Vink, K. C. Nowack, T. Meunier, L. P. Kouwenhoven, and L. M. K. Vandersypen, "Driven coherent oscillations of a single electron spin in a quantum dot." *Nature*, vol. 442, no. 7104, pp. 766–71, aug 2006. [Online]. Available: http://www.ncbi.nlm.nih.gov/pubmed/16915280

[143] G. D. Fuchs, G. Burkard, P. V. Klimov, and D. D. Awschalom, "A quantum memory intrinsic to single nitrogen–vacancy centres in diamond," *Nature Physics*, vol. 7, no. 10, p. 789, 2011.

[144] P. C. Maurer, G. Kucsko, C. Latta, L. Jiang, N. Y. Yao, S. D. Bennett, F. Pastawski, D. Hunger, N. Chisholm, M. Markham, D. J. Twitchen, J. I. Cirac, and M. D. Lukin, "Room-Temperature Quantum Bit Memory Exceeding One Second," *Science*, vol. 336, no. 6086, pp. 1283–1286, 2012.

[145] M. Steger, K. Saeedi, M. L. W. Thewalt, J. J. L. Morton, H. Riemann, N. V. Abrosimov, and P. Becker, "Quantum Information Storage for over 180 s Using Donor Spins in a 28Si "Semiconductor Vacuum"," *Science*, vol. 336, p. 1280, 2012.

[146] J. J. Pla, K. Y. Tan, J. P. Dehollain, W. H. Lim, J. J. L. Morton, D. N. Jamieson, A. S. Dzurak, and A. Morello, "A single-atom electron spin qubit in silicon." *Nature*, vol. 489, no. 7417, pp. 541–5, oct 2012. [Online]. Available: http://www.ncbi.nlm.nih.gov/pubmed/22992519

[147] M. D. Pashley, K. W. Haberern, W. Friday, J. M. Woodall, and P. D. Kirchner, "Structure of GaAs(001) (2x4)-c(2x8) Determined by Scanning Tunneling Miscropy," *Physical review letters*, vol. 60, no. 21, p. 1988, 1988.

[148] M. D. Sturge, E. Cohen, and K. F. Rodgers, "Thermal quenching processes in the low temperature photoluminescence to nitrogen pairs in GaP," *Physical Review B*, vol. 15, no. 6, p. 3169, 1977.

[149] P. J. Wiesner, R. A. Street, and H. D. Wolf, "Exciton Energy Transfer in GaP:N," *Physical review letters*, vol. 35, no. 20, pp. 1366–1369, 1975.

[150] P. Hugon and H. Mariette, "Stochastic transfer of excitations and exhancement of the NN_{α}-pair luminescence in GaP: N," *Physical Review B*, vol. 30, no. 3, pp. 1622–1625, aug 1984. [Online]. Available: http://link.aps.org/doi/10.1103/PhysRevB.30.1622

[151] T. Takagahara, "Theory of exciton doublet structures and polarization relaxation in single quantum dots," *Physical Review B*, vol. 62, no. 24, pp. 16 840–16 855, dec 2000. [Online]. Available: http://link.aps.org/doi/10.1103/PhysRevB.62.16840

[152] H. Kurtze, D. R. Yakovlev, D. Reuter, a. D. Wieck, and M. Bayer, "Hyperfine interaction mediated exciton spin relaxation in (In,Ga)As quantum dots,"

Physical Review B, vol. 85, no. 19, p. 195303, may 2012. [Online]. Available: http://link.aps.org/doi/10.1103/PhysRevB.85.195303

[153] E. Tsitsishvili, R. Baltz, and H. Kalt, "Exciton spin relaxation in single semiconductor quantum dots," *Physical Review B*, vol. 67, no. 20, pp. 1–6, may 2003. [Online]. Available: http://link.aps.org/doi/10.1103/PhysRevB.67.205330

[154] E. Tsitsishvili and H. Kalt, "Exciton spin relaxation in strongly confining semiconductor quantum dots," *Physical Review B*, vol. 82, no. 19, p. 195315, nov 2010. [Online]. Available: http://link.aps.org/doi/10.1103/PhysRevB.82.195315

[155] V. N. Golovach, A. Khaetskii, and D. Loss, "Phonon-Induced Decay of the Electron Spin in Quantum Dots," *Physical Review Letters*, vol. 93, no. 1, p. 016601, jun 2004. [Online]. Available: http://link.aps.org/doi/10.1103/PhysRevLett.93.016601

[156] J. Smith, P. Dalgarno, R. Warburton, a. Govorov, K. Karrai, B. Gerardot, and P. Petroff, "Voltage Control of the Spin Dynamics of an Exciton in a Semiconductor Quantum Dot," *Physical Review Letters*, vol. 94, no. 19, p. 197402, may 2005. [Online]. Available: http://link.aps.org/doi/10.1103/PhysRevLett.94.197402

[157] A. Khaetskii and Y. Nazarov, "Spin relaxation in semiconductor quantum dots," *Physical Review B*, vol. 61, no. 19, pp. 12 639–12 642, may 2000. [Online]. Available: http://link.aps.org/doi/10.1103/PhysRevB.61.12639

[158] K. Roszak, V. Axt, T. Kuhn, and P. Machnikowski, "Erratum: Exciton spin decay in quantum dots to bright and dark states [Phys. Rev. B 76, 195324 (2007)]," *Physical Review B*, vol. 77, no. 24, p. 249905, jun 2008. [Online]. Available: http://link.aps.org/doi/10.1103/PhysRevB.77.249905

[159] D. Stepanenko, G. Burkard, G. Giedke, and A. Imamoglu, "Enhancement of Electron Spin Coherence by Optical Preparation of Nuclear Spins," *Physical Review Letters*, vol. 96, no. 13, p. 136401, apr 2006. [Online]. Available: http://link.aps.org/doi/10.1103/PhysRevLett.96.136401

[160] J. Berezovsky, M. H. Mikkelsen, N. G. Stoltz, L. A. Coldren, and D. D. Awschalom, "Picosecond coherent optical manipulation of a single electron spin in a quantum dot." *Science (New York, N.Y.)*, vol. 320, no. 5874, pp. 349–52, apr 2008. [Online]. Available: http://www.sciencemag.org/content/320/5874/349

[161] M. V. G. Dutt, L. Childress, L. Jiang, E. Togan, J. Maze, F. Jelezko, A. S. Zibrov, P. R. Hemmer, and M. D. Lukin, "Quantum register based

on individual electronic and nuclear spin qubits in diamond." *Science (New York, N.Y.)*, vol. 316, no. 5829, pp. 1312–6, jun 2007. [Online]. Available: http://www.sciencemag.org/content/316/5829/1312

[162] Y. G. Zhang, Z. Tang, X. G. Zhao, G. D. Cheng, Y. Tu, W. T. Cong, W. Peng, Z. Q. Zhu, and J. H. Chu, "A neutral oxygen-vacancy center in diamond: A plausible qubit candidate and its spintronic and electronic properties," *Applied Physics Letters*, vol. 105, no. 5, p. 052107, aug 2014. [Online]. Available: http://scitation.aip.org/content/aip/journal/apl/105/5/10.1063/1.4892654

[163] G. Pica, G. Wolfowicz, M. Urdampilleta, M. L. W. Thewalt, H. Riemann, N. V. Abrosimov, P. Becker, H.-J. Pohl, J. J. L. Morton, R. N. Bhatt, S. A. Lyon, and B. W. Lovett, "Hyperfine Stark effect of shallow donors in silicon," *Physical Review B*, vol. 90, no. 19, p. 195204, nov 2014. [Online]. Available: http://link.aps.org/doi/10.1103/PhysRevB.90.195204

[164] F. Sarti, G. Munnoz Matutano, D. Bauer, N. Dotti, S. Bietti, G. Isella, A. Vinattieri, S. Sanguinetti, and M. Gurioli, "Multiexciton complex from extrinsic centers in AlGaAs epilayers on Ge and Si substrates," *Journal of Applied Physics*, vol. 114, no. 22, p. 224314, dec 2013. [Online]. Available: http://scitation.aip.org/content/aip/journal/jap/114/22/10.1063/1.4844375

[165] P. St-Jean, G. Éthier-Majcher, Y. Sakuma, and S. Francoeur, "Recombination dynamics of excitons bound to nitrogen isoelectronic centers in <math><mi>δ</mi></math>-doped GaP," *Physical Review B*, vol. 89, no. 7, p. 075308, feb 2014. [Online]. Available: http://link.aps.org/doi/10.1103/PhysRevB.89.075308

[166] S. Marcet, C. Ouellet-Plamondon, J. F. Klem, and S. Francoeur, "Single nitrogen dyad magnetoluminescence in GaAs," *Physical Review B*, vol. 80, no. 24, p. 245404, dec 2009. [Online]. Available: http://link.aps.org/doi/10.1103/PhysRevB.80.245404

[167] G. Fishman and G. Lampel, "Spin relaxation of photoelectrons in p-type gallium arsenide," *Physical Review B*, vol. 16, no. 2, pp. 820–831, jul 1977. [Online]. Available: http://link.aps.org/doi/10.1103/PhysRevB.16.820

[168] D. Hilton and C. Tang, "Optical Orientation and Femtosecond Relaxation of Spin-Polarized Holes in GaAs," *Physical Review Letters*, vol. 89, no. 14, p. 146601, sep 2002. [Online]. Available: http://link.aps.org/doi/10.1103/PhysRevLett.89.146601

[169] R. Dzhioev, V. Korenev, I. Merkulov, B. Zakharchenya, D. Gammon, A. Efros, and D. Katzer, "Manipulation of the Spin Memory of Electrons in n-GaAs," *Physical Review Letters*, vol. 88, no. 25, p. 256801, jun 2002. [Online]. Available: http://link.aps.org/doi/10.1103/PhysRevLett.88.256801

[170] P.-F. Braun, X. Marie, L. Lombez, B. Urbaszek, T. Amand, P. Renucci, V. Kalevich, K. Kavokin, O. Krebs, P. Voisin, and Y. Masumoto, "Direct Observation of the Electron Spin Relaxation Induced by Nuclei in Quantum Dots," *Physical Review Letters*, vol. 94, no. 11, p. 116601, mar 2005. [Online]. Available: http://link.aps.org/doi/10.1103/PhysRevLett.94.116601

[171] T. Flissikowski, I. Akimov, A. Hundt, and F. Henneberger, "Single-hole spin relaxation in a quantum dot," *Physical Review B*, vol. 68, no. 16, p. 161309, oct 2003. [Online]. Available: http://link.aps.org/doi/10.1103/PhysRevB.68.161309

[172] S. Laurent, B. Eble, O. Krebs, A. Lemaître, B. Urbaszek, X. Marie, T. Amand, and P. Voisin, "Electrical Control of Hole Spin Relaxation in Charge Tunable InAs/GaAs Quantum Dots," *Physical Review Letters*, vol. 94, no. 14, p. 147401, apr 2005. [Online]. Available: http://link.aps.org/doi/10.1103/PhysRevLett.94.147401

[173] D. Heiss, S. Schaeck, H. Huebl, M. Bichler, G. Abstreiter, J. Finley, D. Bulaev, and D. Loss, "Observation of extremely slow hole spin relaxation in self-assembled quantum dots," *Physical Review B*, vol. 76, no. 24, p. 241306, dec 2007. [Online]. Available: http://link.aps.org/doi/10.1103/PhysRevB.76.241306

[174] E. Tsitsishvili, R. v. Baltz, and H. Kalt, "Exciton-spin relaxation in quantum dots due to spin-orbit interaction," *Physical Review B*, vol. 72, no. 15, p. 155333, oct 2005. [Online]. Available: http://link.aps.org/doi/10.1103/PhysRevB.72.155333

[175] D. Bulaev and D. Loss, "Spin Relaxation and Decoherence of Holes in Quantum Dots," *Physical Review Letters*, vol. 95, no. 7, p. 076805, aug 2005. [Online]. Available: http://link.aps.org/doi/10.1103/PhysRevLett.95.076805

[176] M.-F. Tsai, H. Lin, C.-H. Lin, S.-D. Lin, S.-Y. Wang, M.-C. Lo, S.-J. Cheng, M.-C. Lee, and W.-H. Chang, "Diamagnetic response of exciton complexes in semiconductor quantum dots." *Physical review letters*, vol. 101, no. 26, p. 267402, dec 2008. [Online]. Available: http://journals.aps.org/prl/abstract/10.1103/PhysRevLett.101.267402

[177] D. Gammon, A. L. Efros, T. A. Kennedy, M. Rosen, D. S. Katzer, D. Park, V. L. Korenev, and I. A. Merkulov, "Electron and Nuclear Spin

Interactions in the Optical Spectra of Single GaAs Quantum Dots," *Physical Review Letters*, vol. 86, no. 22, pp. 5176–5179, may 2001. [Online]. Available: http://link.aps.org/doi/10.1103/PhysRevLett.86.5176

[178] S. Erlingsson, Y. Nazarov, and V. Fal'ko, "Nucleus-mediated spin-flip transitions in GaAs quantum dots," *Physical Review B*, vol. 64, no. 19, p. 195306, oct 2001. [Online]. Available: http://link.aps.org/doi/10.1103/PhysRevB.64.195306

[179] J. Puebla, E. A. Chekhovich, M. Hopkinson, P. Senellart, A. Lemaitre, M. S. Skolnick, and A. I. Tartakovskii, "Dynamic nuclear polarization in InGaAs/GaAs and GaAs/AlGaAs quantum dots under nonresonant ultralow-power optical excitation," *Physical Review B*, vol. 88, no. 4, p. 045306, jul 2013. [Online]. Available: http://link.aps.org/doi/10.1103/PhysRevB.88.045306

[180] E. A. Chekhovich, A. B. Krysa, M. S. Skolnick, and A. I. Tartakovskii, "Direct Measurement of the Hole-Nuclear Spin Interaction in Single InP/GaInP Quantum Dots Using Photoluminescence Spectroscopy," *Physical Review Letters*, vol. 106, no. 2, p. 027402, jan 2011. [Online]. Available: http://link.aps.org/doi/10.1103/PhysRevLett.106.027402

[181] B. Krummheuer, V. Axt, and T. Kuhn, "Theory of pure dephasing and the resulting absorption line shape in semiconductor quantum dots," *Physical Review B*, vol. 65, no. 19, p. 195313, may 2002. [Online]. Available: http://link.aps.org/doi/10.1103/PhysRevB.65.195313

[182] L. Besombes, K. Kheng, L. Marsal, and H. Mariette, "Acoustic phonon broadening mechanism in single quantum dot emission," *Physical Review B*, vol. 63, no. 15, p. 155307, mar 2001. [Online]. Available: http://link.aps.org/doi/10.1103/PhysRevB.63.155307

[183] U. Bockelmann, "Exciton relaxation and radiative recombination in semiconductor quantum dots," *Physical Review B*, vol. 48, no. 23, pp. 17 637–17 640, dec 1993. [Online]. Available: http://link.aps.org/doi/10.1103/PhysRevB.48.17637

[184] T. Takagahara, "Theory of exciton dephasing in semiconductor quantum dots," *Physical Review B*, vol. 60, no. 4, pp. 2638–2652, jul 1999. [Online]. Available: http://link.aps.org/doi/10.1103/PhysRevB.60.2638

[185] C. Tonin, R. Hostein, V. Voliotis, R. Grousson, A. Lemaitre, and A. Martinez, "Polarization properties of excitonic qubits in single self-assembled quantum dots,"

Physical Review B, vol. 85, no. 15, p. 155303, apr 2012. [Online]. Available: http://link.aps.org/doi/10.1103/PhysRevB.85.155303

[186] I. Favero, G. Cassabois, C. Voisin, C. Delalande, P. Roussignol, R. Ferreira, C. Couteau, J. Poizat, and J. Gérard, "Fast exciton spin relaxation in single quantum dots," *Physical Review B*, vol. 71, no. 23, p. 233304, jun 2005. [Online]. Available: http://link.aps.org/doi/10.1103/PhysRevB.71.233304

[187] J. J. Morton and B. W. Lovett, "Hybrid Solid-State Qubits: The Powerful Role of Electron Spins," *Annual Review of Condensed Matter Physics*, vol. 2, no. 1, pp. 189–212, mar 2011. [Online]. Available: http://arxiv.org/abs/1103.0418$\delimiter"026E30F$nhttp://www.annualreviews.org/doi/abs/10.1146/annurev-conmatphys-062910-140514

[188] D. D. Awschalom, L. C. Bassett, A. S. Dzurak, E. L. Hu, and J. R. Petta, "Quantum spintronics: engineering and manipulating atom-like spins in semiconductors." *Science (New York, N.Y.)*, vol. 339, no. 6124, pp. 1174–9, mar 2013. [Online]. Available: http://www.ncbi.nlm.nih.gov/pubmed/23471400

[189] T. C. Hain, F. Fuchs, V. A. Soltamov, P. G. Baranov, G. V. Astakhov, T. Hertel, and V. Dyakonov, "Excitation and recombination dynamics of vacancy-related spin centers in silicon carbide," *Journal of Applied Physics*, vol. 115, no. 13, p. 133508, apr 2014. [Online]. Available: http://scitation.aip.org/content/aip/journal/jap/115/13/10.1063/1.4870456

[190] J. Weber, H. Bauch, and R. Sauer, "Optical properties of copper in silicon: Excitons bound to isoelectronic copper pairs," *Physical Review B*, vol. 25, no. 12, pp. 7688–7699, jun 1982. [Online]. Available: http://journals.aps.org/prb/abstract/10.1103/PhysRevB.25.7688

[191] T. Damen, L. Via, J. Cunningham, J. Shah, and L. Sham, "Subpicosecond spin relaxation dynamics of excitons and free carriers in GaAs quantum wells." *Physical review letters*, vol. 67, no. 24, pp. 3432–3435, dec 1991. [Online]. Available: http://journals.aps.org/prl/abstract/10.1103/PhysRevLett.67.3432

[192] F. Heisterkamp, E. A. Zhukov, A. Greilich, D. R. Yakovlev, V. L. Korenev, A. Pawlis, and M. Bayer, "Longitudinal and transverse spin dynamics of donor-bound electrons in fluorine-doped ZnSe: Spin inertia versus Hanle effect," *Physical Review B*, vol. 91, no. 23, p. 235432, jun 2015. [Online]. Available: http://journals.aps.org/prb/abstract/10.1103/PhysRevB.91.235432

[193] A. Greilich, A. Pawlis, F. Liu, O. A. Yugov, D. R. Yakovlev, K. Lischka, Y. Yamamoto, and M. Bayer, "Spin dephasing of fluorine-bound electrons in ZnSe," *Physical Review B*, vol. 85, no. 12, p. 121303, mar 2012. [Online]. Available: http://journals.aps.org/prb/abstract/10.1103/PhysRevB.85.121303

[194] X. Zhang, K. Dou, Q. Hong, and M. Balkanski, "Radiative and nonradiative recombination of bound excitons in GaP:N. I. Temperature behavior of zero-phonon line and phonon sidebands of bound excitons," *Physical Review B*, vol. 41, no. 3, pp. 1376–1381, 1990.

[195] X. Xu, B. Sun, P. R. Berman, D. G. Steel, A. S. Bracker, D. Gammon, and L. J. Sham, "Coherent population trapping of an electron spin in a single negatively charged quantum dot," *Nature Physics*, vol. 4, no. 9, pp. 692–695, aug 2008. [Online]. Available: http://dx.doi.org/10.1038/nphys1054

[196] D. Brunner, B. D. Gerardot, P. A. Dalgarno, G. Wüst, K. Karrai, N. G. Stoltz, P. M. Petroff, and R. J. Warburton, "A coherent single-hole spin in a semiconductor." *Science (New York, N.Y.)*, vol. 325, no. 5936, pp. 70–2, jul 2009. [Online]. Available: http://science.sciencemag.org/content/325/5936/70.abstract

[197] M. Kroutvar, Y. Ducommun, D. Heiss, M. Bichler, D. Schuh, G. Abstreiter, and J. J. Finley, "Optically programmable electron spin memory using semiconductor quantum dots." *Nature*, vol. 432, no. 7013, pp. 81–4, nov 2004. [Online]. Available: http://dx.doi.org/10.1038/nature03008

[198] A. J. Brash, L. M. P. P. Martins, F. Liu, J. H. Quilter, A. J. Ramsay, M. S. Skolnick, and A. M. Fox, "High-fidelity initialization of long-lived quantum dot hole spin qubits by reduced fine-structure splitting," *Physical Review B*, vol. 92, no. 12, p. 121301, sep 2015. [Online]. Available: http://journals.aps.org/prb/abstract/10.1103/PhysRevB.92.121301

[199] M. Atatüre, J. Dreiser, A. Badolato, A. Högele, K. Karrai, and A. Imamoglu, "Quantum-dot spin-state preparation with near-unity fidelity." *Science (New York, N.Y.)*, vol. 312, no. 5773, pp. 551–3, apr 2006. [Online]. Available: http://science.sciencemag.org/content/312/5773/551.abstract

[200] C. Emary, X. Xu, D. G. Steel, S. Saikin, and L. J. Sham, "Fast initialization of the spin state of an electron in a quantum dot in the Voigt configuration." *Physical review letters*, vol. 98, no. 4, p. 047401, jan 2007. [Online]. Available: http://journals.aps.org/prl/abstract/10.1103/PhysRevLett.98.047401

[201] X. Xu, Y. Wu, B. Sun, Q. Huang, J. Cheng, D. G. Steel, A. S. Bracker, D. Gammon, C. Emary, and L. J. Sham, "Fast spin state initialization in a singly charged InAs-GaAs quantum dot by optical cooling." *Physical review letters*, vol. 99, no. 9, p. 097401, aug 2007. [Online]. Available: http://journals.aps.org/prl/abstract/10.1103/PhysRevLett.99.097401

[202] J. Preskill, "Reliable quantum computers," *Proceedings of the Royal Society A: Mathematical, Physical and Engineering Sciences*, vol. 454, no. 1969, pp. 385–410, jan 1998. [Online]. Available: http://rspa.royalsocietypublishing.org/content/454/1969/385

[203] F. Fras, B. Eble, P. Desfonds, F. Bernardot, C. Testelin, M. Chamarro, A. Miard, and A. Lemaître, "Hole-spin initialization and relaxation times in InAs/GaAs quantum dots," *Physical Review B*, vol. 84, no. 12, p. 125431, sep 2011. [Online]. Available: http://link.aps.org/doi/10.1103/PhysRevB.84.125431

[204] A. Greilich, S. G. Carter, D. Kim, A. S. Bracker, and D. Gammon, "Optical control of one and two hole spins in interacting quantum dots," *Nature Photonics*, vol. 5, no. 11, pp. 702–708, sep 2011. [Online]. Available: http://www.nature.com/doifinder/10.1038/nphoton.2011.237

[205] C. Santori, P. Tamarat, P. Neumann, J. Wrachtrup, D. Fattal, R. G. Beausoleil, J. Rabeau, P. Olivero, A. D. Greentree, S. Prawer, F. Jelezko, and P. Hemmer, "Coherent Population Trapping of Single Spins in Diamond under Optical Excitation," *Physical Review Letters*, vol. 97, no. 24, p. 247401, dec 2006. [Online]. Available: http://link.aps.org/doi/10.1103/PhysRevLett.97.247401

[206] C. G. Yale, B. B. Buckley, D. J. Christle, G. Burkard, F. J. Heremans, L. C. Bassett, and D. D. Awschalom, "All-optical control of a solid-state spin using coherent dark states," *Proceedings of the National Academy of Sciences*, vol. 110, no. 19, pp. 7595–7600, may 2013. [Online]. Available: http://www.pnas.org/cgi/doi/10.1073/pnas.1305920110

[207] C. Cohen-Tannoudji, F. Laloe, and B. Diu, *Mécanique quantique - Tome 1 et 2*, hermann ed., Paris, 2007.

[208] J. D. Mar, J. J. Baumberg, X. L. Xu, A. C. Irvine, and D. A. Williams, "Electrical control of quantum-dot fine-structure splitting for high-fidelity hole spin initialization," *Physical Review B*, vol. 93, no. 4, p. 045316, jan 2016. [Online]. Available: http://journals.aps.org/prb/abstract/10.1103/PhysRevB.93.045316

[209] A. Jarmola, V. M. Acosta, K. Jensen, S. Chemerisov, and D. Budker, "Temperature- and Magnetic-Field-Dependent Longitudinal Spin Relaxation in Nitrogen-Vacancy Ensembles in Diamond," *Physical Review Letters*, vol. 108, no. 19, p. 197601, may 2012. [Online]. Available: http://link.aps.org/doi/10.1103/PhysRevLett.108.197601

[210] M. Wu, J. Jiang, and M. Weng, "Spin dynamics in semiconductors," *Physics Reports*, vol. 493, no. 2-4, pp. 61–236, aug 2010. [Online]. Available: http://www.sciencedirect.com/science/article/pii/S0370157310000955

[211] A. Delteil, W.-B. Gao, P. Fallahi, J. Miguel-Sanchez, and A. Imamoğlu, "Observation of quantum jumps of a single quantum dot spin using submicrosecond single-shot optical readout." *Physical review letters*, vol. 112, no. 11, p. 116802, mar 2014. [Online]. Available: http://journals.aps.org/prl/abstract/10.1103/PhysRevLett.112.116802

[212] X. Ding, Y. He, Z.-C. Duan, N. Gregersen, M.-C. Chen, S. Unsleber, S. Maier, C. Schneider, M. Kamp, S. Höfling, C.-Y. Lu, and J.-W. Pan, "On-Demand Single Photons with High Extraction Efficiency and Near-Unity Indistinguishability from a Resonantly Driven Quantum Dot in a Micropillar," *Physical Review Letters*, vol. 116, no. 2, p. 020401, jan 2016. [Online]. Available: http://link.aps.org/doi/10.1103/PhysRevLett.116.020401

[213] S. E. Economou, J. I. Climente, A. Badolato, A. S. Bracker, D. Gammon, and M. F. Doty, "Scalable qubit architecture based on holes in quantum dot molecules," *Physical Review B*, vol. 86, no. 8, p. 085319, aug 2012. [Online]. Available: http://link.aps.org/doi/10.1103/PhysRevB.86.085319

[214] E. B. Flagg and G. S. Solomon, "Optical spin readout method in a quantum dot using the ac Stark effect," *Physical Review B*, vol. 92, no. 24, p. 245309, dec 2015. [Online]. Available: http://link.aps.org/doi/10.1103/PhysRevB.92.245309

[215] S. Sun, H. Kim, G. S. Solomon, and E. Waks, "A quantum phase switch between a single solid-state spin and a photon," *Nature Nanotechnology*, feb 2016. [Online]. Available: http://arxiv.org/abs/1506.06036

APPENDICE A T_d - symmetry operations and character table

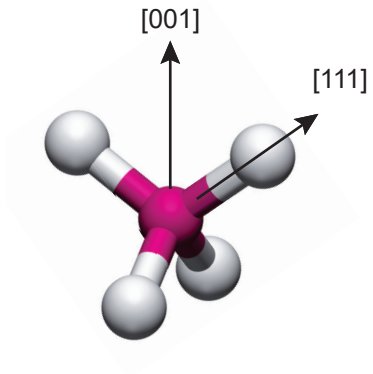

Figure A.1 An isolated-atom IC (pink atom) presents a T_d symmetry inside a zinc-blende host. The symmetry point group describing the defect and its host includes 24 operations.

The T_d point group is composed of 24 symmetry elements (see Fig. A.1) which are separated in 5 classes:

E	Identity (1 operation);
C_3	Clockwise and counterclockwise rotations of $2\pi/3$ about the $\langle 1\,1\,1\rangle$ directions (8 operations);
C_2	Rotations of π about the $\langle 1\,0\,0\rangle$ axes (3 operations)
S_4	Improper rotations of $\pi/2$ about the $\langle 1\,0\,0\rangle$ axes (6 operations)
σ_d	Reflections across the $\{1\,1\,0\}$ family of planes (6 operations)

In addition to these crystal elements symmetries, the half-integers spin of the electrons, which is invariant under 4π rotations, doubles the number of symmetry elements. 9 of these elements are added to existing classes:C_2R (3 operations) and σ_dR (6 operations); and 15 form three new classes of operations:

R	Spin state rotation around the quantization axis (1 operation);
C_3R	C_3 transformations added to the R spin rotation (8 operations);
S_4R	S_4 transformation added to R spin rotation (6 operations)

C_2R (3 operations) and σ_dR (6 operations) do not form new classes of operations, because they belong to the existing C_2 and σ_d classes, respectively.

The character table of the T_d double group is presented in Table A.1. In the last column of the table are presented basic functions that transform according to the corresponding representation. x, y, z stand for the spatial coordinates, l_x, l_y, l_z for the components of angular momentum vectors, (α, β) for the up and down spinors of s-type electrons, and ϕ_{1-4} for the angular wave-function of p-type electrons.

Table A.1 The T_d double group character table presents 7 irreducible representations, among which two corresponds to the symmetry representation of s-type conduction electrons (Γ_6) and light- and heavy-holes (Γ_8). Space and angular momentum vectors transform according to the Γ_4 and Γ_5 representations, respectively.

T_d	E	R	$8C_3$	$8C_3R$	$3C_2$ $3C_2R$	$6S_4$	$6S_4R$	$6\sigma_d$ $6\sigma_dR$	Basis functions
Γ_1	1	1	1	1	1	1	1	1	$x^2+y^2+z^2$
Γ_2	1	1	1	1	1	-1	-1	-1	$l_x l_y l_z$
Γ_3	2	2	-1	-1	2	0	0	0	
Γ_4	3	3	0	0	-1	-1	-1	1	(x, y, z)
Γ_5	3	3	0	0	-1	1	1	-1	(l_x, l_y, l_z)
Γ_6	2	-2	1	-1	0	$\sqrt{2}$	$-\sqrt{2}$	0	(α, β)
Γ_7	2	-2	1	-1	0	$-\sqrt{2}$	$\sqrt{2}$	0	
Γ_8	4	-4	-1	1	0	0	0	0	(ϕ_{1-4})

The wave-function of excitons is obtained by taking the direct product of the electron and hole symmetry representations (Γ_6 and Γ_8, respectively):

$$\Gamma_X = \Gamma_e \otimes \Gamma_h = \Gamma_6 \otimes \Gamma_8 = \Gamma_3 \oplus \Gamma_4 \oplus \Gamma_5, \tag{A.1}$$

Excitons bound to isolated-impurity ICs thus present a fine structure separated in three sub-spaces corresponding to one doublet (Γ_3) and two triplets ($\Gamma_{4,5}$). Understanding the strong difference in the intensity of these transitions requires to evaluate the strength of their coupling to the electromagnetic field, which is presented in the following section.

APPENDICE B C_{2v} - symmetry operations and character table

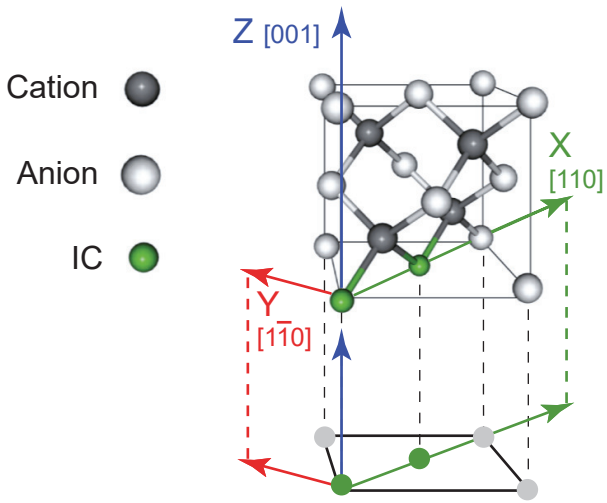

Figure B.1 Dyad (green atoms) presenting a C_{2v} symmetry inside a zinc-blende host. The symmetry point group describing the defect and its host includes 8 operations.

The C_{2v} double point group presents 4 spatial symmetry elements and as much spin symmetry elements (see Fig. B.1 (b)), that form 5 classes of symmetry operations:

E	Identity (1 operation);
R	Spin state rotation of 2π around the quantization axis (1 operation).
C_2/C_2R	π rotation around axis C_2 (2 operations);
σ_v/σ_vR	Reflection across the plane normal to the dyad (2 operations);
$\sigma_{v'}/\sigma_{v'}R$	Reflection across the plane defined by the dyad and the C_2 axis (2 operations);

C_2R, σ_vR and $\sigma_{v'}R$ correspond to C_2, σ_v and $\sigma_{v'}$ operations followed by a spin rotation. All these symmetry operations form the character table presented in Table B.1:

HH and LH excitonic states are each obtained by the direct product of the electron and hole representations, which here corresponds to the product of the Γ_5 representation with itself:

$$\Gamma_5 \otimes \Gamma_5 = \Gamma_1 \oplus \Gamma_2 \oplus \Gamma_3 \oplus \Gamma_4. \tag{B.1}$$

The exciton fine structure associated to C_{2v} dyads is therefore formed of 8 non-degenerate

Table B.1 The C_{2v} double group character table presents 5 classes of symmetry representations, where the spatial coordinates x, y, and z are all non-equivalent, as they transform according to different representation. Half-integer spin states all belong to the Γ_5 representation.

T_d	E	C_2 C_2R	σ_v σ_vR	$\sigma_{v'}$ $\sigma_{v'}R$	R	Basis functions Basis functions
Γ_1	1	1	1	1	1	z
Γ_2	1	-1	1	-1	1	R_z
Γ_3	1	-1	-1	1	1	x, R_y
Γ_4	1	1	-1	-1	1	y, R_x)
Γ_5	2	0	0	0	-2	(α, β) (ϕ_{1-4})

exciton states separated in 2 sub-spaces of 4 non-degenerate states belonging to the Γ_1, Γ_2, Γ_3, and Γ_4: one subset corresponding to LH excitons, and the other associated to HH excitons.